HEAVY OIL UPGRADING FROM ELECTRON BEAM (E-BEAM) IRRADIATION

A Thesis

by

DAEGIL YANG

Submitted to the Office of Graduate Studies of
Texas A&M University
in partial fulfillment of the requirements for the degree of

MASTER OF SCIENCE

December 2009

Major Subject: Petroleum Engineering

HEAVY OIL UPGRADING FROM ELECTRON BEAM (E-BEAM) IRRADIATION

A Thesis

by

DAEGIL YANG

Submitted to the Office of Graduate Studies of
Texas A&M University
in partial fulfillment of the requirements for the degree of

MASTER OF SCIENCE

Approved by:

Chair of Committee,	Maria A. Barrufet
Committee Members,	William D. McCain, Jr.
	Rosana G. Moreira
Head of Department,	Stephen A. Holditch

December 2009

Major Subject: Petroleum Engineering

ABSTRACT

Heavy Oil Upgrading from Electron Beam (E-Beam) Irradiation. (December 2009)
Daegil Yang, B.S., Kookmin University
Chair of Advisory Committee: Dr. Maria A. Barrufet

Society's growing demands for energy results in rapid increase in oil consumption and motivates us to make unconventional resources conventional resources. There are enormous amounts of heavy oil reserves in the world but the lack of cost effective technologies either for extraction, transportation, or refinery upgrading hinders the development of heavy oil reserves.

One of the critical problems with heavy oil and bitumen is that they require large amounts of thermal energy and expensive catalysts to upgrade. This thesis demonstrates that electron beam (E-Beam) heavy oil upgrading, which uses unique features of E-Beam irradiation, may be used to improve conventional heavy oil upgrading. E-Beam processing lowers the thermal energy requirements and could sharply reduce the investment in catalysts. The design of the facilities can be simpler and will contribute to lowering the costs of transporting and processing heavy oil and bitumen.

E-Beam technology uses the high kinetic energy of fast electrons, which not only transfer their energy but also interact with hydrocarbons to break the heavy molecules with lower thermal energy.

In this work, we conducted three major stages to evaluate the applicability of E-Beam for heavy oil upgrading. First, we conducted laboratory experiments to investigate the effects of E-Beam on hydrocarbons. To do so, we used a Van de Graff accelerator, which generates the high kinetic energy of electrons, and a laboratory scale apparatus to investigate extensively how radiation effects hydrocarbons. Second, we studied the energy transfer mechanism of E-Beam upgrading to optimize the process. Third we conducted a preliminary economic analysis based on energy consumption and compared the economics of E-Beam upgrading with conventional upgrading.

The results of our study are very encouraging. From the experiments we found that E-Beam effect on hydrocarbon is significant. We used less thermal energy for distillation of n-hexadecane (n-C_{16}) and naphtha with E-Beam. The results of experiments with asphaltene indicate that E-Beam enhances the decomposition of heavy hydrocarbon molecules and improves the quality of upgraded hydrocarbon. From the study of energy transfer mechanism, we estimated heat loss, fluid movement, and radiation energy distribution during the reaction. The results of our economic evaluation show that E-Beam upgrading appears to be economically feasible in petroleum industry applications.

These results indicate significant potential for the application of E-Beam technology throughout the petroleum industry, particularly near production facilities, transportation pipelines, and refining industry.

DEDICATION

To my lovely wife, Jiu Choe,
for her great support, sacrifice, and unconditional love.
She is the only reason for my study, work, and life.

To my expected baby,
for giving happiness, hope, and joy.

To my parents and parents in laws,
for their love and support.

To my uncle Dennis,
for giving me strong motivation and confidence in my studies.

ACKNOWLEDGMENTS

I would like to express my gratitude to Dr. Maria A. Barrufet, my academic advisor and chair of my committee, for financial assistance, strong encouragement, and academic guidance, all of which helped me to complete this study.

I would like to thank Dr. Rosana Moreira for allowing me to access the Van de Graff facility and for providing valuable advice.

Also, I would like to thank to Dr. William McCain, whose knowledge of phase behavior and service on my committee I found invaluable.

Because this study was interdisciplinary, I would not have been able to complete it without the collaboration and support of all the individuals and groups involved in this project. Therefore, I would like to express my sincerest appreciation to TOTAL Petrochemicals and TOTAL E&P for supporting this research, Dr. Jose Sosa in TOTAL Petrochemicals for serving on my committee and supporting and advising this study with his profound knowledge and expertise, Philippe Remacle of TOTAL E&P for his active support of this research, Dr. Joe Pelati and Jim Butler also of TOTAL Petrochemicals, for advice and technical support, and Jonathan Lyons for chemical analysis of samples and technical support.

Special thanks to Dr. Jongsoon Kim and Paulo Silva, E-Beam research group members, for collaborating with me for this research project. Especially, I thank Dr. Jongsoon Kim for his great contribution to the energy transfer simulation by conducting a radiation transport simulation.

TABLE OF CONTENTS

Page

Page

LIST OF FIGURES

Page

Page

Page

Page

Page

Page

Page

LIST OF TABLES

Page

Page

Page

CHAPTER I

INTRODUCTION

One of the greatest challenges facing our continued use of petroleum as we transition to a balanced use of various energy sources is that the largest remaining reserves of petroleum are made of molecules that are large and difficult to upgrade. For example, three oil sand areas (Athabasca, Cold Lake, and Peace River) in Canada contain an estimated 172.2 billion bbl of remaining reserves (Elliot 2008). However, limitations on current extraction, refining, and upgrading technologies limit production and development to 1% of heavy oil deposits worldwide (Yan 2002; Dickenson 1997).

Minimum upgrading implies reducing the oil viscosity without adding costly solvents to facilitate transportation. The most severe and common upgrading method is to break down heavier molecules to obtain higher quality products such as gas oil and gasoline, which requires a substantial amount of thermal energy and expensive catalysts. Current upgrading methods based on thermo-catalytic-cracking (TCC) require very large capital investments, high operating costs, and vast and complex facilities, and also resulted in chronic bottlenecks. The biggest limitation is that any TCC-based upgrading expends the equivalent of about one third of the energy of the oil processed, with the energy taking the form of steam and heat (Zhussupov 2006; Raseev 2003).

Many laboratories all over the work have conducted research on the radiation chemistry of hydrocarbons since the mid-1920s. In 1965, Salvoy and Falconer used a VDG E-Beam generator and a gamma ray machine to show that the effects of irradiation of n-hexadecane (n-C_{16}) are apparently independent of source and dose rate. Wu et al. (1997) conducted n-C_{16} radiation thermal cracking (RTC) with gamma rays and found that radiation enhances the cracking process. Recent research of polymer cracking with E-Beam (Miao et al. 2009) found that irradiating polymer causes main chain scission at

---

This thesis follows the style of *SPE Reservoir Evaluation & Engineering*.

doses below 200 kGy.

By using a viscous, high paraffin, high sulfur content crude under a very high dose rate (1~4 kGy/s) for a RTC experiment, Zaykina et al. (2001, 2002, 2004, 2004) observed sulfur content reduction, isomerization, and polymerization. In addition, Zaykina's group (2004) conducted RTC of bitumen and observed an increase in isoparaffins and light oil yield with a slight reduction of aromatic components. The greatest problem during thermal cracking arises from reactions involving aromatic feed since aromatic compounds in the feed have a very high tendency to undergo polycondensation reactions that results in coke formation (Simanzhenkov, 2003).

However, their reports lack important information such as descriptions of the experimental procedures, dose calibration, and sample size. Furthermore, they used samples from Kazakhstan and the Caspian area only and, samples from other areas may produce different results. Therefore, discerning a rigorous cause-and-effect relationship in radiation experiment requires well-defined oil samples.

Zaykin et al. (2003) also analyzed energy consumption of hydrocarbon chain cracking reactions for different types of processing. They reported that radiation thermal processing saves a significant amount of energy compared to conventional thermal processing methods. However, they did not describe the system with which they evaluated the energy consumption. Their previous paper (Zaykin et al. 2003) described a layout of hydrocarbon enhancement electron-beam technology (HEET). However, the paper did not provide details of the process mechanisms, operating condition, and specification of the facility.

Zaykin's recent paper (2008) verified the theoretical concept of low-temperature radiation-induced cracking of liquid hydrocarbon through radiation cracking experiments. However, the reported dose rate is too high and there is no description of the experiments and oil samples.

Using some of experimental data, Zhussupov (2006) evaluated the economic feasibility of E-Beam upgrading and compared it with conventional upgrading. However, his work has several simplifications and lots of uncertainties.

1.1 Objective

The main objective of this research is to investigate the effects of E-Beam irradiation on hydrocarbons and evaluate economics and potential applications of E-Beam technology throughout petroleum industry.

1.1.1 Investigation of E-Beam Irradiation on Hydrocarbons

In this study, we will investigate the effects of radiation on hydrocarbons in order to resolve the unknowns and to clarify the ambiguity of the experimental results of previous works.

To analyze accurately the fundamental behavior of E-Beam radiation on hydrocarbons, we will study pure n-C_{16}, a naphtha cut, a combination of a well-defined hydrocarbon groups, and asphaltene to evaluate the effect radiation on heavy and very viscous components. In the experiments, we will change experimental conditions and setup to evaluate the effects of E-Beam radiation under different temperature, radiation exposure, and residence time.

It is very important to estimate how much energy absorbed in the system during the experiment. Therefore, it is essential to study energy transfer mechanism of the process. To estimate the energy transfer mechanism in the system, we will conduct two simulations: heat transfer simulation using computational fluid dynamics (CFD), and radiation transport Monte-Carlo simulation.

1.1.2 Potential Applications and Economic Evaluation

With the results we obtained from the laboratory investigation, we will propose potential applications of this technology. In addition, we will introduce an available industrial scale E-Beam machine which can be used for the potential application. Using the specification of the machines and our experimental results, we will conduct preliminary economic evaluation to compare E-Beam upgrading and conventional upgrading based on the energy used in each process.

1.2 Literature Review

1.2.1 Heavy Oil Background

The global energy trend forecasts point to an increasing demand of fossil fuel over the next decades. However, the crude oil share in the total primary energy supply will remain around 35% until 2030 (Saniere et al. 2007). Thus, the remaining 65% of the energy supply must come from other non-conventional resources such as tar sands, extra-heavy oil, and oil shale. Tremendous amounts of heavy oil resources are available in the world. **Fig. 1.1** shows the total world oil reserves, and indicates that heavy oil, extra heavy oil, and bitumen make up about 70% of the world's total oil resources of 9 to 13 trillion bbl (Alboudwarej et al. 2006). In addition, conventional oil reserves are depleting. **Fig. 1.2** shows that crude oils have become heavier and sour, with the likelihood of further deteriorating quality.

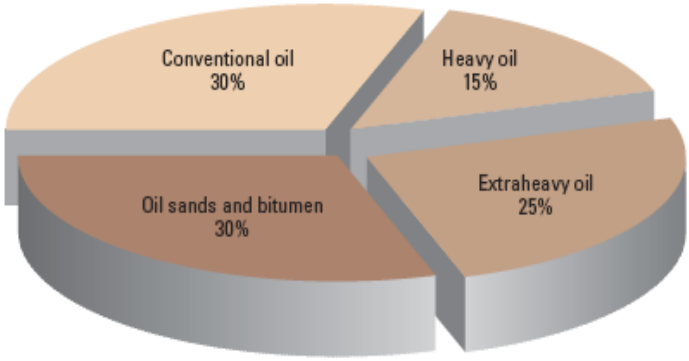

Fig. 1.1—Total world oil reserves (Source: Alboudwarej et al. 2006).

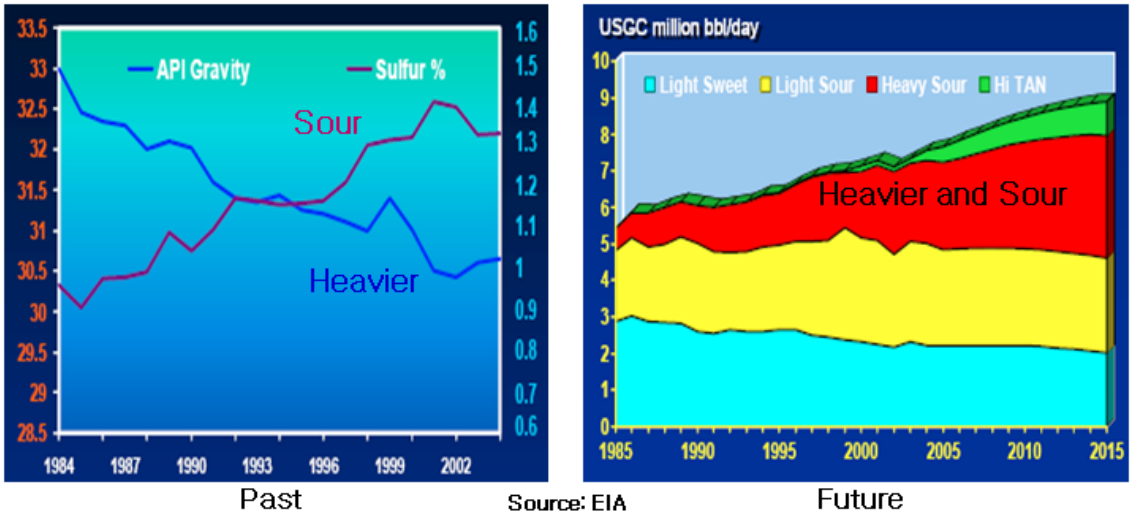

Fig. 1.2—US refinery input quality from 1984 to 2002 and USGC refinery input quality per day from 1985 to 2015. (USGC: US gulf coast refinery, HiTAN: high toxic acid number)

Making those unconventional oil reserves profitable requires an increased focus on technology that make the exploitation of heavy crude oil economically viable. To accomplish this, we must develop cost-effective ways to upgrade the heavy oil by removing sulfur, water, salts, and other impurities, decreasing the density, and/or reducing the viscosity (Agrell et al. 2007).

Heavy oils are characterized by low H/C ratios, high viscosities, and high concentrations of metals and hetero-atoms, such as sulfurs and nitrogen (Wangen et al. 2007). In the petroleum industry, crude oils are classified based on viscosity and API gravity. **Fig. 1-3** shows the classification of crude oils (Khan 2007). From the figure, we can consider crude oils with API gravity lower than 20 and viscosity higher than 100 cp as heavy crude oils.

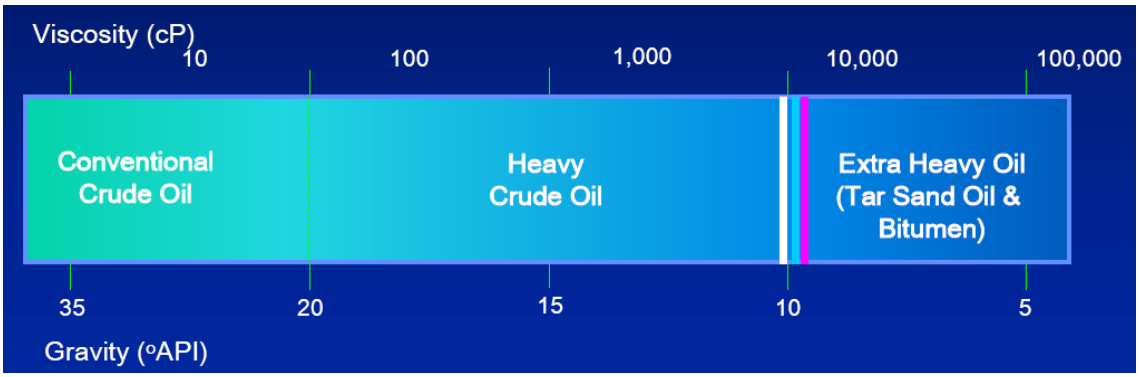

Fig. 1.3—Typical crude oil viscosity and API ranges for conventional to extra heavy oil (Khan 2007).

The following is a brief discussion about some specific problems that heavy oil poses for the E&P and the Refining industry. As discussed earlier, transportation problems exist with heavy oils because of their high viscosity. The current methods available to transport heavy oil include dilution, partial upgrading, and insulation or warming of pipelines (Koppel et al. 2002; Argillier et al. 2005; Veith 2007), though these methods are expensive. In addition, the high sulfur content of heavy oil causes pipeline corrosion which is a major cause of pipeline failures. The easiest way to remove sulfur is field upgrading using cracking methods (Khan 2007). Therefore, a promising alternative for the heavy oil transportation problem is to apply cost effective field upgrading technology. The refining side also has several problems because of the high aromaticity, high molecular weight, and high heteroatom content of heavy oil (Yasar 2001). Thus, refining heavy oil requires excessive thermal energy. For catalytic processes, very expensive catalysts must be used, though these may become poisoned or inactive, and will increase the complexity of the operation. Another problem is that it requires many large-scale facilities. Therefore, conventional upgrading must be improved by applying new innovative technology to resolve these problems in both the E&P and Refining industry.

1.2.2 Hydrocarbon Upgrading

Upgrading is converting heavy crude oil into light, higher value crude or into valuable transportation fuels. There are several technologies available to do this. The most common upgrading technologies are thermal cracking (TC) base technologies such as visbreaking, and delayed and fluid coking (Lott et al. 2005). During cracking, larger molecules break down to smaller molecules via C–C bond cleavage, which happens with free-radical chain reactions. **Fig. 1-4** illustrates the main chemical reactions during hydrocarbon-hexadecane thermal cracking. During the cracking, larger molecules break down to smaller molecules via C–C bond cleavage, initiated by free-radical formation. Free radicals are molecular species with unpaired electrons that have a highly reactive nature.

$$n-C_{16}H_{34} \rightarrow {}^{\bullet}C_8H_{17} + {}^{\bullet}C_8H_{17} \quad \textbf{(Radical formation)}$$

$$\left.\begin{aligned} {}^{\bullet}C_8H_{17} + n-C_{16}H_{34} &\rightarrow C_8H_{18} + {}^{\bullet}C_{16}H_{33} \\ {}^{\bullet}CH_3 + n-C_{16}H_{34} &\rightarrow CH_4 + {}^{\bullet}C_{16}H_{33} \\ {}^{\bullet}C_2H_5 + n-C_{16}H_{34} &\rightarrow C_2H_6 + {}^{\bullet}C_{16}H_{33} \end{aligned}\right\} \textbf{(H abstraction)}$$

$${}^{\bullet}C_{16}H_{33} \rightarrow {}^{\bullet}C_8H_{17} + C_8H_{16} \quad \textbf{(Radical decomposition)}$$

Fig. 1.4—Main chemical reactions during n-C_{16} thermal cracking. The n-C_{16} molecule breaks into two free radicals and many different chemical reactions initiated by the free radicals.

In case of radiation thermal cracking of hexadecane, C-H dissociation is one of the predominant processes. Hydrogen atoms produced from C-H dissociation easily undergo hydrogen abstraction leading to H_2 formation and can produce alkene products (Wu et al. 1997). **Fig. 1.5** illustrates several reactions that lead to hydrogen formation and olefin formation by radiation process.

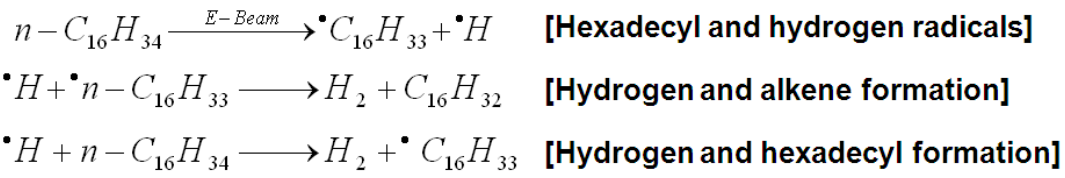

Fig. 1.5—Main chemical reactions during n-hexadecane radiation thermal cracking that produce hydrogen (Salvoy et al. 1965).

1.2.3 Radiation Background

The energy of an electron is usually measured in electron volts (eV). An electron volt is the energy acquired by one electron at a potential difference of 1V. Electrons passing through neutral material excite and ionize atoms, so that they can also emit energy (Turner 1986). When a charged particle interacts with a medium, it produces an ionization event or ion pair production. Electrons may interact either with the Coulomb field of the nucleus of an atom or with the electron shell in elastic or non-elastic interactions. When the energetic electrons interact with the electrons of the absorbing material in non-elastic interaction they slow down, and ionization or excitation of the absorbing material results. In the course of elastic scattering, the direction of interaction is determined by the energy of the electrons and the nature of the absorbing material (Foldiak 1981). Stopping power is the expectation value of the rate of energy loss per unit of path length *x* by a charged particle of type *Y* and kinetic energy *T*, in a medium of atomic number *Z* (Attix 1986). Mathematically, it is expressed as

$$\left(\frac{dT}{dx}\right)_{Y,T,Z}, \qquad (1.1)$$

The typical unit of stopping power is MeV/cm or J/V ($1MeV/cm \equiv 1.602 \times 10^{-11} J/m$). If we divide the stopping power by the density ρ of the absorbing medium, it results in a quantity called the mass stopping power which is expressed as

$$\left(\frac{dT}{\rho dx}\right), \qquad (1.2)$$

The typical unit for mass stopping power is MeV cm^2/g or Jm^2/kg.

The range *R* is a charged particle of an electron of a given energy in a given medium; it is the expectation value of the path length *x* that it follows until it comes to rest (Attix 1986). Due to the stochastic nature of interactions, two electrons of identical initial energy will not have identical path lengths (Braby 2008). A similar but not identical quantity is called the CSDA (continuously slowing down approximation) range (Beger and Seltzer 1983). The CSDA range is defined as

$$R_{CSDA} \equiv \int_0^{T_0} \left(\frac{dT}{\rho dx} \right)^{-1} dT \,, \qquad (1.3)$$

where T_0 is the starting energy of the electron.

If $\left(\frac{dT}{\rho dx} \right)$ is given in MeVcm^2/g and dT is MeV, then R_{CSDA} is given in g/cm^2.

Absorbed dose, defined by radiation energy per unit mass, is a measure of that part of the energy transferred to the irradiated material that results in the formation of ions and excited molecules. In other words, it is the energy absorbed in unit mass of a material that can generate chemical or physical change in the irradiated material. The absorbed dose is determined by the characteristics of the radiation field and the composition of the stopping material (Woods 1994).

Absorbed dose is the expectation value of the energy imparted to the matter per unit mass (Attix 1986). The unit for this is J/kg or kJ/kg which, according to the International Standard (SI), is given the special name gray (Gy) or kilo gray (kGy). If we have one kilogram of stone and if this stone received radiation energy equal to 1 kilo joule, the radiation dose for this stone is 1 kGy (Yang 2009).

Radiation technology is used in many different fields for different purposes (**Fig. 1.6**). For food treatment and safety, such as food pasteurization, we use a dose range of 0.1~3kGy. For Gemstone coloring, we use very high dose range above 1500 kGy. We also receive radiation doses in our common life. Natural background radiation is around 3 miligray per year. So, each individual gets around 3 miligray yearly. In comparison, a

hospital CT scan produces a dose of around 10 miligray. As a reference, the radiation dose we used for our asphaltene experiment is around 3.1 kGy.

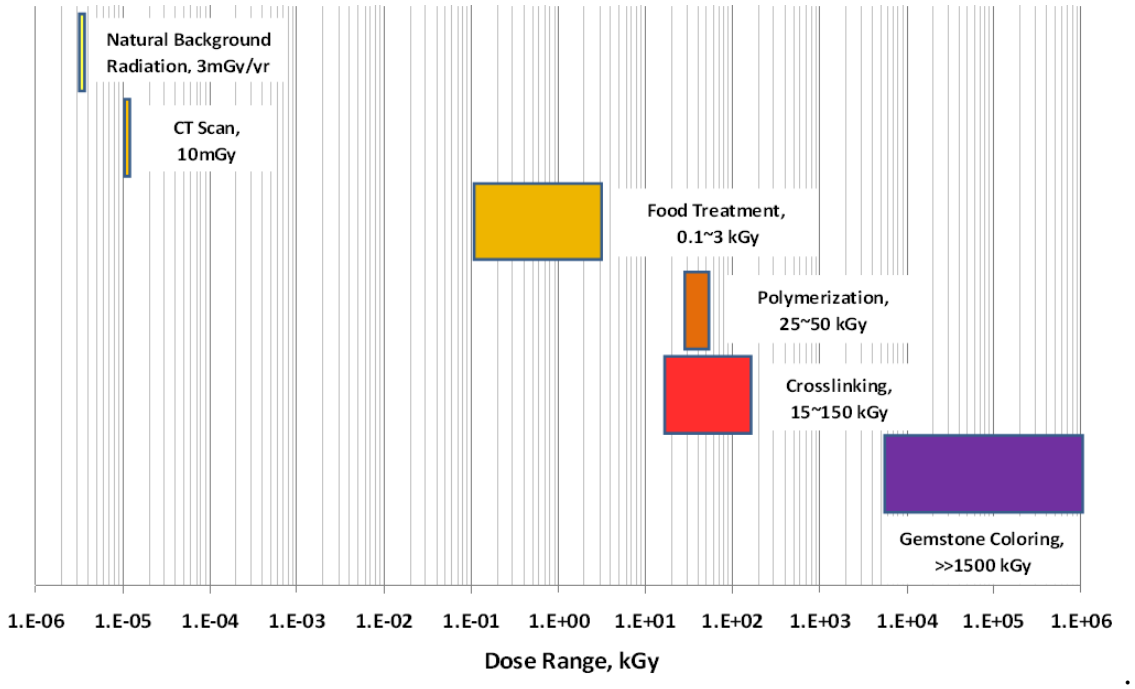

Fig. 1.6—Radiation dose range for specific treatment.

Dosimetry is the study of the physical quantities of concern for radiation applications and for radiation protection. The goal of dosimetry for health physics application is to evaluate the potential consequences of a radiation exposure. To do this we need to determine the dose at a control volume within the object exposed (a part of the person's body). In our application (hydrocarbon upgrading) our specific location is the entire volume of hydrocarbon in the reactor since we want to upgrade the entire sample placed in the reactor using E-Beam radiation.

The following discussion helps to clarify the concept of radiation energy. In radiation dosimetry, radiation energy is categorized into two parts, dose and kerma which are based on energy imparted and energy transferred. The energy imparted is defined as,

$$\varepsilon = R_{in} - R_{out} + \Sigma Q, \text{ ..}\ldots\ldots\text{..}\ldots\ldots\ldots\ldots\ldots\ldots\ldots\ldots\ldots\ldots\ldots\ldots\ldots\ldots\ldots\ldots\ldots\ldots \quad (1.4)$$

where R_{in} is the radiant energy incident on the volume and R_{out} is the radiant energy emerging from the volume. ΣQ is the sum of all changes (decreases: positive sign, increases: negative sign) of the rest mass energy of nuclei and elementary particles in any nuclear transformations which occur in the volume. An example is shown in **Fig. 1.7**. A γ-ray $h\nu_1$ is emitted by a radioactive atom in *V*. The photon ($h\nu_1$) undergoes pair production, giving kinetic energy T_1 to the electron T_2 to the positron. Both are annihilated and the resulting two photons (0.511 MeV each) are shown escaping from *V*. Then the energy imparted (ε) is, ε = 0-1.022 MeV + ΣQ

where $\Sigma Q = h\nu_1 - 2m_0c^2 + 2m_0c^2 = h\nu_1$

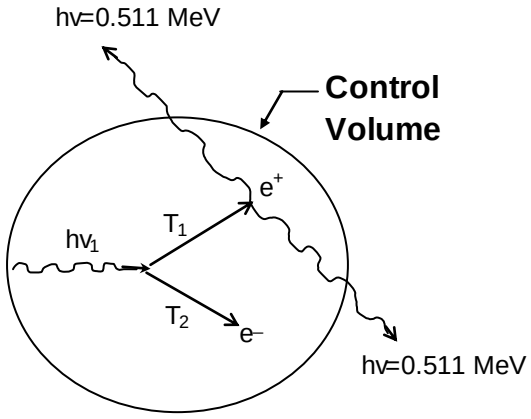

Fig. 1.7—Example involving γ-ray emission, pair production, and positron annihilation (Attix, 1983).

ε is a stochastic quantity. The expectation value of ε, termed the mean energy $\bar{\varepsilon}$, is a non-stochastic quantity. We should remember that ε is specific to the material of the absorber as well as radiation. ε is usually expressed in Joules (J). Now we can express the absorbed dose as follows:

$$D = \frac{d\bar{\varepsilon}}{dm}, \text{ ..}\ldots\ldots\text{..}\ldots\ldots\ldots\ldots\ldots\ldots\ldots\ldots\ldots\ldots\ldots\ldots\ldots\ldots\ldots\ldots\ldots\ldots \quad (1.5)$$

Kerma is the quotient of dE_{tr} by *dm*. dE_{tr} is the sum of the initial kinetic energies of all the charged ionizing particles liberated by uncharged ionizing particles in a material of mass *dm*. Kerma, *K*, is defined as

$$K = \frac{dE_{tr}}{dm} \text{ (J/kg)} , \ldots\ldots\ldots\ldots\ldots\ldots\ldots\ldots\ldots\ldots\ldots\ldots\ldots\ldots\ldots\ldots\ldots\ldots \text{(1.6)}$$

The Kerma is expressed in the same units as dose. From the concepts of dose and kerma, we can derive very important concepts which make dose measurement more convenient. *K* is relatively easy to calculate but probably impossible to measure. *D* is relatively easy to measure but difficult to calculate. This is because we are able to calculate how much radiation energy transferred to a target material but we cannot calculate how much of the transferred energy was absorbed by the target material without measuring it. Under very special circumstances (Radiation equilibrium and charged particle equilibrium), *D=K*. **Fig. 1.8** shows a set of circumstances in which charged particle equilibrium can occur. Electron e_2 enters the control volume with a kinetic energy *T* equal to that carried out by electron e_1. If e_1 then emits an x-ray $h\nu_1$, e_2 will also emit an identical x-ray $h\nu_2$ (Braby 2008).

Fig. 1.8—Circumstance when CPE exists in a control volume (Braby 2008).

We used a concept of charged particle equilibrium (CPE) to measure dose. If CPE exists, then

$$\overset{CPE}{D} = K_c = \psi\left(\frac{\mu_{en}}{\rho}\right), \ldots\ldots\ldots\ldots\ldots\ldots (1.7)$$

where ψ (energy fluence) is defined by energy per unit area (J/m^2), and $\left(\frac{\mu_{en}}{\rho}\right)$ is the energy absorption coefficient.

Now we use this concept for measuring the absorbed dose. When we have CPE in the air,

$$D_{air} = (K_c)_{air}\ , \ldots\ldots\ldots\ldots\ldots\ldots (1.8)$$

Therefore, exposure, which is the absolute volume of the total charge of the ions of one sign produced in the air when all the electrons in the air of mass *dm* are completely stopped, is calculated from

$$X = D_{air}\left(\frac{e}{\overline{W}_{air}}\right) \text{ (C/kg)}, \ldots\ldots\ldots\ldots\ldots\ldots (1.9)$$

$\overline{W}_{air}$ is the energy required to generate a positron and an electron, also called an ion pair (Attix 1986).

where $\frac{\overline{W}_{air}}{e} = \frac{33.97\,eV/i.p.(ion.pair)}{1.602\times10^{-19}\,C/electron}\times1.602\times10^{-19}\,J/eV = 33.97\,J/C$

Now, let's calculate dose from the above concepts. Suppose we have the following condition in our farmer ion type chamber, the most common chamber designed for absolute photon and electron dosimetry with therapy dosemeters (**Fig. 1.9**).

Fig. 1.9—Schematic of farmer ion chamber. 1 mg is mass of air in the chamber.

From the given condition, we can calculate the dose rate of the machine. As mentioned before the energy to produce an ion pair is $\overline{W}_{air} = 33.97 eV / i.p$. Since 1 Coulomb is 6.2415×10^{18} electrons then one electron is 1.602×10^{-19} Coulomb. Thus, the number of electrons produced in the chamber per second is

$$IC = 8.831 \times 10^{-8} \times 6.24151 \times 10^{18} = 5.51207 \times 10^{11}$$

Radiation energy absorbed in the ion chamber is the energy required to produce a pair of electrons multiplied by the number of produced electrons.

$$33.97(eV / electron) \times 5.51207 \times 10^{11} = 1.87245 \times 10^{13} eV / \sec$$

Since 1 Joule is $6.24151 \times 10^{18} eV$ the energy rate is

$$\frac{1.87248 \times 10^{13} eV / \sec}{6.24151 \times 10^{18} eV} = 0.000003 J / \sec$$

Therefore, the absorbed dose rate is

$$\dot{D} = \frac{dD}{dt} = \frac{d}{dt}\left(\frac{d\varepsilon}{dm}\right) = \frac{0.000003 J / \sec}{0.000001 kg} = 3 Gy / \sec$$

This is the absorbed dose rate (nominal dose) for this machine. If we run this machine for one hour, the absorbed dose measured in the chamber would be $(3 kGy / s) \times 3600 s = 12.96 kGy$. This is the reference dose that is then used to measure and quantify the absorbed dose of other media since this is the only accurate way of measuring radiation dose with the current technique. However, this is not an absorbed dose for a different media where charged particle equilibrium is not valid. Therefore, in our experimental setup, the absorbed dose in hydrocarbons can be calculated by matching the reference dose data and Monte-Carlo simulation.

1.3 Summary

Chapter I presents the background and literature review for this research.

Chapter II presents methodology for this research. First, we described the facility we used for our experiment. Then, we explained some important techniques and concepts used to measure and calibrate the radiation dose, followed by descriptions of the experimental setup, procedure, and results.

Chapter III presents the simulation study of the E-beam upgrading process, which shows the energy distribution, energy loss, and amount of energy deposited during the process.

Chapter IV presents potential applications and the economic feasibility of this technology.

Chapter V presents the conclusions, recommendations, and possible extensions of this work.

CHAPTER II

LABORATORY INVESTIGATION

In this work, we used a Van de Graff accelerator to generate the high kinetic energy of electrons. We also set up a laboratory scale apparatus to investigate extensively the radiation effects on hydrocarbons. Using the E-Beam machine and the apparatus, we conducted two parallel experiments, one with radiation and the other without radiation. To analyze the fundamental behavior of E-Beam radiation on hydrocarbons accurately, we evaluated three oils of increasing complexity—pure n-C_{16}, a naphtha cut, a combination of a well-defined hydrocarbon groups, and an asphaltene-sample provided from TOTAL Petrochemicals U.S.A. in order to see the radiation effects on heavy and very viscous hydrocarbons.

2.1 Description of E-Beam Accelerator and Operation

2.1.1 E-Beam Machine

A Van de Graff or VDG (**Fig. 2.1**) is an electrostatic accelerator which produces a beam of fast (high kinetic energy) electrons in continuous mode. VDG is a versatile research tool because it provides a steady-state beam with good energy regulation (Humphries 1986). This machine is able to accelerate electrons to selected energy levels between 0.75 MeV and 2MeV. In this experiment, we accelerated electrons to 1.35 MeV since this is chosen to be the ideal energy level for the continuous operation of this machine. This is a relatively low level of kinetic energy compared to other industrial scale accelerators, which can produce 10 MeV of electrons. The main mechanism of this machine is based on the mechanical transfer of charge from the ground to the high voltage terminal (Chao et al. 1999). **Fig. 2.2** shows the configuration of the main parts of a Van De Graff electrostatic accelerator. Electrons generated by corona discharge or physical rubbing in gas are sprayed on to a moving belt.

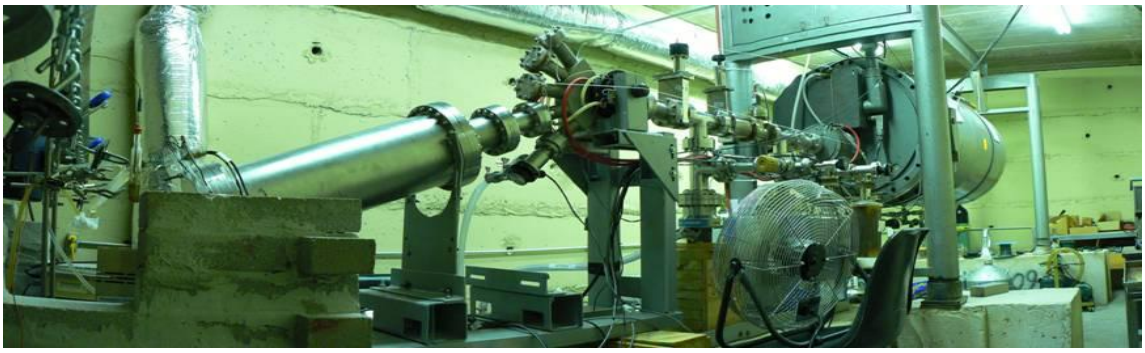

Fig. 2.1—Van De Graff accelerator (VDG) at Texas A&M University.

A DC-power generator is used as an electron source. The plastic rubber moving belt has a high dielectric strength and is immersed in an insulating gas at high pressure. The moving belt transports the sprayed electrons or charges to a high voltage metal terminal where the charge is collected upon contact with a metal comb of needles. The charge is then accelerated back to the ground (Humphries, 1986).

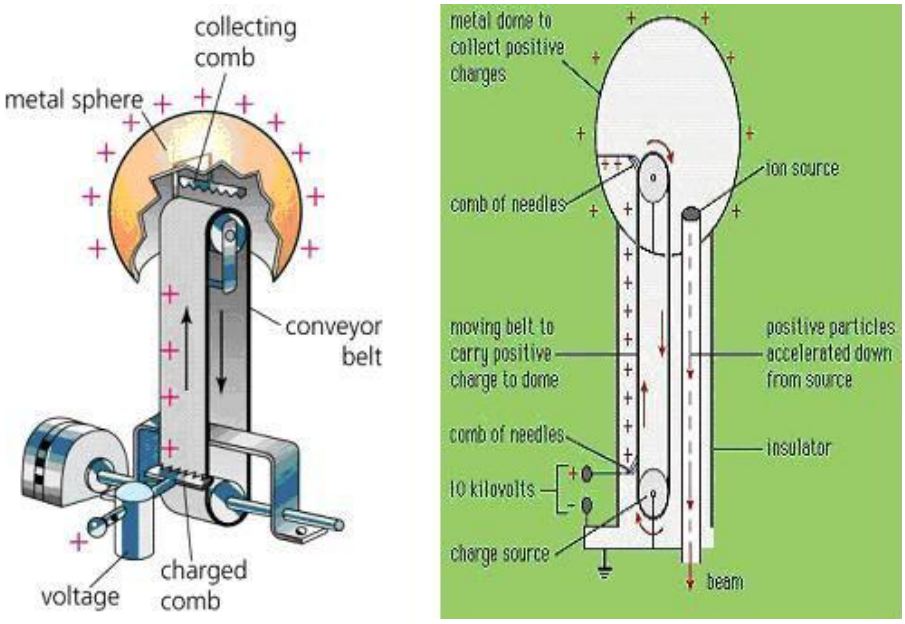

Fig. 2.2—Schematics of main parts Van De Graff accelerator (Wilson 2001).

2.1.2 Van De Graff (VDG) Tune Up

We decided to upgrade the VDG machine (Kim and Fortes Da Silva 2008) to achieve higher doses and robust operation. The following items were repaired or replaced.

Motor Driven Belt. This transports the electrons from the ground to the high voltage terminal, thereby charging the terminal to the desired voltage (**Fig. 2.3**). It was properly cleaned with lint free paper and its static tension (200 lb) was adjusted to reduce flapping and slippage to a practical minimum within the operating pressures of the pulley bearings.

Corona Discharge. This is the belt charge unit that draws electrons from the ground by means of an electronic circuit and sprays them onto the moving belt by an arrangement of corona points (**Fig. 2.3**). Those points were found to be quite dirty because of the dust formed from using the belt. The corona needles were cleaned.

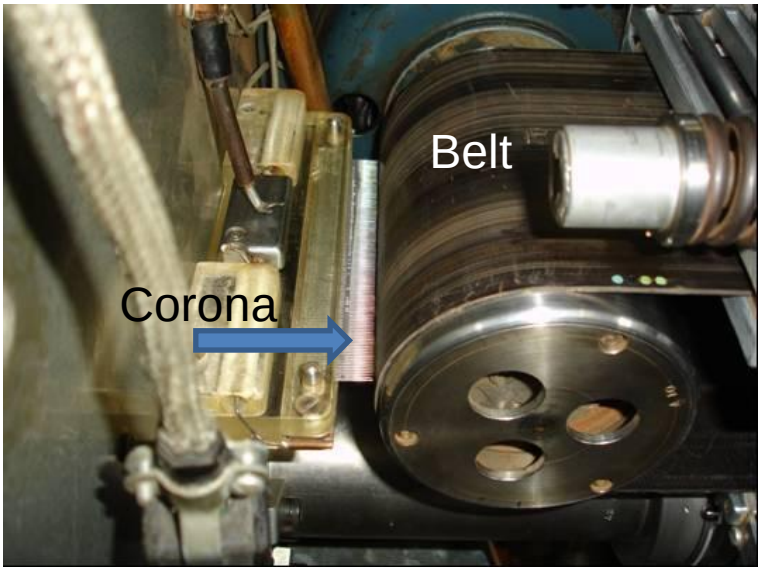

Fig. 2.3—Motor driven belt and corona discharge.

Column. This supports the high voltage terminal, provides an alleyway for the belt, and maintains a uniform potential gradient from the high voltage terminal to the ground. We checked the resistances of the resistors and found that one of the glass spacers was cracked. We used a specific epoxy adhesive with very low conductivity-reactivity and high mechanical strength to repair it.

Cathode head. This is the heart of the machine, taking the electrons from the high voltage terminal and emitting them into the accelerator tube. We found that the cathode we were using was very old and had some extraneous particles. Therefore, we replaced it with a new one. **Fig. 2.4** shows cathode head, new cathode, and old cathode.

Fig. 2.4—Cathode head, new cathode, and old cathode.

Accelerator tube. Using an electrostatic field, this accelerates the electrons to an energy level determined by the voltage of the high voltage terminal, focuses them into a beam, and carries them through the tube extension to the exit beam window. **Fig. 2.5** shows the accelerator column and the accelerator tube inside of the column. We found a broken part of the tube. Therefore, we replaced it with new accelerator tube.

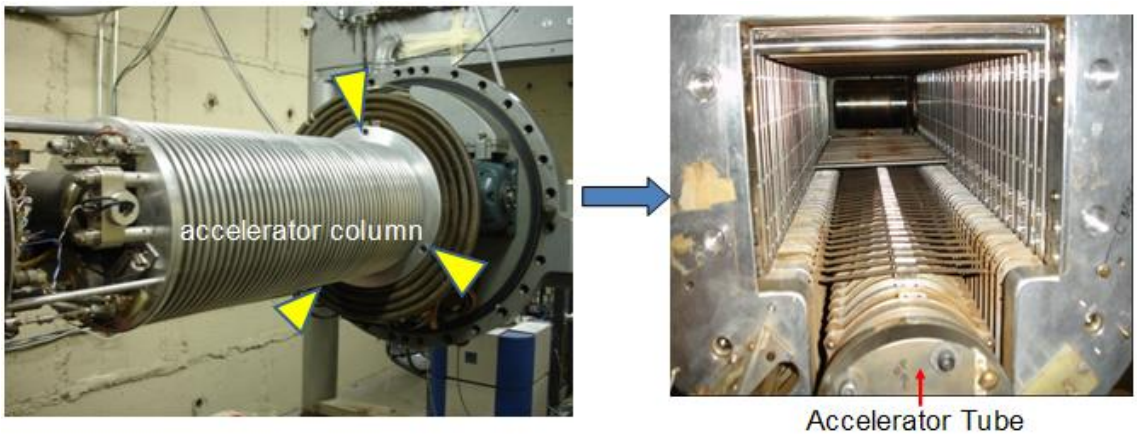

Fig. 2.5—Accelerator tube is located in the accelerator column. Electrons generated from the cathode are accelerated by the electrostatic field of the tube.

In summary, among all the upgrading procedures, the critical works were done by the replacement of the accelerator tube and its cathode, which can lead to higher electron output, and therefore higher dose rates. The machine now has a new cathode, which allows a higher current rate up to 14 μAmps, and new accelerator tube. Also, the machine is very robust and can operate continuous experiments.

2.2 Dose Measurement and Calibration

In chapter I, we discussed about the fundamentals of dose measurement. For measuring and calibrating the doses used in our experiment, we created a step by step procedure. The steps we used to estimate the radiation dose are:

- E-Beam distribution measurement and calibration
- E-Beam measurement using a farmer ion chamber
- Dose calibration and measurement using radiochromic film
- Matching data of the farmer ion chamber and radiochromic film
- Estimate overall dose deposited in the liquid by matching experimental data and Monte-Carlo simulation data

2.2.1 E-Beam Distribution Measurement and Calibration

The main purpose of this step is to check the distribution of the E-Beam passing through the exit beam window. If the distribution is not centered we modify the path of the E-Beam using the bending magnet. **Fig. 2.6** describes this step in detail. We attached GAFCHROMIC® HD-810 radiochromic film (RCF) directly to the exit beam window of the machine. The RCF changes its color due to the exposure to the E-Beam and the intensity of the E-Beam is proportional to the color change of the film. Darker blue color indicates an E-Beam composed of dense electrons.

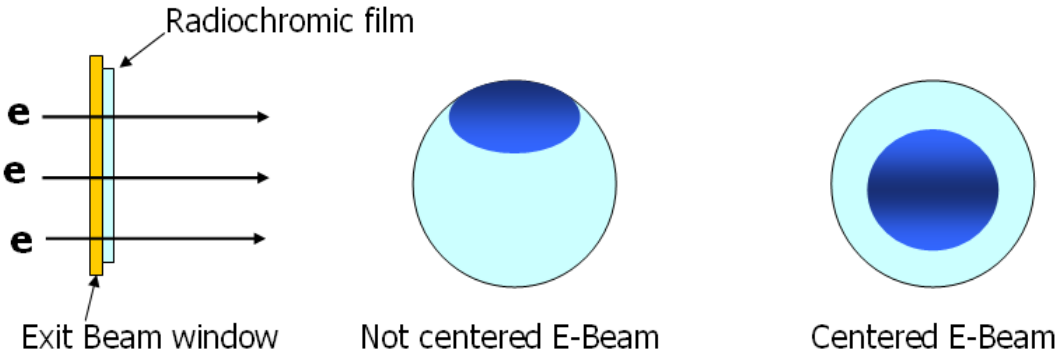

Fig. 2.6—RCF is directly attached to the exit beam window to check E-Beam distribution. When E-Beam passes through the RCF it changes the color of RCF. Darker blue color area of the RCF indicates that E-Beam passed through that area.

2.2.2 E-Beam Measurement Using a Farmer-Type Ion Chamber

As mentioned earlier, the radiation dose of E-Beam is measured with a farmer-type ion chamber (Markus Chamber, Type 23343). The Markus chamber is a well-known electron chamber widely used throughout the world. Developed by Prof. Markus at Göttingen University, Germany, it was the first high-performance ionization chamber for precise dose measurements of high-energy electron beams in radiation therapy. Its small sensitive volume and its waterproof construction make this chamber suitable for dose distribution measurements in a water phantom (Direct Scientific 2009). The underlying assumption for this measurement technique is that charged particle equilibrium (CPE) exists. In our experiment, however,

charged particle equilibrium is not valid since the electrons coming in to the reactor (aluminum can) cannot fully penetrate the fluid. The limited penetration depth of the E-Beam results in electrons coming in to the reactor stopping somewhere in the reactor's hydrocarbons.

Therefore, if we use this technique to report the radiation dose for the hydrocarbons in the reactor it cannot accurately represent the radiation energy absorbed in the hydrocarbons. However, we can use the number that we get from this technique as a reference nominal dose since this is the only accurate way of measuring and quantifying radiation dose using the current technique. Using this reference dose we are able to conduct radiation transport Monte-Carlo simulation to estimate the radiation dose distribution in the hydrocarbons, or average dose. **Fig. 2.7** shows the Markus chamber. This chamber has a volume of 0.055cc and measures a maximum dose of 50 Gy. We connected the chamber to the exposure meter (**Fig. 2.8)** and operated the E-Beam machine until the gauge indicated the maximum number.

Fig. 2.7—The Markus chamber has volume of 0.055cc and measure maximum dose of 50Gy. The membrane material is polyethylene of 0.03 mm thickness. The guard ring borders the measuring volume.

Fig. 2.8—Exposure meter measures exposure in the Markus chamber and provides measured value in röntgen (R). 1 R is $2.58 \times 10^{-4} C/kg$

Fig. 2.9 shows the parallel plate transmission ion chamber directly attached to the exit beam window. The ion chamber measures the charge C resulting from electrons passing through it. Point P is the location of the Markus chamber.

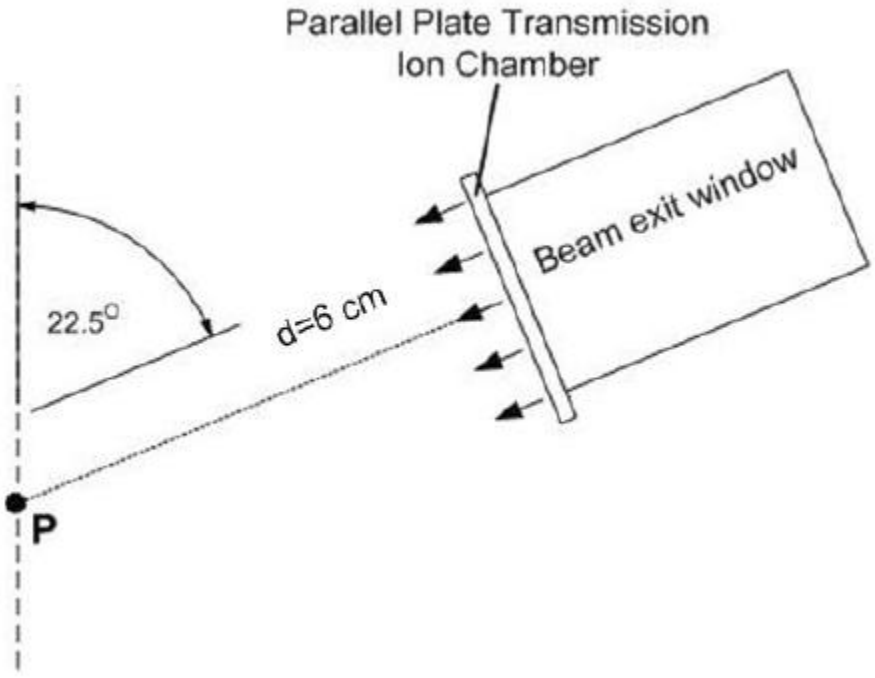

Fig. 2.9—Location of the Markus ion chamber (Point P) and the parallel plate transmission ion chamber (Zhussupov 2006).

From the control room, we operate and monitor the accelerator (**Fig. 2.10**) and read the charge measured from the parallel plate transmission ion chamber. We used 9V batteries connected in series to supply voltage to the parallel plate transmission ion chamber.

Fig. 2.10—Counter panel located in the control panel reads charge of electrons passing through the parallel plate transmission ion chamber.

After measuring the dose with the Markus chamber, we made a linear relation between the measured radiation dose and the charge measured from the parallel plate transmission ion chamber attached to the exit beam window (**Fig. 2.11**). Since we can measure a maximum dose of 50 Gy with the Markus chamber, extrapolating a higher dose requires extending the linear relation. Therefore, with the linear relation (**Fig. 2.11**) we were able to estimate a higher dose by reading the counter of the transmission ion chamber.

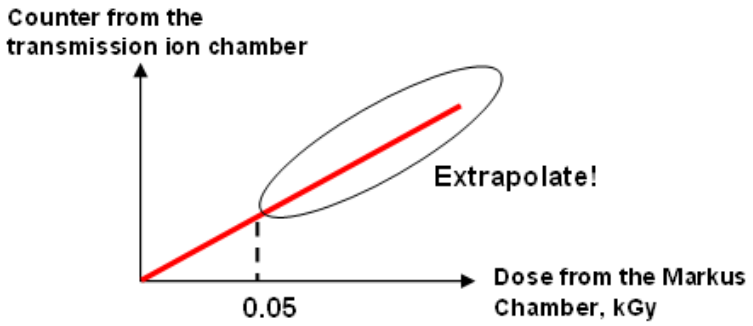

Fig. 2.11—Linear relation between radiation dose measured from the Markus chamber (Farmer-type ion chamber) and counter measured transmission ion chamber. With this relation we can extrapolate the relation after 50 Gy.

2.2.3 Dose Calibration and Measurement using Radiochromic Film

In the previous step we set up a linear relation between the transmission ion chamber and the Markus chamber to estimate radiation dose at point P. We can then estimate dose at any point in which we are interested. We used GAFCHROMIC® HD-810 (radiochromic film) to measure conveniently radiation dose in any area (**Fig. 2.12**). We attached several pieces of film inside the wall of the aluminum container to measure the dose. Especially, one film was placed in the same position where we placed the Markus chamber (farmer-type ion chamber). Therefore, we were able to set up a linear relation between the dose and the optical density of radiochromic film.

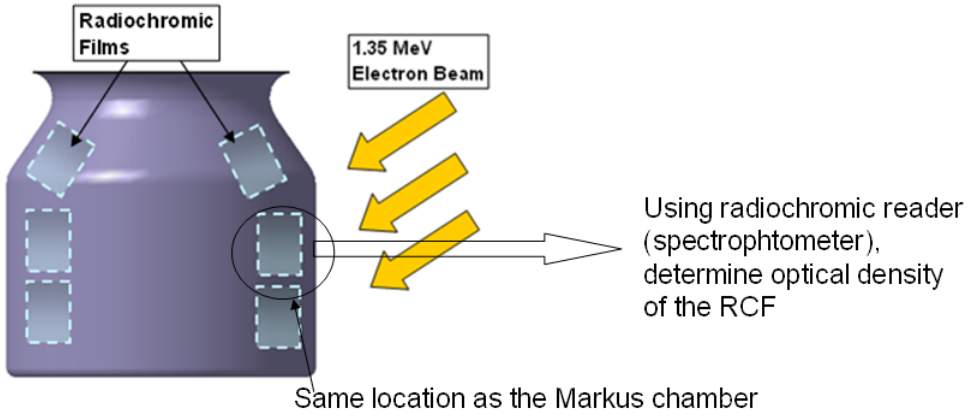

Fig. 2.12—Location of RCF and Marcus chamber (Famer ion chamber) (Kim and Yang 2009).

2.2.4 Matching Data of the Markus Chamber (Farmer ion chamber) and Radiochromic Film (RCF)

When electrons pass through the radiochromic film (RCF) they increase the optical density of RCF. We then can convert the optical density of RCF to dose (**Fig. 2.13**) with the linear relation between the counter of the transmission ion chamber and the radiation dose (**Fig. 2.11**). When we measure the optical density of RCF using a spectrophotometer it is important to start measuring it about 48 hours after the end of irradiation since this is the minimum saturation time of RCF.

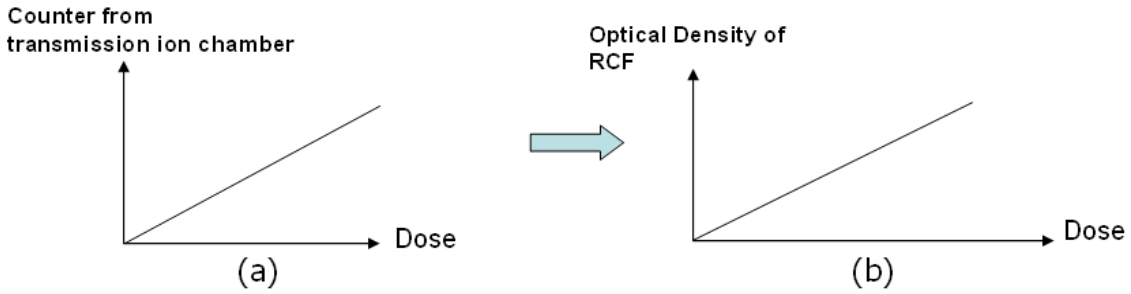

Fig. 2.13—Dose estimated from linear relation of the Markus chamber (a) can be compared with optical density of RCF (b). New linear relation (b) makes it possible to estimate radiation dose with RCF.

2.2.5 Estimate Overall Dose Deposited in the Liquid by Matching Measured Data and Monte-Carlo Simulation Data

Even though we are able to estimate the radiation dose at a point of our interest, we cannot estimate average dose in the object where the charged particle equilibrium (CPE) is not valid. To resolve this problem we estimated the average dose in the object by matching the measured data with the Monte-Carlo simulation data. **Fig. 2.14** shows the radiation dose distribution of the hydrocarbon sample from Monte-Carlo simulation. Notice that the dose in each layer is not uniform since the penetration of electrons in the hydrocarbon is limited. From the Markus chamber and RCF, we estimated the radiation dose of measuring points located on the outer and inner wall of the reactor. Using Monte-Carlo simulation, we determined the radiation dose distribution in the control volume (**Fig. 2.14**). Then we inputted the value of the measured dose into the geometry of Monte-Carlo simulation code. After inputting the value into the code, we ran the simulation and the computer will automatically calculate the average dose of the entire control volume by integrating the dose distribution in each layer.

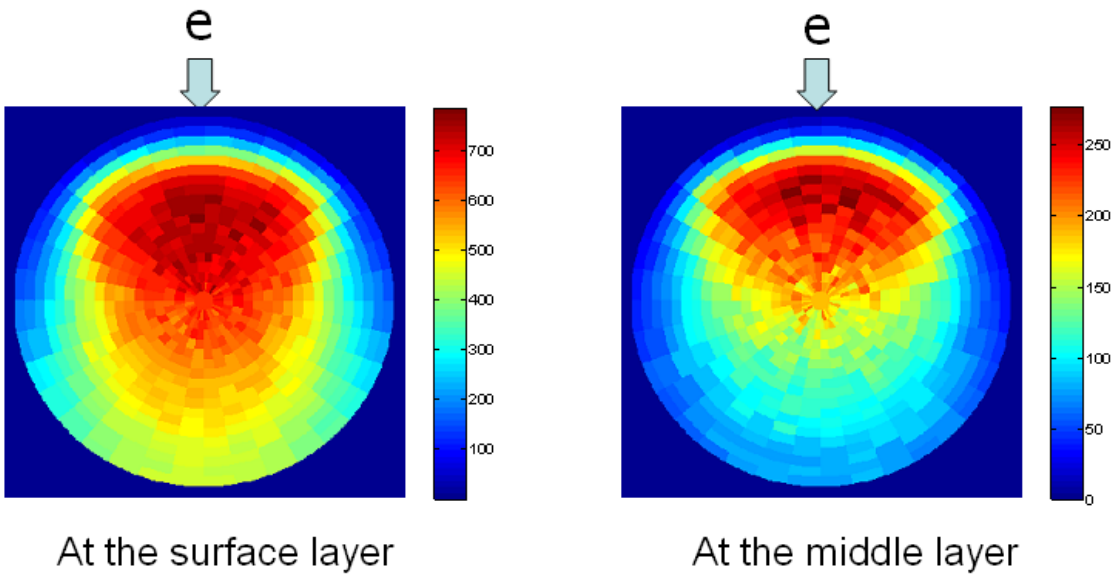

Fig. 2.14—Radiation dose distribution of asphaltene generated from Monte-Carlo simulation (top view) (Kim and Yang 2009).

2.3 Experimental Setup and Procedure

Fig. 2.15 describes the experimental setup for distillation of n-C_{16} and naphtha and cracking of asphaltene. An aluminum alloy reactor (oil container) is located on a heater that is placed in front of an E-Beam accelerator (VDG accelerator). The distillation unit is connected to the reactor, and the two thermocouples measure vapor temperature and copper base (bottom of the reactor) temperature. Since the bottom of the reactor is not flat we used a custom-made copper base which precisely fit the bottom of the reactor and inserted a thermocouple to measure the bottom temperature. The temperature data is transported to the data acquisition module every 10 seconds. A sampling bag is connected to a distillation unit to collect the non-condensable gases produced during the experiment.

Fig. 2.16 shows experimental setup for n-C_{16} and naphtha reflux. The setup is similar to **Fig. 2.15** but the main difference is that we used a reflux condenser to keep fluid in the reactor. After the experiment we collected the liquid sample in the reactor for chemical analysis.

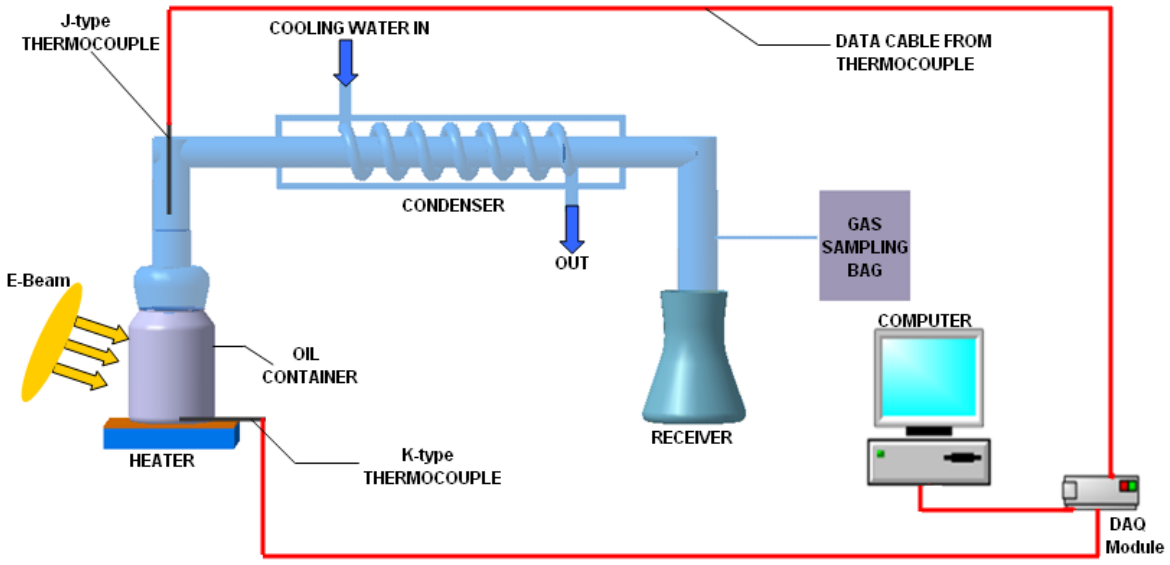

Fig. 2.15—Experimental setup for distillation of n-C_{16} and naphtha and cracking of asphaltene.

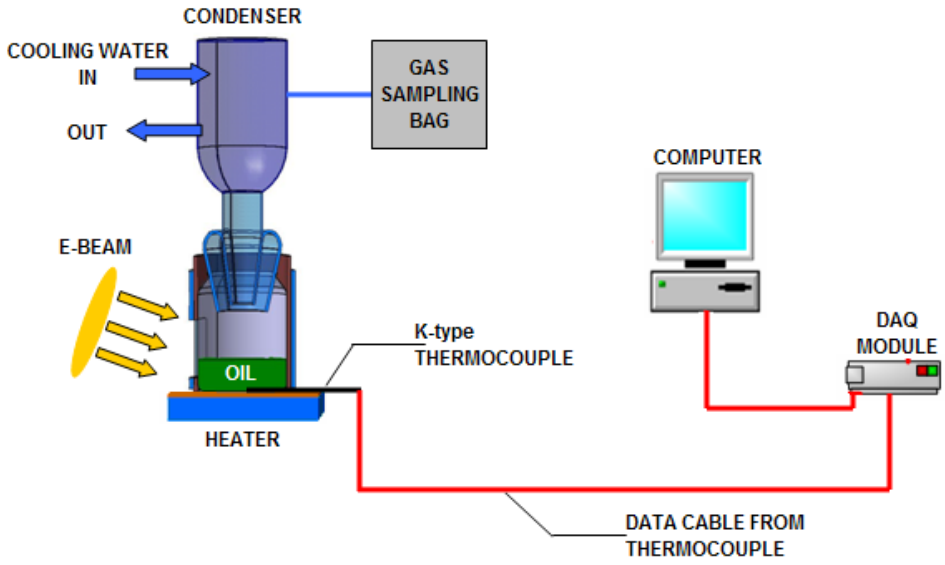

Fig. 2.16—Experimental setup for reflux of n-C_{16} and naphtha.

2.3.1 Design of Reactor

The objective of this work was to evaluate the effective radiation delivery in two different oil containers: aluminum can and glass flask. We measured the doses in several points of an aluminum can and a glass flask using the same measurement method used for dose calibration. To measure the effective delivery of the radiation dose we placed pieces of radiochromic film at the outside and inside the aluminum can and flask to determine the energy loss caused by differences in thickness and density. From the measurement, we found that the dose measured inside of the aluminum can is about 4% less than the one outside. However, the dose measured inside the glass flask is only 1/4 of the outside dose. This is because the thickness of the flask is 10 times that of the aluminum can. The result is that 3/4 of the radiation energy is absorbed or scattered at the wall of the flask. This is the main reason for choosing an aluminum can for the reactor since its wall thickness is very thin (0.2 mm), and allows transfer of most of the radiation energy to the inside of the reactor without the electrons losing a substantial amount of kinetic energy. We procured approximately 4000 12-oz aluminum cans and

4000 8-oz aluminum cans provided from the Crown Beverage Packaging Company of Mississippi.

2.3.2 Reactor Design Change

Throughout the course of our experiences, we made modifications to achieve an optimum reactor design. The main problems of the previous reactor (**Fig. 2.17**) were reproducibility and leaking. It used an expensive silicon rubber stopper to connect the reactor and the distillation unit. In addition, the silicon rubber stopper was glued to the aluminum can using a high temperature silicon gasket maker. Once we use a reactor for an experiment we had to make a new reactor with a new silicon rubber stopper. Furthermore, even though the aluminum can and the silicon rubber were glued together, vapor frequently leaked through the glued area.

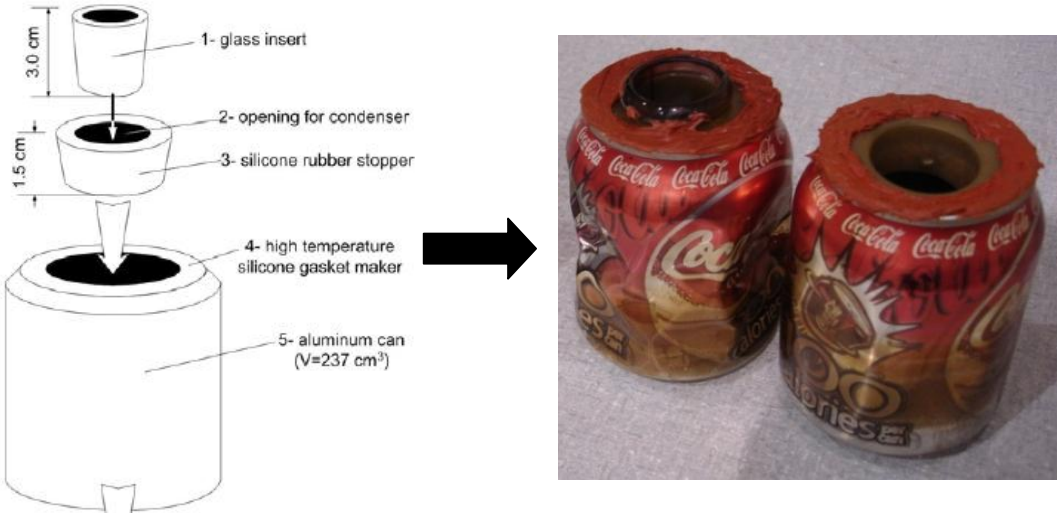

Fig. 2.17—Previous reactor design (Daniyar Zhusspov 2006).

The new design of the reactor included using a custom-made pyrex glass helmet which has a 24/40 female joint (Fortes Da Silva 2008). We covered the open top of the aluminum can with the glass helmet so we were able to insert the male 24/40 joint of the

distilling condenser into the female joint. The biggest concern in this design was leaking from the contact area between the glass helmet and the open top of the aluminum can. To solve this problem a thermal resistant silicon material was used to make a gasket and placed in between them. However, this did not work well; the silicon gasket started deforming as the temperature approached the high boiling point of n-C_{16} (287^{o}C). We then replaced silicon gasket with a thermal resistant rubber gasket. This gasket is designed to seal better than the silicon gasket. However, leaking started again as the n-C_{16} reached its BP. **Fig. 2.18** shows the leaking of n-C_{16} when using a silicon and rubber gasket.

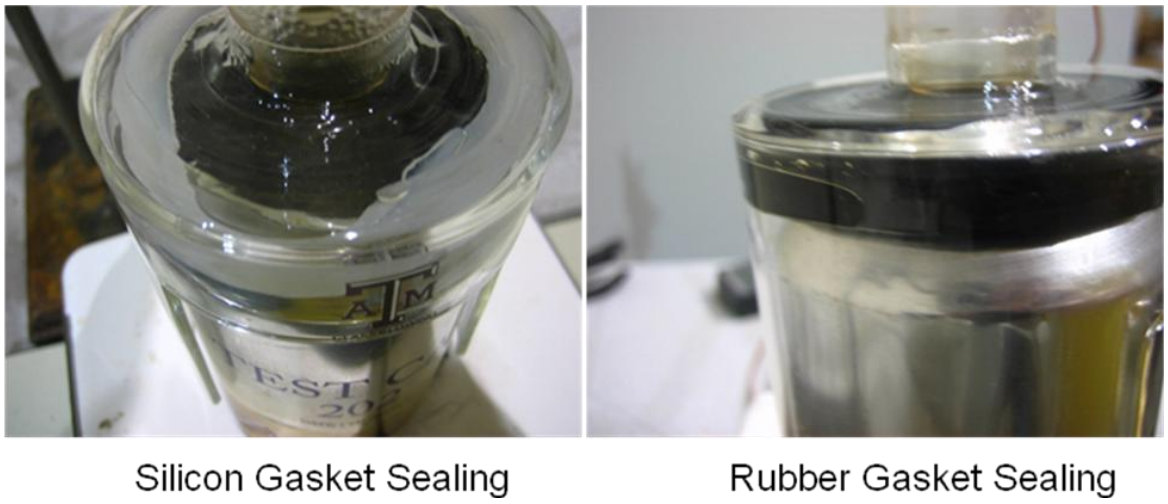

Fig. 2.18—Deformation of silicon and rubber gasket results in leakage of n-C_{16} in the reactor. Therefore, the result shows that silicon and rubber gasket cannot stay with boiling temperature of n-C_{16}.

To resolve the problems with the sealing gasket, we found new sealing materials called “style-760” which can function effectively up to 700 ^{o}C. The sealing gasket was then custom-made by Fluid Sealing Products Ltd (**Fig. 2.19**). However, this material was not very rubber-like so it required enough vertical pressure to seal the contact area. As a result, we arranged a special setup for the reactor to provide uniform vertical pressure to the helmet (**Fig. 2.20**) and then tried the leaking test again. However, at very high temperatures (500^{o}C of copper base temperature), the aluminum can started collapsing due to thermal stress and vertical stress, causing leakage. Therefore, we concluded that the gasket sealing method is not appropriate for sealing hydrocarbons with a high boiling point.

Fig. 2.19—Custom made gasket “style -760” can stay with maximum temperature of 700 ^{o}C.

Fig. 2.20—Custom made apparatus provides uniform pressure to seal the gasket in the contact area. However, aluminum can start collapsing when the fluid reaches high temperature because of thermal stress.

Another solution we proposed was to seal the contact area with a high temperature sealant. We found special sealing silicon sealant with very good thermal resistance (up to 400^{o}C). We glued the contact area with the silicon sealant (**Fig. 2.21**). Finally, we were able to prevent leaks at high temperatures. However, there was a problem with the glass helmet reactor design. In the reactor design, the inside of glass helmet must be glued to the open top of an aluminum can. Therefore, contamination of feedstock by the sealant material will be possible especially when distilling or cracking hydrocarbons at very high temperature. During the previous leaking test with n-C_{16}, small amounts of sealant material were found in the residue of the n-C_{16}.

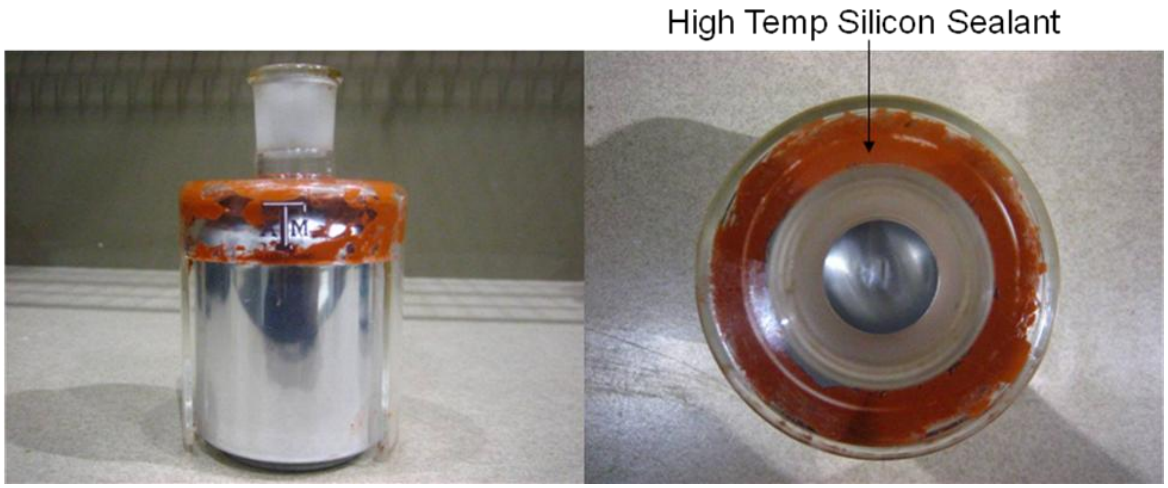

Fig. 2-21— High temperature silicon sealant is glued in the contact area. However, fluid in the reactor may contact with the sealant and get contaminated by the sealant.

A solution for this problem was to custom-make a glass joint which precisely fit the open top of aluminum can and then glue the outside of the contact area (**Fig. 2.22**) (Fortes Da Silva 2008). In the center of the customized glass joint, we connected 24/40 female glass joint into which we insert the male joint of the distilling condenser. As a result, contamination of the sealant material did not appear. The advantages of using the new reactor design include: (1) No contamination of sealant material since it is glued outside of contact area, (2) The curing time of the high temperature sealant is faster, and (3) It is easy to disassemble or reuse the glass.

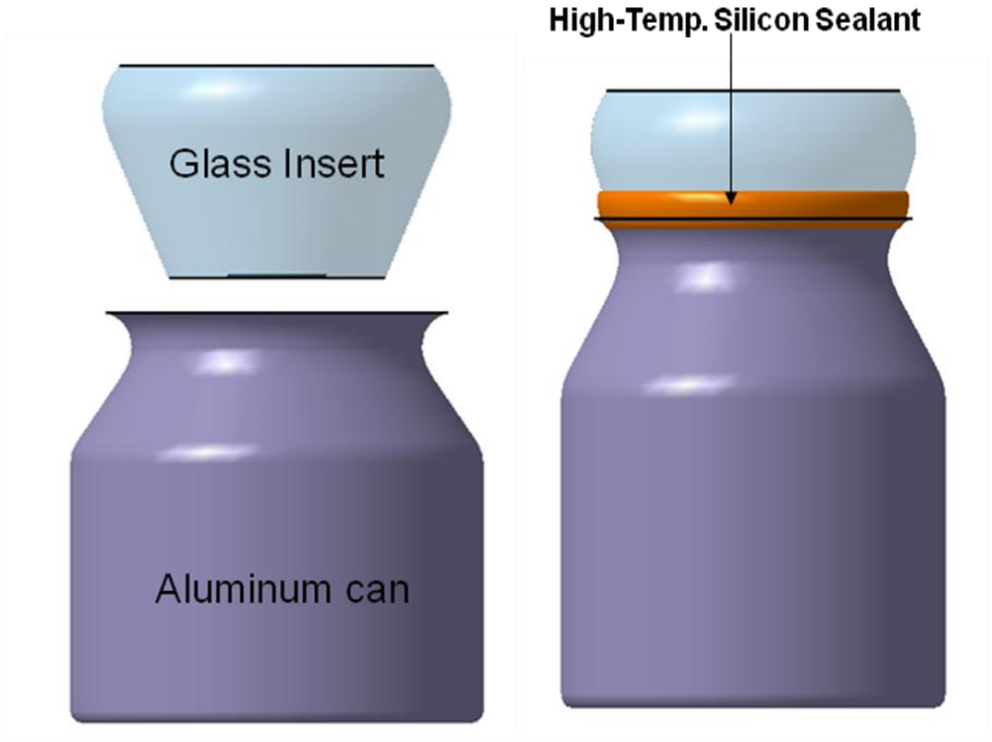

Fig. 2.22—Glass insert is perfectly fit to the aluminum can and high temperature resistant sealant is glued in the contact area.

2.3.3 Reactor Leaking Test

The purpose of leaking test is to check for any leakage during the experiment. Closure of the material balance and accurate component analysis are necessary for this process. Therefore, it is very important that there is no leakage during the experiments.

The following is the procedure for a leaking test.

1) Weigh the empty reactor and collector.
2) Weigh the reactor with feedstock.
3) Obtain the weight of the sample by difference. ($m_{feedstock} = m_{container+feedstock} - m_{container}$)
4) After the distillation test, weigh the mass of the feedstock left in the reactor and the mass collected in the collector
5) Weigh the condensates in the condenser.
7) Check mass balance

$$\text{Mass balance} = \frac{m_{collected-yield} + m_{condensate} + m_{feedtock-left}}{m_{feedstock(before-distillation)}}$$

8) Acceptable leaking test result is mass balance range of 99% ~ 100%

*Gases produced during the experiment are collected using a sampling bag however the mass of gases is too little so it can be ignored.

Table 2.1 shows an example of leaking test of hexadecane. We observed that some liquid drops remained in the condenser walls after collecting the liquid sample. This is because the low temperature of the condenser wall made the fluid more viscous to flow.

Table 2.1—Mass balance calculation of leaking test result.

Weight of collector, g	66.97
Weight of reactor, g	213.69
Weight of reactor + 100ml n-C_{16}, g	281.58
Weight of n-C_{16}, g	67.89
Weight of collector + yield, g	97.28
Weight of reactor + residual oil, g	250.82
Weight of yield, g	30.31
Weight of residual oil, g	37.13
Mass balance, %	99.3

2.3.4 Insulation of Reactor

The purpose of insulation was to minimize heat loss during the experiment. Since the reactor we used in the experiment was made of an aluminum can which has a very thin wall thickness, a substantial amount of heat loss occurred during the distillation process. Insulation of the reactor would minimize this heat loss. We determined the final design of an insulation jacket after several tests conducted for the purpose of minimizing errors and reducing variability. The custom made insulation jacket, as indicated in **Fig. 2.23** minimizes heat losses substantially. The insulation material, Waletex tape manufactured by Wale Apparatus, can withstand a temperature up to 2400^{o}F (1316^{o}C).

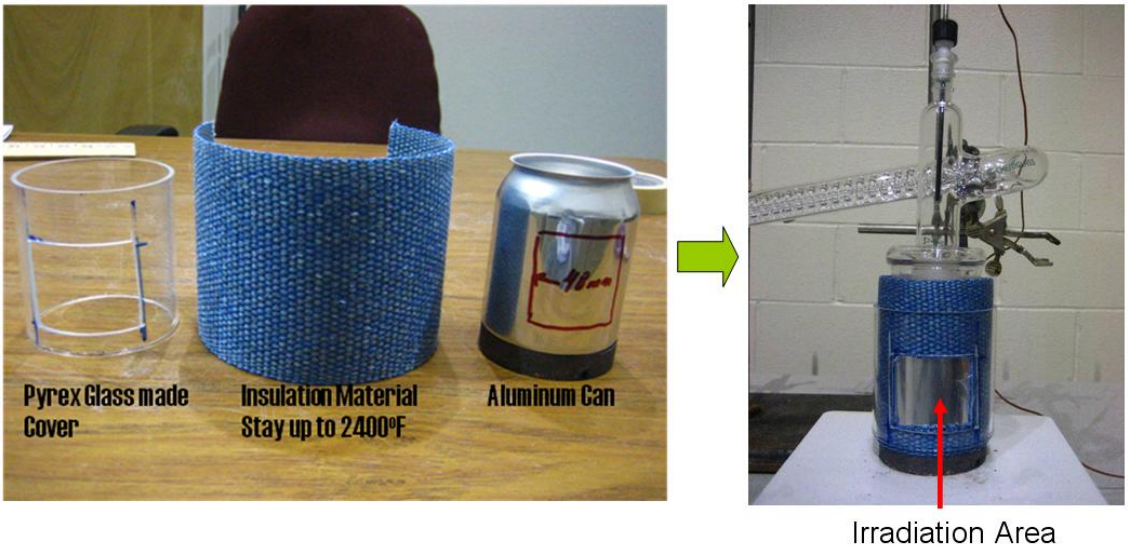

Fig. 2.23—Insulation of aluminum can is made of custom made pyrex glass cover and glass fiber.

2.4 N-Hexadecane Experiment

N-hexadecane is a very good model hydrocarbon for evaluating radiation effect on hydrocarbons since it is a pure component and a reference component of diesel. We used 99% n-C_{16} purchased from Sigma-Aldrich and conducted three experiments: radiolysis, distillation, and reflux. The main reason for using n-C_{16} for our first experiment was to compare our experimental results with the most recent n-C_{16} radiation experiment (Wu et al. 1997).

2.4.1 N-Hexadecane Radiolysis

We conducted liquid n-C_{16} radiolysis to investigate the effect of E-Beam irradiation at ambient temperature and atmospheric pressure. We prepared 2ml amber vials from VWR (P.N: 66030-084) which have non-hydrocarbon reactive septum inside the cap. Each amber vial was filled with 1ml n-C_{16}. We conducted two different experiments. First, we irradiated vials with a nominal dose of 500 Gy. Then we irradiated vials with a nominal dose of 1kGy (**Fig. 2.24**). Nominal dose is a theoretical

dose that we can measure at a point of our interest where electrons can penetrate. If our point of interest is a fluid volume inside a reactor then the dose absorbed in the entire volume of the fluid is always less than the nominal dose.

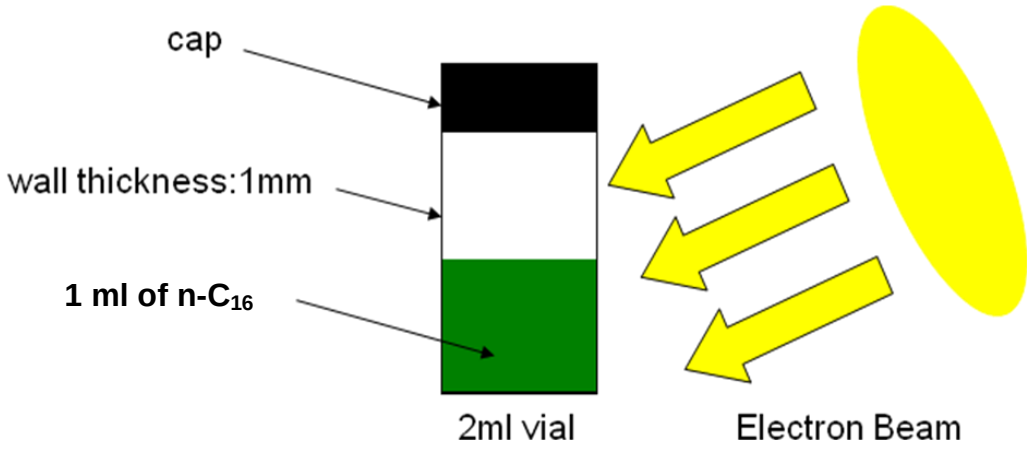

Fig. 2.24—2 ml of vial containing 1 ml of pure n-C_{16} is irradiated by electron beam.

We analyzed the composition of irradiated and non-irradiated samples using gas chromatography-mass spectrometry (GC-Mass) to observe the radiation effect on hydrocarbon. From the sample analysis, we found that the component distribution and composition of each irradiated and non-irradiated sample is identical. This result indicates that there was no composition change in irradiated n-C_{16} compared with non-irradiated n-C_{16}. Because the radiation dose was very low no composition change of the n-C_{16} occurred. Furthermore, the reported dose is a nominal dose which means the average dose in the n-C_{16} is even lower, since the glass wall of the vial substantially reduces the kinetic energy of electrons entering into the n-C_{16}. The density of the glass vial is approximately 2.3 g/cm^3, and the CSDA range of pyrex glass material when 1.35 MeV of an electron strikes the material is approximately 0.75 g/cm^2 (ESTAR 2009). This means that the electrons had already used a substantial amount of their kinetic energy to pass through the wall of the vial. Therefore, because our machine generates an

E-Beam of relatively low kinetic energy we had to use a thin wall reactor to deliver more electrons.

2.4.2 N-Hexadecane Distillation Experiment

We poured 80 ml of n-C_{16} into the reactor, and measured the total mass of the reactor. After building the distillation setup described earlier (**Fig. 2.15**), we turned on the heater, fixing 500^{o}C as the target copper base temperature. Simultaneously, we began irradiating. The distilled vapor was condensed by the condenser and then sent to the collector. The gas sampling bag (SKC foil bag) collected the non-condensable gas sample created during the experiment. We kept constant condenser temperature, 23^{o}C using water circulation pump. Since melting point of n-C_{16} is 18^{o}C we found that 23^{o}C is optimum condenser temperature to effectively collect the condensed liquid sample. We conducted two experiments, identical except for the fact that one was exposed to E-Beam radiation (**Fig. 2.25a**) while the other was not (**Fig. 2.25b**). We compared the results of each experiment to determine the radiation effect on the hydrocarbons. The absorbed dose for n-C_{16} radiation distillation was 0.35 kGy.

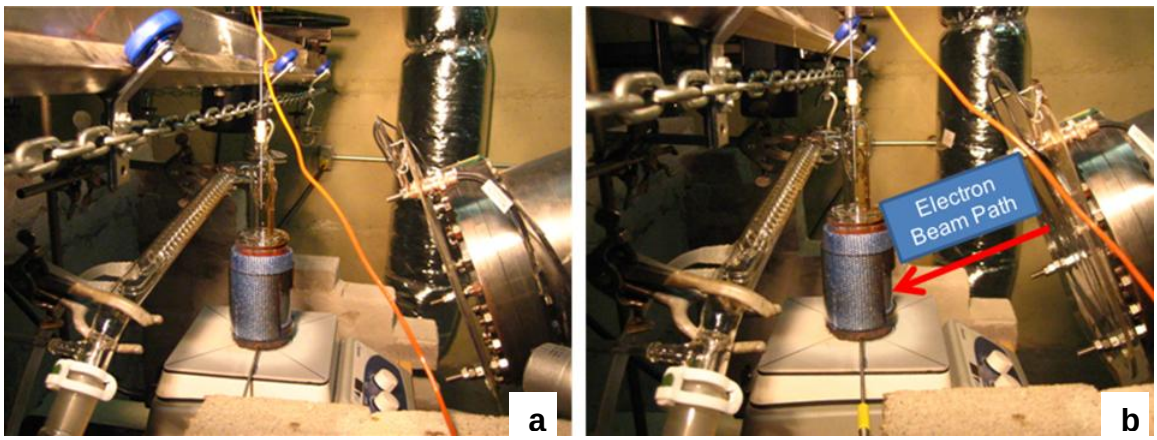

Fig. 2.25—Experiment (a): VDG machine is not operated; no electrons are provided. Experiment (b): VDG is operated; electrons are provided to the reactor.

N-C_{16} is a single hydrocarbon component which has a boiling point of 287^{o}C. In this experimental setup, when the n-C_{16} in the reactor reaches its boiling point, it begins to vaporize. The distilled vapor is condensed then due to heat transfer in the condenser and the distillate is collected. **Fig. 2.26** shows the distillation time of the thermal distillation and the radiation thermal distillation experiment. **Fig. 2.26** indicates that the time to distill 80 ml of hexadecane is different in the two experiments. The experiment using radiation takes a shorter time to distill n-C_{16}. This result illustrates that there was a radiation effect on the n-C_{16} that makes it achieve its boiling point more quickly. This is a significant finding because it suggests a way of minimizing the energy required to upgrade heavy oil since radiation energy provides a synergetic effect that lowers thermal energy needed to upgrade or refine oils. The very small energy of the absorbed radiation dose (0.35 kGy) made a big difference in distillation time. Also, this is a reliable result since we used pure n-C_{16} for our experiment; n-C_{16} is a single component hydrocarbon liquid that is not complex compared to multicomponent hydrocarbons. From the gas sample analysis using the GC-Mass, we analyzed and compared the components of the non-condensable gas samples after distillation with and without E-Beam. We found hydrogen content in the gas sample from the E-Beam experiment. However, no hydrogen was found in the gas sample that was not exposed to E-Beam radiation. Generally, C-H dissociation requiers a high thermal energy (Wu et al. 1997). However, C-H dissociation is the predominant reaction in hydrocarbon radiolysis. With the effect of electron beam radiation, C-H dissociation was easily occurred during the experiment. In addition, more olefins were formed in the gas sample with E-Beam than the one without E-Beam. Therefore, the results of the sample analysis, hydrogen and olefin formation, indicate that the electrons with high kinetic energy struck the n-C_{16} and transferred their energy by ionizing radiation during the radiation thermal distillation.

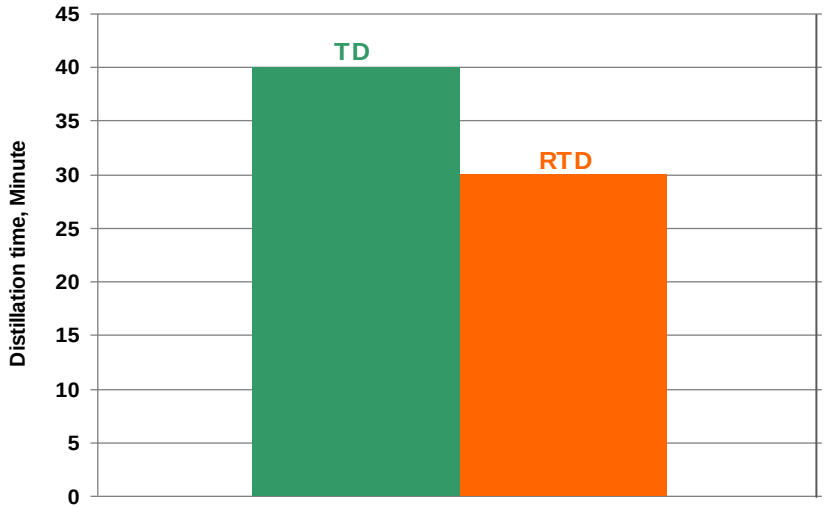

Fig. 2.26—Distillation Time Comparison: Distillation time to distill 80 ml of hexadecane with E-Beam radiation is 25% faster than the non radiation experiment (TD: Thermal Distillation, RTD: Radiation Thermal Distillation).

Experimental result comparison with reference

In 1997, the radiation effect on thermal cracking of n-C_{16} was studied by several researchers at the University of Tokyo (Wu et al. 1997). They conducted radiation thermal cracking of liquid phase and gas phase n-C_{16} using cobalt 60 γ-radiation in the temperature range of 300~400^{o}C. The results of our experiments were compared to the results from the University of Tokyo. Comparison between our experimental results and another experiment conducted using a different experimental setup and radiation source, might provide useful insights.

Wu et al. conducted RTC at 330^{o}C which indicates that their operation pressure was higher than our pressure (atmospheric pressure). According to the following PVT analysis using PVT SIM, we estimated the vapor pressure for the Japanese experiment as 45~50 psia (**Fig. 2.27**). Therefore, we found that our experiment was conducted under very conservative conditions compared to Wu's experimental work. **Table 2.2** shows a comparison of the two experimental conditions.

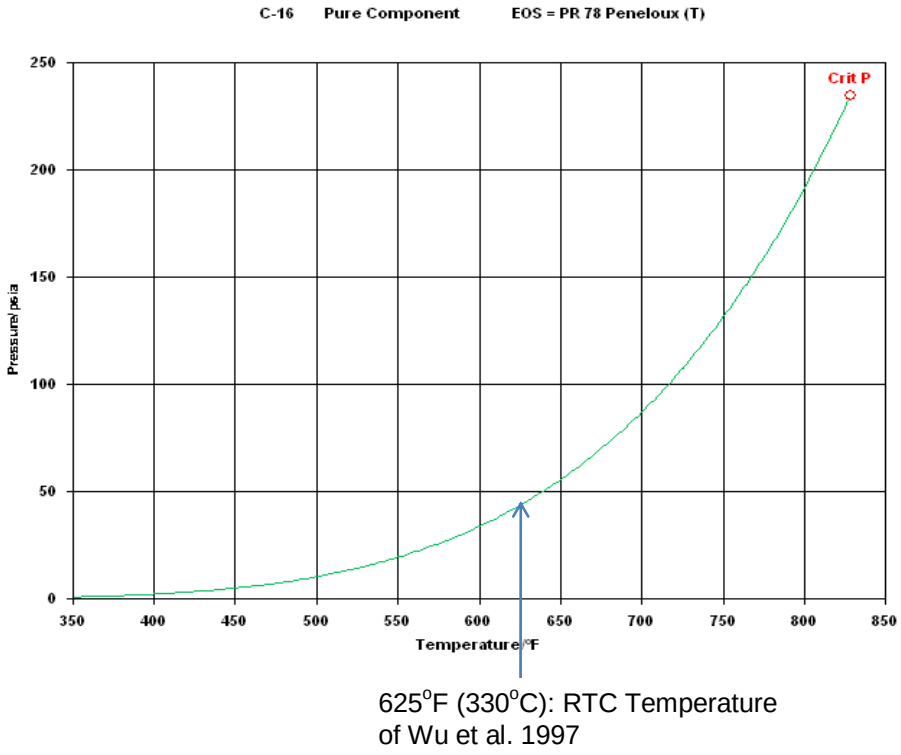

Fig. 2.27—n-C_{16} Pressure temperature curve generated from PVT sim.

Table 2.2—Comparison of two experimental conditions.

	Yang et al. 2008	Wu et al. 1997
Feedstock	n-Hexadecane 99%	n-Hexadecane 99%
Volume of C16, ml	80	5
Process	Radiation Assisted Distillation	Cracking using an ampule
Temperature, °C	287°C	330°C
Pressure, psia	14.6	45~50
Process Time, min	26	336
Radiation Source	Electron Beam	g-ray (cobalt 60)
Dose Rate, Gy/h	808	460
Dose, Gy	350	2576

We compared H_2 formation in our experiment and Wu's experiment. Since C-H dissociation is a unique feature of hydrocarbon radiolysis we were able to evaluate the

efficiency of each experiment by comparing H_2 generation. We calculated the H_2 formation rate constant of our results and Wu's results. The following assumptions were made when conducting the calculation.

1) Volume of gas per volume of liquid in Wu's result is proportional to the volume of gas per volume of liquid in our result.

$$\left(\frac{V_{Gas}}{V_{liquid}}\right)_{Yang} = \left(\frac{V_{Gas}}{V_{Liquid}}\right)_{Wu}, \quad \ldots\ldots\ldots\ldots\ldots\ldots\ldots\ldots\ldots\ldots\ldots\ldots\ldots\ldots\ldots\ldots \text{(2.1)}$$

2) Gases are mostly composed of methane (more than 95%).

3) Molar volume of gas is measured at standard condition (60^{o}F and 14.7psia).

From Wu's experimental results, the mass of the gas is 4% of the total mass of the liquid and gas mixture. Since mass does not change the mass of gas is 4% of the mass of the initial n-C_{16} liquid. Since we assumed that most of the gases are composed primarily of methane, the density and molar volume of the gas can be obtained from the methane density and methane molar volume at standard condition. Using the density and mass of the gas, the volume of gas collected in Wu's RTC experiment can be calculated. Then, using the volume of liquid and gas from Wu's experiment and the volume of liquid from our experiment, the volume of gas collected from the our experiment can be calculated from the first assumption above. We determined the hydrogen formation rate constant by using the following equation.

$$K_{H_2} = \frac{\dot{n}_{H_2}}{n_{C_{16}}} \text{ (lbmol/hr/lbmol of n-C}_{16}\text{)}, \quad \ldots\ldots\ldots\ldots\ldots\ldots\ldots\ldots\ldots\ldots\ldots \text{(2.2)}$$

where $\dot{n}_{H_2}$ is moles of hydrogen produced per hour.

$$n_{C_{16}} = \frac{\rho_{C_{16}} V_{C_{16}}}{M_{C_{16}}}, \quad \ldots\ldots\ldots\ldots\ldots\ldots\ldots\ldots\ldots\ldots\ldots\ldots\ldots\ldots\ldots\ldots\ldots\ldots\ldots\ldots \text{(2.3)}$$

$$n_{H2} = n_{gas} \times (mol\%)_{H2}, \quad \ldots\ldots\ldots\ldots\ldots\ldots\ldots\ldots\ldots\ldots\ldots\ldots\ldots\ldots\ldots\ldots\ldots\ldots \text{(2.4)}$$

where $(mol\%)_{H_2}$ is mol percent of hydrogen in the gas sample which we determined from the gas chromatography analysis.

We determined moles of gas from

$$n_{gas} = \frac{V_{gas}}{Vm_{gas}} \quad , \ldots\ldots\ldots\ldots\ldots\ldots\ldots\ldots\ldots\ldots\ldots\ldots\ldots\ldots \text{(2.5)}$$

where the volume of gas produced from our experiment is,

$$\left(V_{gas}\right)_{Yang} = \left(\frac{V_{gas}}{V}\right)_{Wu} \times \left(V_L\right)_{Yang} \quad , \ldots\ldots\ldots\ldots\ldots\ldots\ldots\ldots\ldots\ldots \text{(2.6)}$$

As mentioned previously, we used a very conservative approach when comparing our experiment with Wu's since the vapor pressure of our experiment is 3~4 times less than Wu's work. **Table 2.3** shows the result of our calculation. We found that the rate constant for our experiment is 20 times higher than Wu's. This result indicates that the E-Beam effect on hydrocarbon is more efficient than the γ-ray effect.

Table 2.3—H_2 rate constant calculation result

	Yang et al. 2008	Wu et al. 1997
n_{C16}, lbmole	5.88E-04	3.77E-05
V_{gas}, m^3	3.68E-03	2.28E-04
n_g, lbmole	3.32E-04	2.13E-05
n_{H2}, lbmole	2.98E-07	9.63E-10
K_{H2}, lbmole/h/lbmole of C16	**1.17E-03**	**5.90E-05**

2.5 Naphtha Experiment

2.5.1 Naphtha Distillation Experiment

Naphtha is a distillation cut with a boiling point range from 32^{o}C to 145^{o}C and carbon number ranging from C_4 to C_9. It consists of more than 50 components, and the naphtha was provided by TOTAL Petrochemicals research and technology center. We used the same experimental setup (**Fig. 2.15**) used for the n-C_{16} experiment and poured

100 ml of naphtha into the reactor. Then, we conducted a 1-hour thermal distillation (TD) and radiation thermal distillation (RTD) experiment since this is the optimum time for collecting enough distillation yield and residual sample. The temperature of copper base of the reactor was 180^{o}C, and the absorbed dose for the radiation experiment was 0.64 kGy.

Fig. 2.28 and **Fig. 2.29** show the vapor temperature profiles of the naphtha experiment with radiation and without radiation, respectively. By comparing the two graphs we can see that the vapor temperature of the radiation distillation experiment is higher than the one without radiation. Therefore, we can anticipate that the amount of distilled yield from the RTD experiment will be more than the yield from the TD experiment.

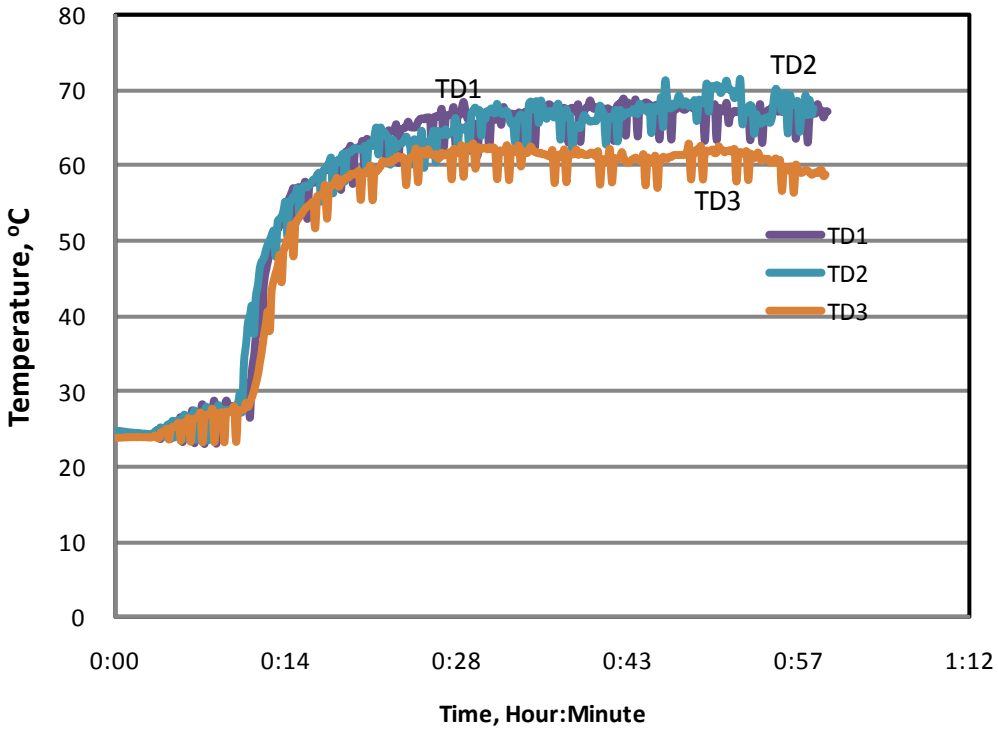

Fig. 2.28—Vapor temperature profiles of three TD experiments.

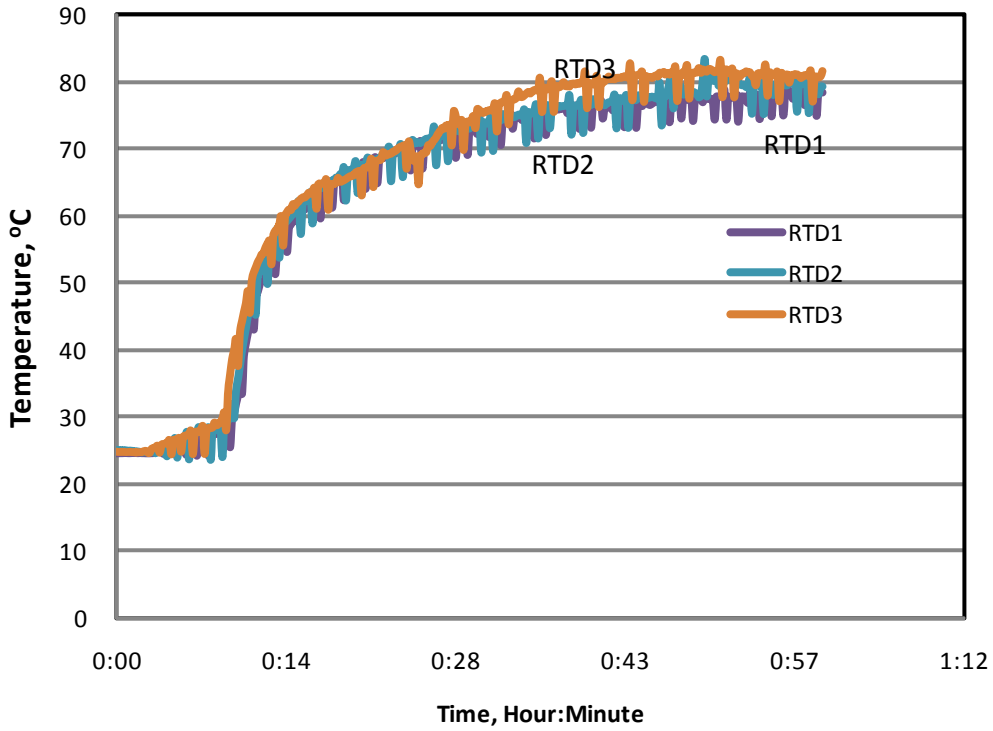

Fig. 2.29—Vapor temperature profiles of three RTD experiments.

Table 2.4 shows a summary of TD and RTD experiments. The average distilled yield of the RTD experiment increased by 17.5% compared to the TD experiment.

Table 2.4—Summary of TD and RTD experimental results (Distillate: liquid yield collected from the condenser during the distillation. Residue: liquid sample remained in the reactor after the distillation finished).

	Mass of distillate, g	Mass of residue,g	Fraction of yield, g	Estimated absorbed dose, kGy
TD1	26.84	39.95	0.40	-
TD2	27.74	39.89	0.41	-
TD3	26.32	40.4	0.39	-
Avg.	26.97	40.08	0.40	-
Std. dev.(σ)	0.587	0.228	0.006	-
RTD1	30.71	37.33	0.45	0.64
RTD2	31.17	35.62	0.47	0.69
RTD3	32.17	34.86	0.48	0.72
Avg.	31.35	35.94	0.47	0.68
Std. dev.(σ)	0.609	1.033	0.012	0.033

*Average increase in yield = $\frac{Y_{RTD} - Y_{TD}}{Y_{TD}} = \frac{0.47 - 0.40}{0.40} \times 100 = 17.5\%$

How can we account for this increase in vapor temperature? The experimental conditions for each experiment are identical except that we provided electrons for the radiation experiment. **Fig. 2.30** shows the average vapor temperature profiles of the TD and RTD experiments. The difference between the two temperature profiles began 10 minutes after the experiment began and peaked (15^{o}C) at the end of the experiment.

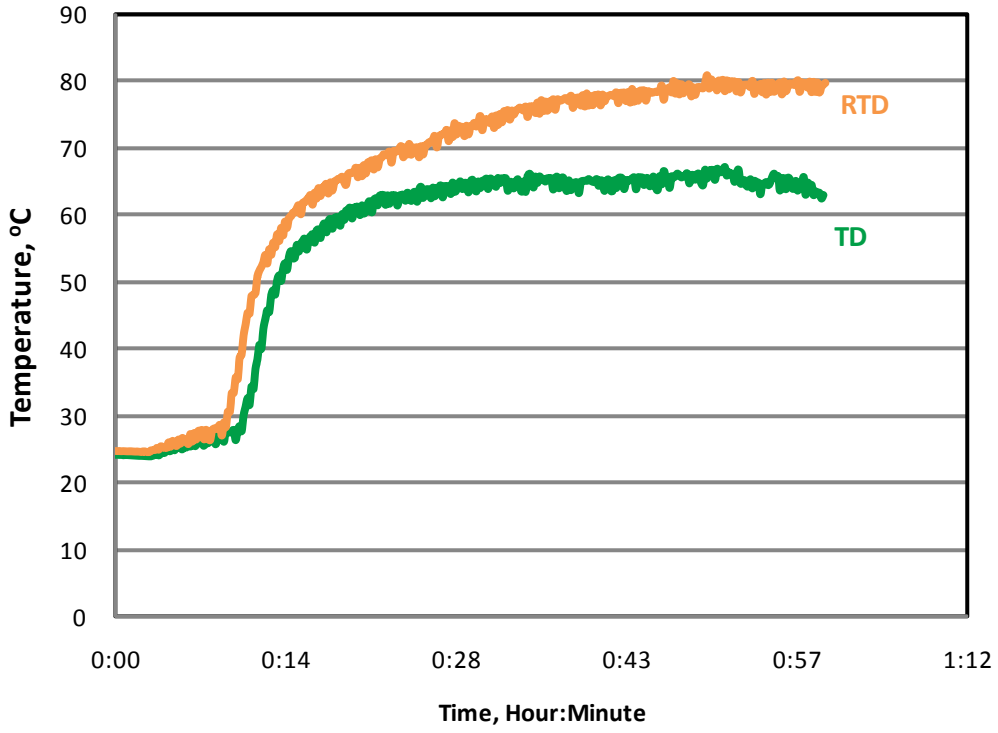

Fig. 2.30—Average vapor temperature profile of TD and RTD. The higher temperature profile suggests that exothermic reactions take place during RTD. The average absorbed Dose for RTD is 0.68 kGy.

Using the concepts of heat energy and dose, we can set up three equations to estimate the increase in vapor temperature that is attributable to radiation energy. In the equation,

$$\Delta Q = mc_p \Delta T \text{ , } \qquad (2.7)$$

ΔQ is the heat energy added to the substance due to ionizing radiation.

$$D = \frac{\varepsilon}{m} \text{ , } \qquad (2.8)$$

D is the absorbed dose and ε is the radiation energy deposited in the substance. Since we want to know the increase in temperature due to radiation energy, $\Delta Q = \varepsilon$. Therefore, the increase in temperature is,

$$\Delta T = \frac{\Delta Q}{mc_p} = \frac{Dm}{mc_p} = \frac{D}{c_p}, \quad \text{..... (2.9)}$$

From this calculation, we can see that 0.68 kGy of radiation energy, when converted to heat, can cause a maximum temperature increase of 0.3°C.

The values that we used for the calculation are very conservative, so the actual increase in temperature from radiation energy is somewhat lower than 0.3°C. This is because we had a change in the volume of naphtha (a moving boundary) during distillation so the electrons that would otherwise hit the upper area of the liquid phase naphtha could no longer transfer their entire radiation energy because the liquid phase naphtha that occupied that area vaporized. The density of vapor phase naphtha is much lower than that of liquid phase naphtha. Therefore, the high kinetic energy of electrons allow them to penetrate the vapor phase naphtha with the result that very little energy transfer occurred in the area of the vapor phase naphtha. In the case of the liquid phase naphtha, most of the electrons entering to the naphtha were absorbed.

However, even the value 0.3°C, which we consider as the maximum ΔT which can be achieved from the perfect energy transfer from the E-Beam radiation, is much lower than the increase in vapor temperature, 15°C.

We analyzed liquid and gas samples of naphtha TD1 and RTD1 and compared the composition of each sample. **Table 2.5** shows the result of the gas sample analysis, illustrating that the gas components generated from each TD1 and RTD1 are approximately the same. The only significant difference is that the formation of hydrogen in RTD is higher than that in TD which resulted from the radiation effect on C-H dissociation.

Table 2.5—Gas sample analysis of naphtha experiment indicates that component distributions of TD1 and RTD1 samples are relatively similar except for the composition of hydrogen. RTD1 produces 1.6 times more hydrogen than TD1.

Component, mol%	TD1	RTD1
hydrogen	3.82	6.21
carbon dioxide	0.26	0.52
iso-butane	0.00	0.00
n-butane	2.39	2.46
iso-pentane	55.13	53.25
n-pentane	38.19	37.57
cis-2-butene	0.22	0.00
Total	100	100

Table 2.6 shows the composition of the liquid naphtha sample. The table indicates that distillate of RTD1 has higher aromatics and less iso-parafins; apparently the RTD1 sample contains more undesirable components and less desirable components. However, the comparison is based on different distillate and residue. Since we collected more naphtha distillate from RTD1 it is evident that the compositions of TD1 and RTD1 are different. Therefore, we had to recombine the distillate and residue of each TD1 and RTD1 sample and recalculate a new component distribution after recombination.

Table 2.6—Composition of hydrocarbon groups in each sample. Distillate is collected yield from the distillation and residual is rest of naphtha remained in the reactor after the experiment. Control sample: no heat and no radiation.

Group, wt%	Control	TD1 Distillate	RTD1 Distillate	TD1 Residue	RTD1 Residue
Aromatics	8.05	1.93	2.70	15.37	16.01
Iso-Paraffins	35.15	43.50	41.69	28.88	28.97
Naphthenes	19.22	8.66	11.46	28.81	28.57
Olefins	0.09	0.44	0.38	0.00	0.00
Paraffins	37.50	45.48	43.78	26.94	26.46
Total	100	100	100	100	100

Table 2.7 shows the component distribution of the naphtha control, naphtha TD1, and naphtha RTD1 samples. As mentioned previously, we recombined the distillate and residue of TD1 and RTD1 samples to obtain a new overall composition and compared this result with the control sample, to which we did not apply any heat or radiation. Recombination calculation can be conducted using the composition of distillate and residue obtained from GC-Mass. In case of C_6 in aromatic group, recombined composition is calculated from

$$C_6 = \frac{[dwt\%]_{C_6} \times M_d + [rwt\%]_{C_6} \times M_r}{M_d + M_r}, \quad \text{..... (2.10)}$$

where $[dwt\%]_{C_6}$ and $[rwt\%]_{C_6}$ are weight percent of aromatic C_{16} distillate and residue respectively. M_d and M_r are mass of distillate and mass of residue. **Table 2.7** indicates that the component distributions of the control, TD1, and RTD1 samples are about the same which means that no composition change took place during the experiment. The only difference is the higher amount of distillate collected from RTD1. Therefore, what we observed from this experiment is that we obtained a higher vapor temperature profile from RTD, which indicates that the additional energy generated from the radiation effect on hydrocarbon increased vapor temperature. However, it did not change the composition of hydrocarbons. **Fig. 2.31** shows the reaction velocity constants for the decomposition of hydrocarbons. K_1 is the reaction velocity constant and this is calculated from

$$K_1 = \frac{1}{t} \ln \frac{a}{a - x}, \quad \text{..... (2.11)}$$

where t, a, x are time (sec), percentage of material in feed stock (a=100 for pure feedstock), and percentage of material that disappears during the reaction time t.

This graph indicates that decomposition of lighter hydrocarbons requires a higher temperature. Therefore, in our experimental setup, if we want to achieve a higher composition change of naphtha, such as cracking, to obtain lighter components, we need to either increase thermal energy or increase the amount of radiation absorbed in the hydrocarbon. The results of our naphtha experiment show that some of the lighter

components in naphtha usually reach their boiling points before the end of the experiment, and could not be irradiated during the entire experiment. This means that it is difficult for a naphtha sample to absorb a higher dose. To resolve this problem we proposed a reflux experiment which keeps all the liquid naphtha in the reactor during the entire experiment.

Table 2.7—Comparison of naphtha control sample and recombined naphtha TD1 and RTD1 samples show that component distribution of each sample is similar.

Group	Carbon Number	Control Sample wt%	TD1 wt%	RTD1 wt%
Aromatics	6	1.42	1.37	1.34
	7	4.30	4.21	4.25
	8	2.81	4.36	4.32
I-Paraffins	4	0.07	0.00	0.06
	5	9.40	8.91	9.03
	6	11.06	10.64	10.35
	7	7.74	7.50	7.55
	8	6.21	6.48	6.28
	9	0.95	1.26	1.54
Naphthenes	5	0.96	0.90	0.90
	6	6.46	6.31	6.15
	7	9.73	9.38	9.45
	8	2.44	3.28	3.35
	9	0.87	0.89	0.87
Olefins	5	0.07	0.06	0.18
Paraffins	4	2.32	1.99	2.09
	5	11.61	11.02	11.21
	6	9.80	9.53	9.23
	7	7.17	6.95	7.05
	8	3.57	3.91	3.78
	9	1.05	1.05	1.04
Total		100	100	100.02

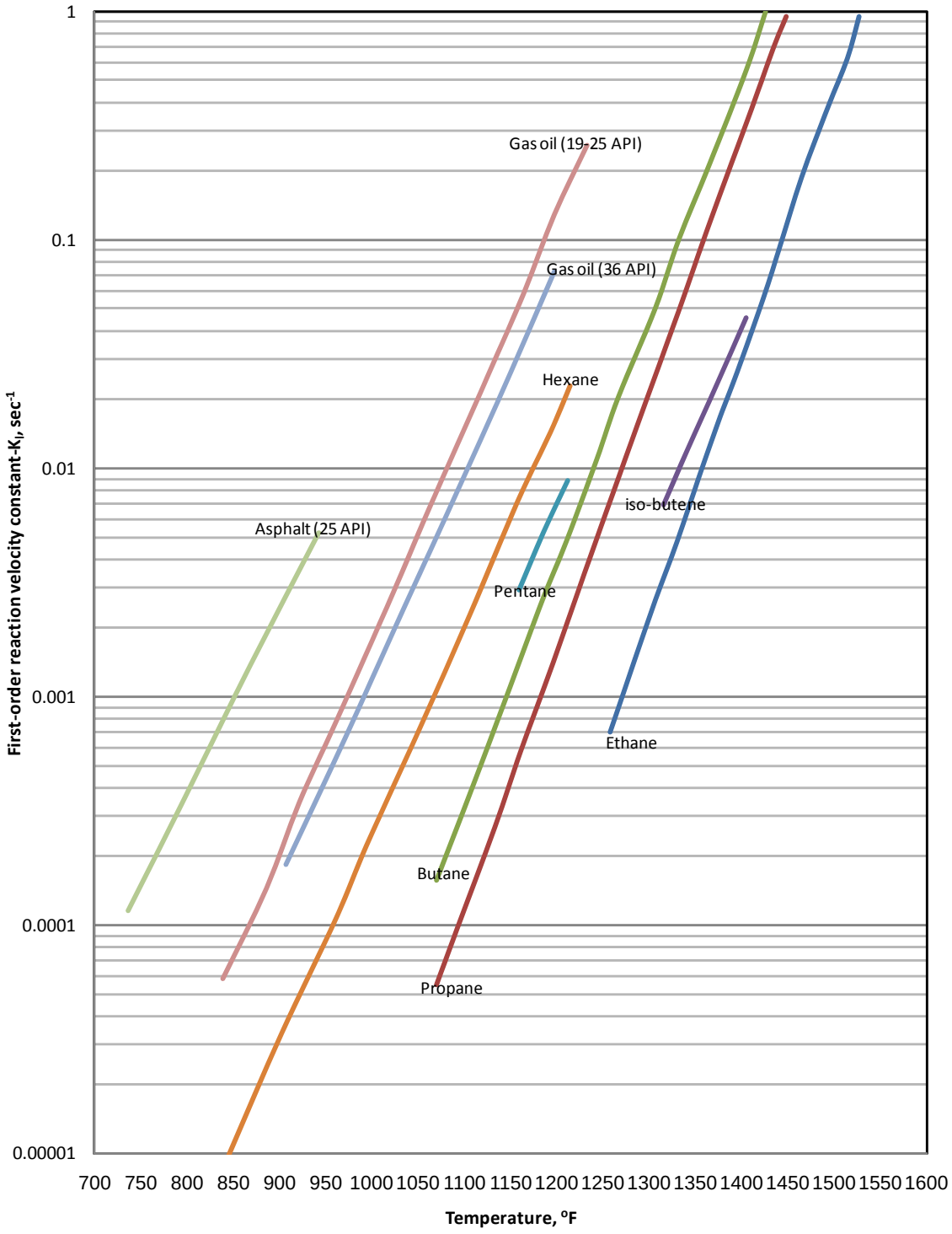

Fig. 2.31—Reaction velocity constants for the decomposition of hydrocarbons and petroleum fractions into various production (Nelson 1958).

Since the same amount of heat used in the two experiments (TD and RTD), we can estimate the additional energy generated from naphtha RTD that increased the distilled yield. We used the concept of enthalpy of vaporization. The heat used to vaporize each component is the integration of change in enthalpy multiplied by the change in the number of moles:

$$Q_i = \int_{n_o}^{n} \Delta H_{(vap)} dn, \quad \text{..... (2.12)}$$

Here, n_0 is the initial number of moles in the new phase and n is the final total number of moles in the new phase. We used the composition of liquid sample from GC-Mass to determine n and conducted a PVT simulation to calculate the enthalpy of vaporization for each component. Therefore, the total heat of vaporization is calculated from the sum of each Q_i:

$$Q_{total} = \sum Q_i \, , \quad \text{..... (2.13)}$$

In the case of TD1 and RTD1, we found that Q_{total} of RTD1 is 13.4% higher than that of TD1 (Q_{total} of TD1: 9.4 kJ, Q_{total} of RTD1: 10.6 kJ) and is similar to the increase in the distilled yield of RTD1, which is 12.5%.

Naphtha distillation with higher exposure

Another experiment we did with naphtha was a higher exposure experiment. During the previous naphtha experiment, we observed that a substantial amount of electrons struck the pyrex glass cover of the insulation jacket, thus losing most of their energy through scattering (**Fig. 2.32**). In order to achieve higher exposure, we removed the insulation jacket so the jacket would not block electrons. This allowed more electrons to enter the hydrocarbons, and we recorded the resulting radiation effect.

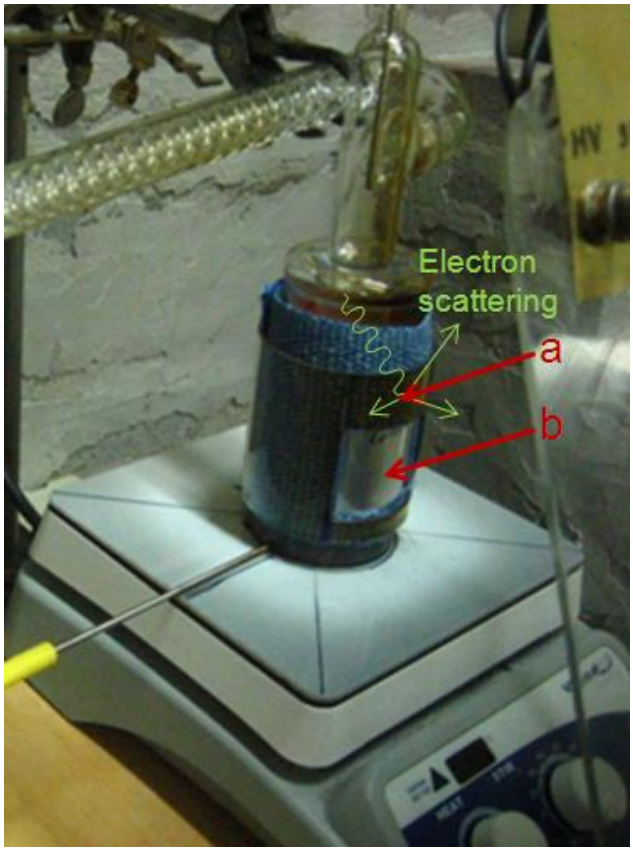

Fig. 2.32—Pyrex glass cover of the reactor blocks electrons coming in to the reactor (a). When electrons hit the thin wall of the reactor they can penetrate without loss of their kinetic energy (b).

Fig. 2.33 shows the result of the naphtha higher exposure experiment. As that figure shows, the difference between the vapor temperature profiles of the radiation and non-radiation experiments is higher than the difference recorded in previous experiment (**Fig. 2.30**).

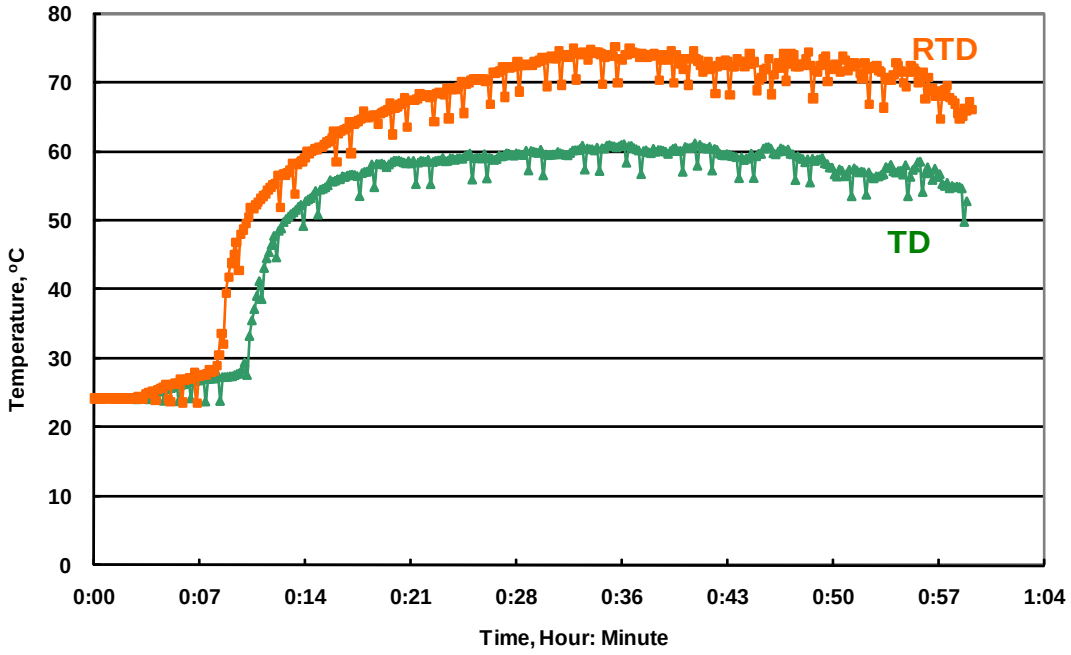

Fig. 2.33—Vapor temperature profile of higher exposure experiment indicates that difference between TD and RTD is higher than lower exposure experiment. Absorbed Dose for RTD is 0.89kGy.

We observed a 29.4% increase of distilled yield (**Table 2.8**) with radiation which illustrates that the radiation effect is proportional to the exposure. Therefore, when we have more electrons entering the hydrocarbons, radiation effect on hydrocarbons will increase.

Table 2.8—Summary of experiment indicates that RTD experiment obtained 29.4% more radiation dose compare to previous experiments (0.68kGy).

	Mass of distillate, g	Mass of residue,g	Fraction of yield, g	Estimated absorbed dose, kGy
TD	22.97	44.33	0.34	-
RTD	29.87	67.35	0.44	0.89

*Increase in yield = $\frac{Y_{RTD} - Y_{TD}}{Y_{TD}} = \frac{0.44 - 0.34}{0.34} \times 100 = 29.4\%$

We made a comparison of the two different sets of naphtha experiments, lower exposure and higher exposure (**Fig. 2.34**). With the vapor temperature data of the two naphtha experiments (TD and RTD of lower exposure and TD and RTD of higher exposure) we made a graph that shows ΔT with time. ΔT is the difference between the vapor temperature of RTD and the vapor temperature of TD. The graph indicates that ΔT of the higher exposure experiment is higher than that of the lower exposure experiment. Average ΔT is 9^{o}C and 12^{o}C, for the lower exposure and higher exposure experiments.

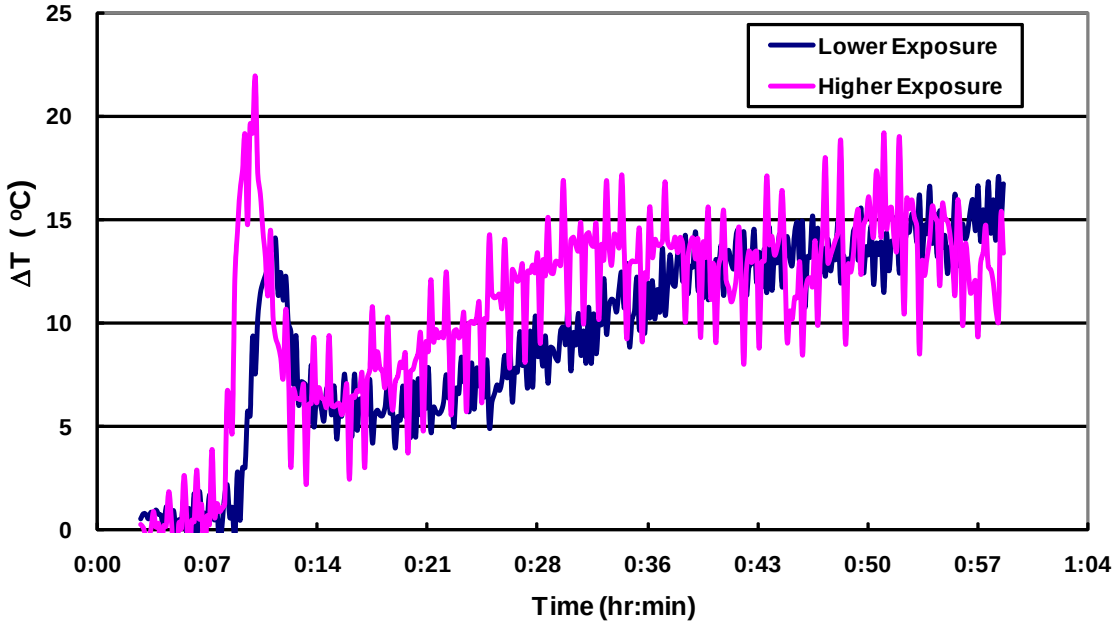

Fig. 2.34—ΔT is the difference between vapor temperature with radiation and without radiation. Average ΔT of higher exposure experiment is 25% higher than lower exposure experiment. Higher exposure resulted in higher temperature increase.

2.6 Asphaltene Experiment

The asphaltene content in a heavy oil sample plays a dominant role in determining its high viscosity. The strong attractive interactions among the asphaltene

particles at high asphaltene contents cause the heavy oil viscosity to increase dramatically (Luo et al. 2007). Therefore, it is important to investigate how E-Beam upgrading effectively converts asphaltene into better quality hydrocarbons.

Asphaltene is an extremely heavy and viscous product and it is almost solid at ambient temperature (**Fig. 2.35**). We used the same experimental apparatus (**Fig. 2.16**) that we used for the n-C_{16} and naphtha experimenst and conducted asphaltene cracking. The main difference between this experiment and the previous n-C_{16} and naphtha experiments is the cracking process. Since asphaltene has very heavy molecules we cannot collect distillates without breaking the heavy molecules. We used 22g of ashphaltene and conducted paralleled experiments for 2 hours with 500^{o}C of copper base temperature to crack the heavy asphaltene molecules. The light oils (distillates) from each cracking experiment were collected. We then compared the amount of yield (**Table 2.9 and 2.10**) and the component distribution of the liquid sample from GC-Mass. The absorbed dose for radiation thermal cracking (RTC) was around 3.1~3.2 kGy. We conducted three sets of TC and RTC experiments.

Fig. 2.35—Asphaltene sample at atmospheric condition

Table 2.9—Results of two hours of TC and RTC experiments with 500°C of copper base temperature.

	Mass of distillate, g	Mass of residue,g	Fraction of yield	Estimated absorbed dose, kGy
TC1	0	22	0.00	-
TC2	0.73	21.27	0.03	-
TC3	0.56	21.44	0.03	-
Avg.	0.43	21.57	0.02	-
Std. dev.(σ)	0.312	0.312	0.014	-
RTC1	1.09	20.91	0.05	3.1
RTC2	0.92	21.08	0.04	3.1
RTC3	0.87	21.13	0.04	3.2
Avg.	0.96	21.04	0.04	3.13
Std. dev.(σ)	0.094	0.094	0.004	0.047

From the comparison, we observed that the amounts of distillate for the three RTC experiments are similar (standard deviation: 0.064g). On the other hand, the TC experiments show uneven distribution for the mass of collected light oil sample (standard deviation: 0.312g). Even though we are encouraged by the fact that we collected more light oil from RTC experiments, the standard deviation of the TC results is too high. Therefore, we decided to ignore the first set of experiments for better comparison of the experimental results (**Table 2.10**).

Table 2.10—Results of TC and RTC experiments without the first set of experiment.

	Mass of distillate, g	Mass of residue,g	Fraction of yield	Estimated absorbed dose, kGy
TC1	0.73	21.27	0.03	-
TC2	0.56	21.44	0.03	-
Avg.	0.65	21.36	0.03	-
Std. dev.(σ)	0.069	0.069	0.003	-
RTC1	0.92	21.08	0.04	3.1
RTC2	0.87	21.13	0.04	3.2
Avg.	0.90	21.11	0.04	3.15
Std. dev.(σ)	0.020	0.020	0.001	0.041

*Average increase in yield = $\frac{Y_{RTD} - Y_{TD}}{Y_{TD}} = \frac{0.90 - 0.65}{0.65} \times 100 = 39\%$

The **Table 2.10** indicates that the average increase in yield of the RTC samples compared to the TC samples is around 39%. In addition, the GC-Mass analysis results (**Table 2.11 and Table 2.12**) show that the RTC samples contain more light components compared to the TC samples. These results indicate that cracking of asphaltene is enhanced with E-Beam irradiation. In addition, the formation of aromatics and isoparaffins (**Table 2.11**) indicates that the hydrocarbon quality of the RTC samples is better than that of the TC samples. The RTC samples have less aromatic components and higher isoparaffin components than the TC samples. As mentioned earlier, aromatic compounds in hydrocarbons have a very high tendency to undergo polycondensation reactions that lead to coke formation. Coke formation decreases the yield of the desired gasoline and other light oil fractions (Simanzhenkov, 2003). **Fig. 2.36** is an example of polycondensation reaction, and indicates that molecules of some products from thermal cracking reactions can sometimes be larger than feed molecules (Simanzhenkov, 2003).

Table 2.11—Average molecular weight and API gravity of each sample indicate that the RTC sample is lighter than the TC sample. In addition, there is significant decrease in the formation of aromatic components in the RTC sample compared to the TC sample. In terms of isoparaffin formation, the RTC sample contains 38% more isoparaffins than the TC sample which indicates the strong enhancement of isomerization.

	TC1	RTC1	TC2	RTC2
Avg. MW	98.60	84.89	99.02	82.03
Avg. API	65.19	79.90	65.85	83.30
Aromatics, mol%	9.17	3.65	9.21	3.13
I-Paraffins, mol%	25.85	57.13	27.09	63.89

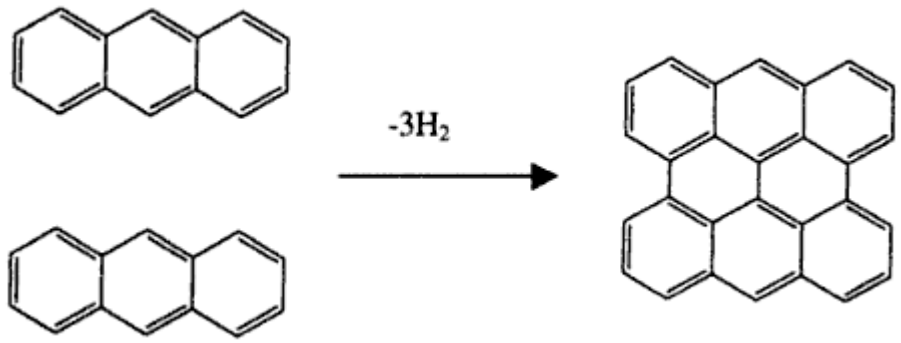

Fig. 2.36—Polycondensation reaction of aromatic compounds.

On the other hand, isoparaffins are very valuable components in hydrocarbons since they have a high octane rating. The octane rating determines the quality or resistance of gasoline and other fuels to the knocking “detonation” in spark-ignition internal combustion engines. Isomerization converts straight-chain paraffins to their branched-chain counterparts the component atoms of which are the same but are arranged in a different geometric structure. This conversion yields high octane hydrocarbon components.

Table 2.12—Components distribution of TC and RTC samples indicate that RTC sample have more light components compare to TC samples.

Group	Carbon Number	TC1 mol%	RTC1 mol%	TC2 mol%	RTC2 mol%
Aromatics	6	1.27	0.84	1.31	0.75
	7	1.29	0.76	1.38	0.62
	8	5.00	1.74	5.12	1.84
	9	0.91	-	1.40	0.23
	10	0.70	0.32	-	-
I-Paraffins	4	0.12	-	0.15	
	5	0.92	43.92	1.00	55.64
	6	2.89	2.15	3.07	1.96
	7	5.15	3.36	5.68	3.10
	8	10.49	6.32	10.74	4.39
	9	5.74	1.38	5.75	0.39
	10	0.55	-	0.71	-
Naphthene	5	0.42	0.39	0.44	0.24
	6	1.53	1.08	1.64	1.03
	7	2.71	1.25	2.51	1.07
	8	5.59	2.88	5.17	1.44
	9	1.83	0.68	1.83	0.64
	10	0.71	-	-	-
Olefins	4	1.22	0.48	1.31	0.69
	5	4.18	7.21	3.72	3.58
	6	7.45	4.65	7.46	4.31
	7	5.88	2.36	4.94	1.32
	8	2.25	0.42	2.88	0.32
	9	-	-	0.15	-
	10	0.41	-	0.34	-
Paraffin	3	0.38	0.34	0.52	0.40
	4	1.21	0.75	1.37	0.88
	5	3.52	2.21	3.37	2.48
	6	5.53	3.73	5.74	3.47
	7	7.77	5.03	8.04	4.09
	8	6.41	3.89	6.69	3.22
	9	3.23	1.56	3.04	1.48
	10	0.29	-	0.69	0.27
	11	0.12	-	0.15	-
Unidentified		2.20	-	1.74	0.20
Total		100	100	100	100

2.7 N-hexadecane and Naphtha Reflux Experiment

The main purpose of a reflux experiment is to achieve a higher and a uniform radiation dose by controlling residence time of fluid, because previous distillation experiments resulted in different radiation doses to the yield and residue. For example, when we conducted RTD of naphtha for one hour, approximately 70% of the mass of the naphtha stayed in the reactor which means that only 70% of the naphtha was irradiated for one hour. Then the rest of naphtha (30%) which was already distilled and collected had not been irradiated for one hour. Therefore, we had to modify the experimental procedure that would allow the radiation dose to effect the entire fluid evenly. After some discussion, we proposed an E-Beam reflux experimental setup (**Fig. 2.16**) since this would not allow fluid distillation. Using the apparatus, we conducted a reflux experiment with n-C_{16} and naphtha and analyzed the component distribution of the irradiated samples from GC-Mass.

2.7.1 N-Hexadecane Reflux Experiment

We used a reflux experimental setup (**Fig. 2.16**) and reduced the sample size to 50 ml in order to achieve higher radiation dose. Therefore, we expected to see the composition change of hydrocarbon molecules (cracking) caused by E-Beam irradiation. After building the experimental setup, we turned on the heater which fixing 500^{o}C as the target copper base temperature, and started irradiating at the same time. The n-C_{16} liquid stayed in the reactor for the two hours of the experiment, with the vaporized n-C_{16} condensing and dropping back into the reactor, a phenomenon called reflux. At the end of the experiment we collected liquid samples from the reactor for chemical analysis (GC-Mass). The absorbed dose for the n-C_{16} radiation experiment was 2.4 kGy.

Table 2.13 and **Table 2.14** show the component distribution of the liquid n-C_{16} sample after the experiment. The tables indicate that the component distribution of the TC and RTC samples were similar except for slight differences of C_{17+}. RTC samples have slightly higher C_{17+} components which illustrate that polymerization reactions were taking place during the E-Beam thermal cracking of hexadecane. During the RTC, n-C_{16}

breaks into free radicals and these radicals initiate chain reactions. The chain reactions not only generate lighter components but also generate heavier components due to polymerization.

Table 2.13—Comparison of component distribution for two hours of TC and RTC experiments. Radiation dose for the three RTC experiments was 2.4 kGy.

Carbon Number	TC1 wt%	RTC1 wt%	TC2 wt%	RTC2 wt%	TC3 wt%	RTC3 wt%
C5~C15	0.23	0.24	0.12	0.13	0.24	0.15
C16	99.35	99.42	99.39	92.55	99.29	96.50
C17+	0.42	0.35	0.49	7.32	0.46	3.36
Total	100	100	100	100	100	100

Table 2.14—Average component distribution of TC and RTC samples indicate that polymerization was taken place during RTC of n-C_{16}.

Carbon Number	TC wt%	Std. dev. (σ)	RTC wt%	Std. dev. (σ)
C5~C15	0.20	0.03	0.17	0.05
C16	99.34	0.01	96.16	2.82
C17+	0.46	0.04	3.68	2.85
Total	100		100	

Zaykin's group in 2004 also conducted radiation thermal cracking of highly paraffinic oil. They observed the high polymerization rate and low olefin content in products of radiation processing. They reported that alkyl radicals initiate polymerization and isomerization in heavy paraffin fractions. Therefore, degradation reactions compete with the reverse reactions of chain addition of alkyl radicals to the olefins.

We discussed the method of minimizing polymerization caused by alkyl radicals and found that 2,2,6,6-tetramethyl-piperidine-N-oxyl (Tempo) is a good inhibitor to suspend polymerization since it is able to capture alkyl radicals during the reaction. **Fig. 2.37** shows the reaction of Tempo with alkyl radicals. During the reaction, propagating

alkyl radicals are in dynamic equilibrium with the Tempo with the equilibrium constant *k*. A minimum temperature of 110°C is required to shift the equilibrium to the left (Toube and Schmidt-Naake 2001). However, if the reaction takes place at a very high temperature, the reversed reaction is favored which leads to the release of trapped alkyl radicals from the Tempo.

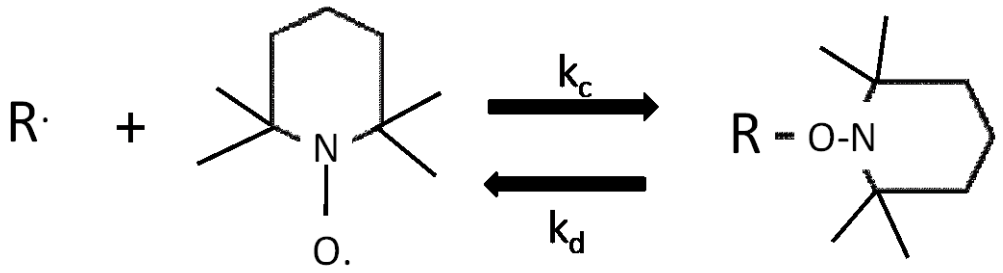

Fig. 2.37—During polymerization, the propagating alkyl radical $R^{\bullet}$ is in dynamic equilibrium with the Tempo (k_c = combination rate; k_d = dissociation rate).

In our n-C_{16} experiment, the reaction temperature reaches 287°C and the temperature of the copper base (bottom of the reactor) reaches 500°C. Therefore, it is evident that we are going to have reversed reactions that release a substantial amount of trapped alkyl radicals. This is the main reason for not selecting Tempo for a radical trap. However, if we reduce the sample size in order to achieve a higher radiation dose in the hydrocarbons then we may not need a high temperature to initiate C-C bond decomposition. This also creates ideal conditions for using Tempo to trap alkyl radicals.

2.7.1 Naphtha Reflux Experiment

Table 2.15 shows the experimental conditions for a naphtha reflux experiment. In this experiment we set two different temperatures for the copper base: 230°C and 327°C. The reason for setting two different temperatures was that we wanted to find the optimum temperature for maximizing the radiation effect on hydrocarbon. From the

hexadecane experiment, we found that C-H dissociation was enhanced by using E-Beam. However, it might result in a negative effect such as polymerization. Therefore, it is very important to find the optimum conditions which minimize the use of heat and radiation and maximize the upgrading of hydrocarbons.

We used the same experimental setup and sample size of the n-C_{16} reflux experiment. At the end of the experiment we collected liquid samples from the reactor for chemical analysis. The absorbed dose for naphtha radiation distillation was 2.6 KGy.

Table 2.15—Experimental conditions for naphtha reflux experiment.

	TC1	RTC1	TC2	RTC2
Heater Temp., ^{o}C	300	300	400	400
Copper Base Temp.,^{o}C	230	230	327	327
Radiation Dose, kGy	0.0	2.6	0.0	2.6
Reation Time, hr	0	2	0	2
Initial Mass, g	33.9	33.9	33.9	33.9

Table 2.16 shows the results of the naphtha gas sample analysis. RTC result of reflux#1 indicates that more hydrogen and iso-pentane were produced during the experiment. Even though the quantity was not substantial, it showed that hydrogen increased by 40% in RTC1 compared to TC1. So, we can expect that we may collect more olefins from RTC1. In terms of iso-pentane, its composition increased 2.5 times compared to its composition in TC1. In the result of reflux#2, both TC2 and RTC2 produced more hydrogen than reflux#1. However, the quantities of hydrogen produced from TC2 and RTC2 are almost the same. This may indicate that the radiation effect on naphtha at high temperatures is not significant since both TC and RTC provide similar results.

Table 2.16—Naphtha gas sample components conducted at two different temperatures. Reflux#1 was conducted at 230°C of copper base temperature. Reflux #2 was conducted at 327°C. Experimental time for each TC and RTC experiment was two hours.

	Reflux #1		Reflux #2	
component, mol%	TC1	RTC1	TC2	RTC2
hydrogen	0.63	0.89	18.58	18.52
nitrogen/carbon monoxide	-	-	-	-
methane		0.42		
carbon dioxide	0.22	0.29	6.07	1.70
ethylene				
ethane		0.49		1.30
propane	0.12	0.85		2.03
propylene		0.33		
iso-butane	1.08	6.06		
n-butane	32.23		18.10	35.07
trans-2-butene		0.38		
1-butene		0.29		
isobutylene				
cis-2-butene		1.70		
iso-pentane	35.06	88.30	28.06	19.53
n-pentane	30.66		29.18	21.85
1,3-butadiene				
Total	100.00	100.00	100.00	100.00

We also analyzed liquid samples of both reflux#1 and reflux#2 using GC-Mass. **Fig. 2.38** indicates that RTC1 has lighter components than TC1. API of RTC1 and TC1 is 68.7 and 65.5 respectively. **Fig. 2.38** shows that the biggest difference in the composition of TC1 and RTC1 is C5 formation. Therefore, E-Beam enhanced cracking of naphtha produced lighter components of naphtha molecules, especially pentane. From the gas sample analysis of reflux#1, we obtained 2.5 times more iso-pentane formation in gas sample of RTC1 than that of TC1. It is apparent that more iso-pentane formation generated from the gasification of iso-pentane occurred after cracking of naphtha. **Fig. 2.39** shows the component distribution of reflux#2. The trend of the component distribution of the reflux#2 experiment is similar to the previous result of the reflux#1

experiment. However, the difference between TC2 and RTC2 is not significant. Therefore, the E-Beam effect on cracking of naphtha is less efficient at high temperatures. This is because polymerization and cracking might take place simultaneously at high temperatures, a situation which we already experienced with the n-C_{16} reflux experiment.

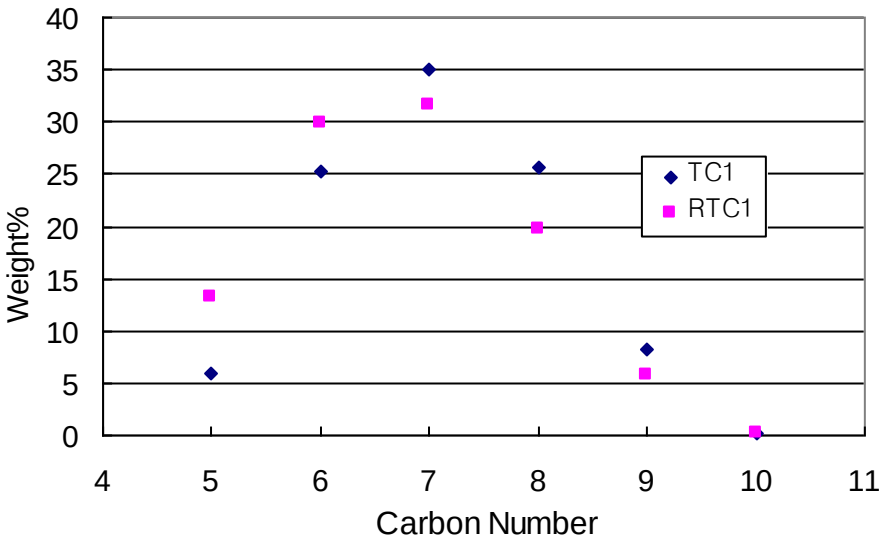

Fig. 2.38—Component distribution of TC1 and RTC1 sample indicates that cracking of liquid naphtha was enhanced by E-Beam irradiation.

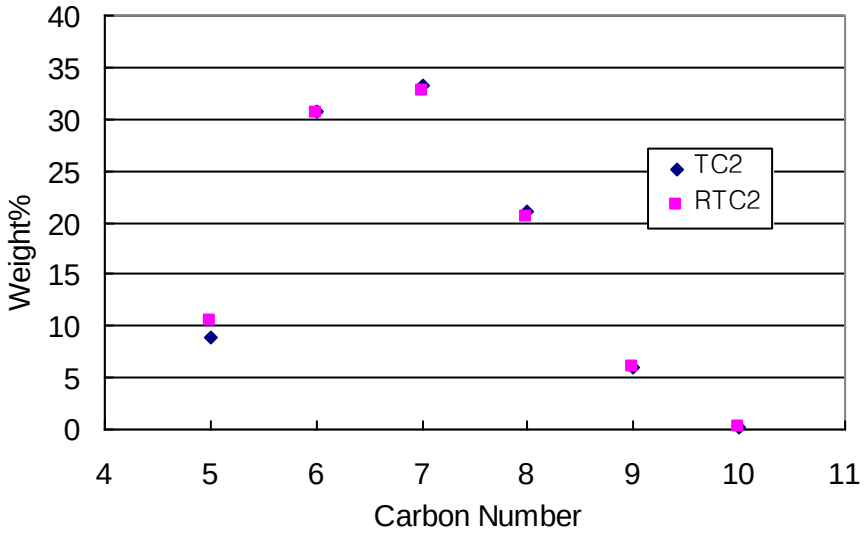

Fig. 2.39—Component distribution of TC2 and RTC2 sample indicates that cracking of liquid naphtha was taken placed during the experiment. However, radiation effect on hydrocarbon is not significant which means E-Beam radiation is not very efficient when we break naphtha molecules at high temperature.

Table 2.17 and **Table 2.18** show the composition of hydrocarbon groups in the naphtha samples. The results indicate that aromatic contents were reduced with E-Beam irradiation. From the asphaltene cracking experiment, we already observed that E-Beam significantly reduced aromatic components. Therefore, it is more apparent that reduction of aromatic contents is one of the unique features of E-Beam irradiation. As for olefin formation, the RTC sample has higher olefin formation, which we already expected from the gas sample analysis since the RTC sample has a higher hydrogen formation. Even though the quantity is not substantially higher, the RTC samples have slightly higher iso-paraffins and paraffins.

Table 2.17— Component distribution of TC and RTC samples indicate that RTC experiments generate more light components. In addition, radiation effect on cracking of naphtha is more efficient at lower temperature.

Group	Carbon Number	TC1 mol%	RTC1 mol%	TC2 Mol%	RTC2 Mol%
Aromatics	6	1.39	1.82	1.92	1.90
	7	5.42	4.81	5.19	5.04
	8	5.92	4.35	4.72	4.54
	9	0.34	0.09	0.09	0.13
I-Paraffins	5	2.16	5.21	2.66	3.59
	6	10.30	12.16	12.50	12.43
	7	8.98	7.85	8.39	8.17
	8	8.67	6.33	6.85	6.65
	9	3.59	2.50	2.70	2.61
	10	0.15	0.10	0.11	0.11
Naphthenes	5	0.74	1.19	1.13	1.09
	6	7.21	7.53	7.97	7.83
	7	11.66	9.98	10.72	10.45
	8	2.87	2.18	2.35	2.28
	9	1.07	0.68	0.74	0.72
Olefins	5	0.04	0.14	0.08	0.11
	6	0.02	0.04	0.04	0.03
Paraffin	4	-	-	-	-
	5	5.03	10.47	7.77	8.85
	6	9.85	11.04	11.58	11.40
	7	8.55	7.20	7.74	7.53
	8	4.81	3.52	3.82	3.69
	9	1.24	0.85	0.92	0.89
Unidentified	-	-	-	-	-
Total		100	100	100	100

Table 2.18—Composition of hydrocarbon groups in each sample shows that E-Beam reduces aromatic contents and increases olefins formation.

Group	TC1 mol%	RTC1 mol%	TC2 mol%	RTC2 mol%
Aromatics	13.06	11.06	11.93	11.61
I-Paraffins	33.85	34.13	33.21	33.54
Naphthenes	23.55	21.56	22.92	22.36
Olefins	0.06	0.18	0.12	0.14
Paraffin	29.48	33.08	31.83	32.35

CHAPTER III

ENERGY TRANSFER SIMULATION

Measuring radiation in fluid is more complicated than measuring radiation in solid objects because fluid moves during the reaction. Furthermore, if we provide heat during the process, the fluid moves more rapidly because of convection. In addition, the fluid density changes when we provide thermal energy because of thermal expansion. If some light components in crude oil vaporize during the radiation thermal or thermal process then the vapor and liquid phases will coexist in the system during the reaction, making it difficult to measure the accurate amount of radiation deposited in the fluid.

In this work, we conducted heat transfer and radiation transport simulation of n-C_{16} reflux experiment to estimate the amount of heat and radiation energy deposited in the fluid.

We collected simulation data from laboratory n-C_{16} reflux experiments. For thermal cracking, a heat transfer simulation was conducted using the computational fluid dynamics method. In the case of radiation thermal cracking, we used the results of the heat transfer simulation to conduct a Monte-Carlo radiation transport simulation. Because of the complexity of the process, we made some engineering approximations.

3.1 Heat Transfer Simulation

In this work, we used ANSYS CFX to conduct a heat transfer simulation. ANSYS CFX is a computational fluid dynamics (CFD) code well known for its high performance. Researchers around the world have applied it to solve a variety of fluid problems for over 20 years. With the highly parallelized solver, this code can solve many physical models such as laminar, turbulent, incompressible, fully compressible, isothermal, and non-isothermal with heat transfer by conduction, convection, and radiation. Since it has been used in the industry for a long time, it has superior bi-directional connections to all major CAD systems such as CATIA, Pro-E, and Solid

Works. Therefore, any sophisticated geometry can be analyzed with ANSYS CFX. In ANSYS CFX, the set of equations that describe the processes of momentum, heat, and mass transfer, known as the Navier-Stokes equations are solved by the finite volume technique (**ANSYS CFX Manual**). In addition, we used PVT SIM, a powerful fluid property program made by CalSep, to generate all the necessary fluid properties.

Fig. 3.1 shows the experimental setup of the n-C_{16} reflux experiment designed from CATIA V5. An aluminum alloy reactor covered with insulation material and pyrex glass is located on a heater that is placed in front of an E-Beam accelerator (VDG accelerator). Water with a temperature of 23^{o}C is circulated from a water tank to pyrex glass 1) to maintain a consistent temperature during the reaction. N-C_{16} begins in the liquid phase and vaporizes after reaching its boiling point.

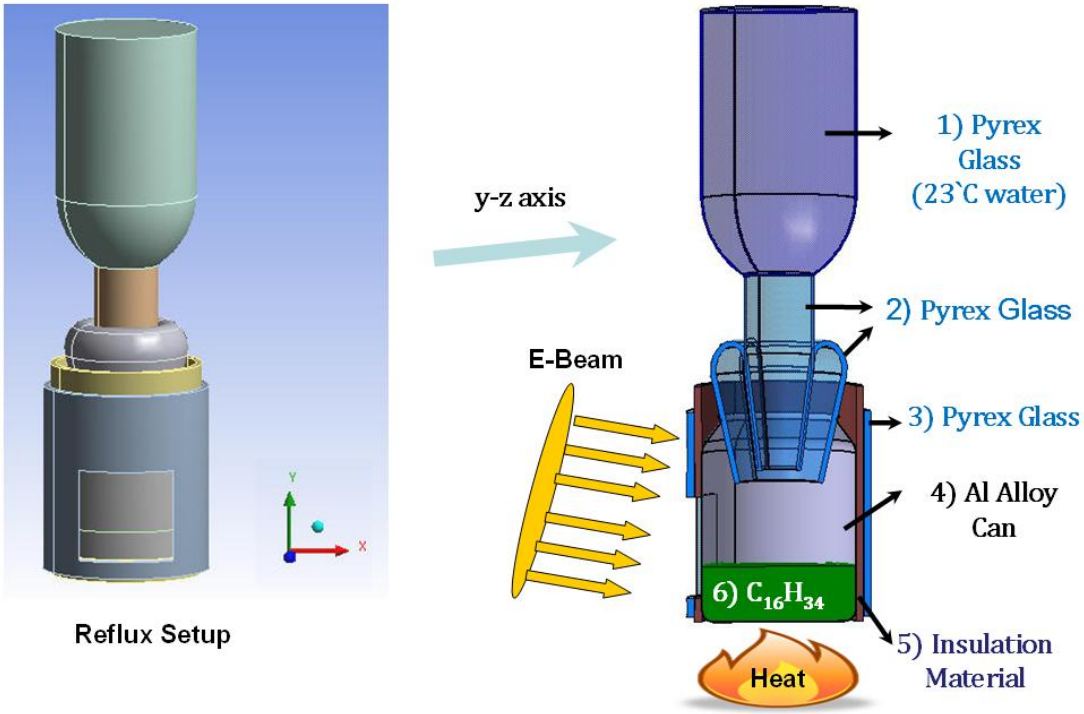

Fig. 3.1—Reflux experimental setup

The vapor phase n-C_{16} will then reach to the condenser filled with water and will condense. The condensed n-C_{16} will become n-C_{16} liquid droplets and fall into the liquid phase region. Therefore, pressure buildup caused by the thermal expansion of the n-C_{16} vapor would not occur in this system since the vapor is condensed by the condenser.

Fig. 3.2 shows copper base's temperature profile during the n-C_{16} reflux experiment. We used this profile to compute the heat flux at the bottom of the reactor. The copper base's temperature increases with time until the temperature reaches up to 500^{o}C, which takes approximately 17 minutes. After 17 minutes, the copper base temperature remains almost constant (500^{o}C) throughout the rest of the experiment. From the experiment, we found n-C_{16} vaporization begins after about 17 minutes. Therefore, we considered the time range from 0 to 17 minutes as a single phase period. From 17 to 20 minutes phase transition occurs because the n-C_{16} vaporizes. After 20 minutes, the system stays as a two-phase region where liquid and vapor co-exist. We divided our heat transfer simulation into two simulation conditions: single phase heat transfer from time 0 to 20 minutes and multiphase heat transfer after 20 minutes. In the case of the single phase heat transfer, the experimental results indicate (**Fig. 3.2**) that the temperature of the copper base increases with time. Therefore, we set this condition as transient, since the temperature changes with time. Once the copper base temperature reaches the targeted temperature (approximately 20 minutes) it ceases to change with time. Therefore, we set this condition as steady state.

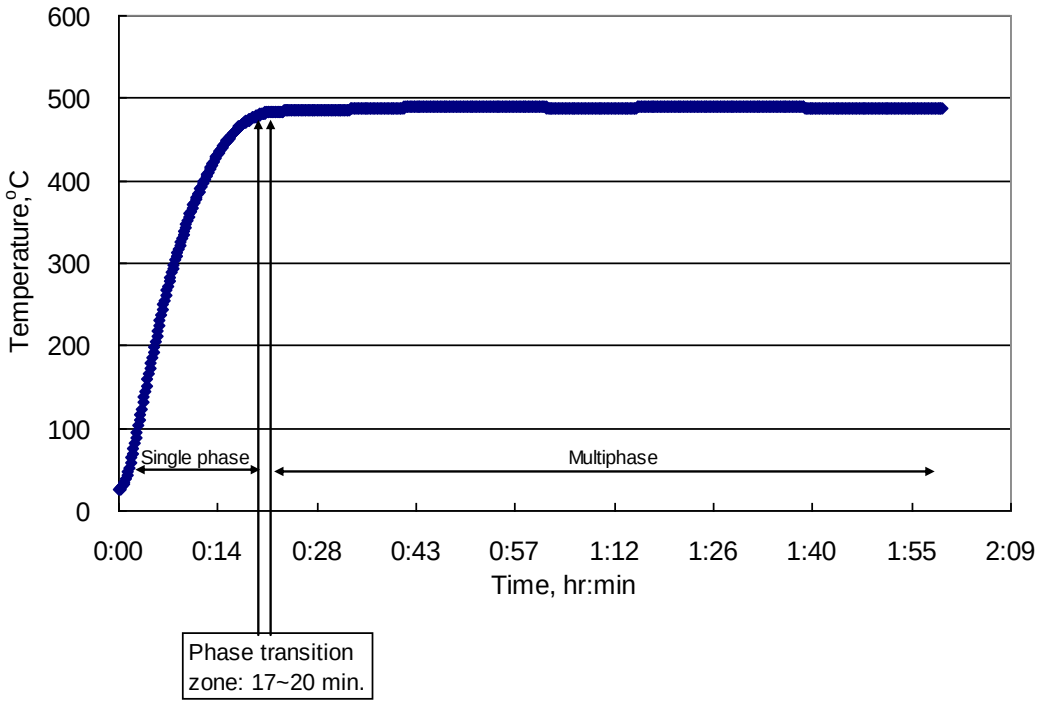

Fig. 3.2—Copper base (bottom of the reactor) temperature increases with time up to 17 minutes after the experiment. Then it becomes constant during the rest of experiment.

3.1.1 Single Phase Heat Transfer

Table 3.1 shows the simulation conditions of a single phase heat transfer. The simulated time for the single phase heat transfer is 1200 seconds. Since the aluminum alloy reactor is covered with both insulation material and pyrex glass, the boundary condition of the wall is insulation. **Fig 3.3** shows the control volume and its three boundaries (wall, bottom, and top). We selected a point in each boundary and compared the results from each point after the simulation. The boundary condition (B.C.) of the bottom is heat flux from the heater. The top of the fluid contacts with air resulting in fluid heat loss. The liquid phase n-C_{16} is initially at room temperature (23^{o}C) and has no fluid movement (the velocity of the liquid in the x, y, and z directions is zero).

Table 3.1—Simulation condition of single phase heat transfer

Simulation Time	1200 sec
B.C. of Wall	Insulated with fiber glass and pyrex glasss
B.C. of Bottom	Heat flux from the heater
B.C. of Top	Heat loss from air
Initial Condition	23°C of n-C_{16} liquid

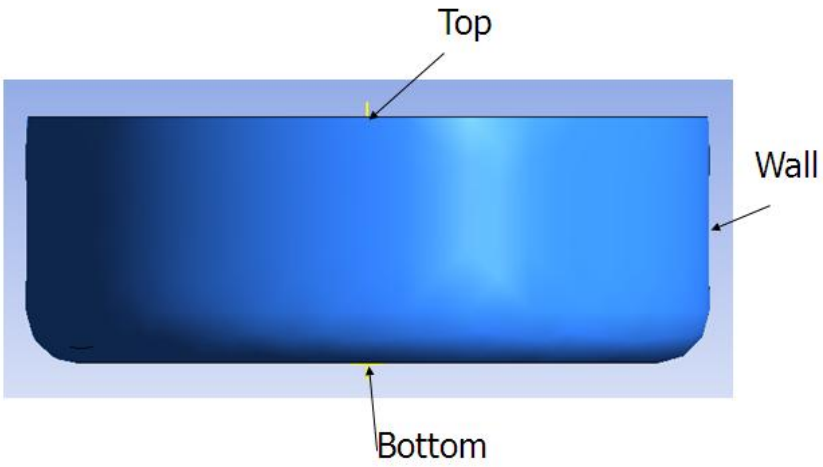

Fig. 3.3—Control volume of n-C_{16} single phase heat transfer.

Boundary Conditions at the Wall

The wall of the reactor is insulated. Therefore, calculation of the heat flow rate should consider all the insulated materials. We calculated heat flow rate in the wall using

$$q = UA\Delta T \,, \quad (3.1)$$

where U is overall coefficient of heat transfer that is calculated from

$$U = h_{overall} = \frac{1}{\left(\frac{1}{h_{fiber}} + \frac{1}{h_{pyrex}} + \frac{1}{h_{alcan}} + \frac{1}{h_{air}}\right)} \,, \quad (3.2)$$

The heat transfer coefficient of each component is calculated using

$$h_{wall} = \frac{k}{(d_o - d_i)} \,, \quad (3.3)$$

where k is the thermal conductivity of each wall material and d_o and di are inner and outer diameter of each wall. **Table 3.2** shows the values that we computed for the boundary conditions.

Table 3.2—Values for computing the boundary conditions at the wall.

	k, W/mmK	h, W/mm^{2}K	d_o-d_i, mm
Pyrex glass cover	1.10E-03	3.67E-04	3
Glass fiber insulation	4.00E-05	1.33E-05	3
Aluminum alloy can	1.75E-01	8.75E-01	0.2
Air	-	5.00E-06	-

Boundary Conditions at the Bottom

At the bottom of the reactor, we placed a heater to provide thermal energy. Therefore, the boundary condition of the bottom is heat flux provided from the heater. To estimate the heat flux from the heater, we first calculated the approximate heat energy using following equation.

$$Q = C_p m \Delta T \,, \quad (3.4)$$

We then calculated the heat flow rate using

$$q = Q / t \,, \quad (3.5)$$

Since we know the area of the bottom, the heat flux at the bottom is

$$q / A, \quad (3.6)$$

The heat flux value we calculated from the above equations is an estimated value. To determine the heat flux more accurately, we inserted the estimated heat flux value into our simulation model to generate a temperature profile of n-C_{16}. Then, we compared the temperature profile with the temperature profile of the n-C_{16} experiment. If the simulation result is lower than the experimental result, then we increased the estimated heat flux. If the temperature profile of the simulation is higher than the experimental result, then we decreased the estimated heat flux. After the computation work, we found that the simulated heat flux of 14000 W/m^2 closely matched the results of the n-C_{16} reflux experiment.

Boundary Conditions at the Top

The top of the liquid n-C_{16} has contact with air. Therefore, we used the heat transfer coefficient of natural convection of air to estimate the heat loss.

Thermodynamics Properties

The Redlich Kwong (R-K) equation of state (EOS), first published in 1949, is considered one of the most accurate two-parameter corresponding states EOS (**ANSYS manual**). This EOS is useful and convenient since it only requires fluid properties that users already know. Aungier (1995) modified the R-K EOS by adding an additional parameter *c* so that the equation provides much better accuracy near the critical point (**ANSYS manual**). ANSYS CFX uses this modified R-K EOS, which is expressed as

$$P = \frac{RT}{V_m - b + c} - \frac{a(T)}{V_m(V_m + b)}, \quad \text{(3.7)}$$

where V_m is molar volume and *a*, *b*, and *c* are parameters. The parameters are determined by

$$a = a_0\left(\frac{T}{T_c}\right)^{-n}, \quad \text{(3.8)}$$

where *n* is

$$n = 0.4986 + 1.2735\omega + 0.4754\omega^2, \quad \text{(3.9)}$$

$$a_0 = \frac{0.42747\, R^2 T_c^2}{P_c}, \ldots\ldots (3.10)$$

$$b = \frac{0.08664\, R T_c}{P_c}, \ldots\ldots (3.11)$$

$$c = \frac{R T_c}{P_c + \dfrac{a_0}{v_c (v_c + b)}} + b - v_c, \ldots\ldots (3.12)$$

To calculate specific heat capacity (C_p) we used the Redlich Kwong polynomial, defined as

$$C_p / R = a_1 + a_2 T + a_3 T^2 + a_4 T^3 + a_5 T^4, \ldots\ldots (3.13)$$

where R is the gas constant and T is temperature. We used PVT SIM to determine the coefficients of the above equation.

Simulation Results

Fig. 3.4 shows the temperature profiles n-C_{16} at three different locations. Since we computed constant heat flux for a simulation condition the bottom temperature increases with time. After 20 minutes the n-C_{16} reaches its boiling point of 287°C. The temperature profiles of the wall and top are the same as that of the copper base because of convection. **Fig. 3.5** shows that the density the n-C_{16} decreases with time. This is because the volume of the n-C_{16} increases due to thermal expansion. The density profiles of the wall and top are also almost the same as the profile of the bottom.

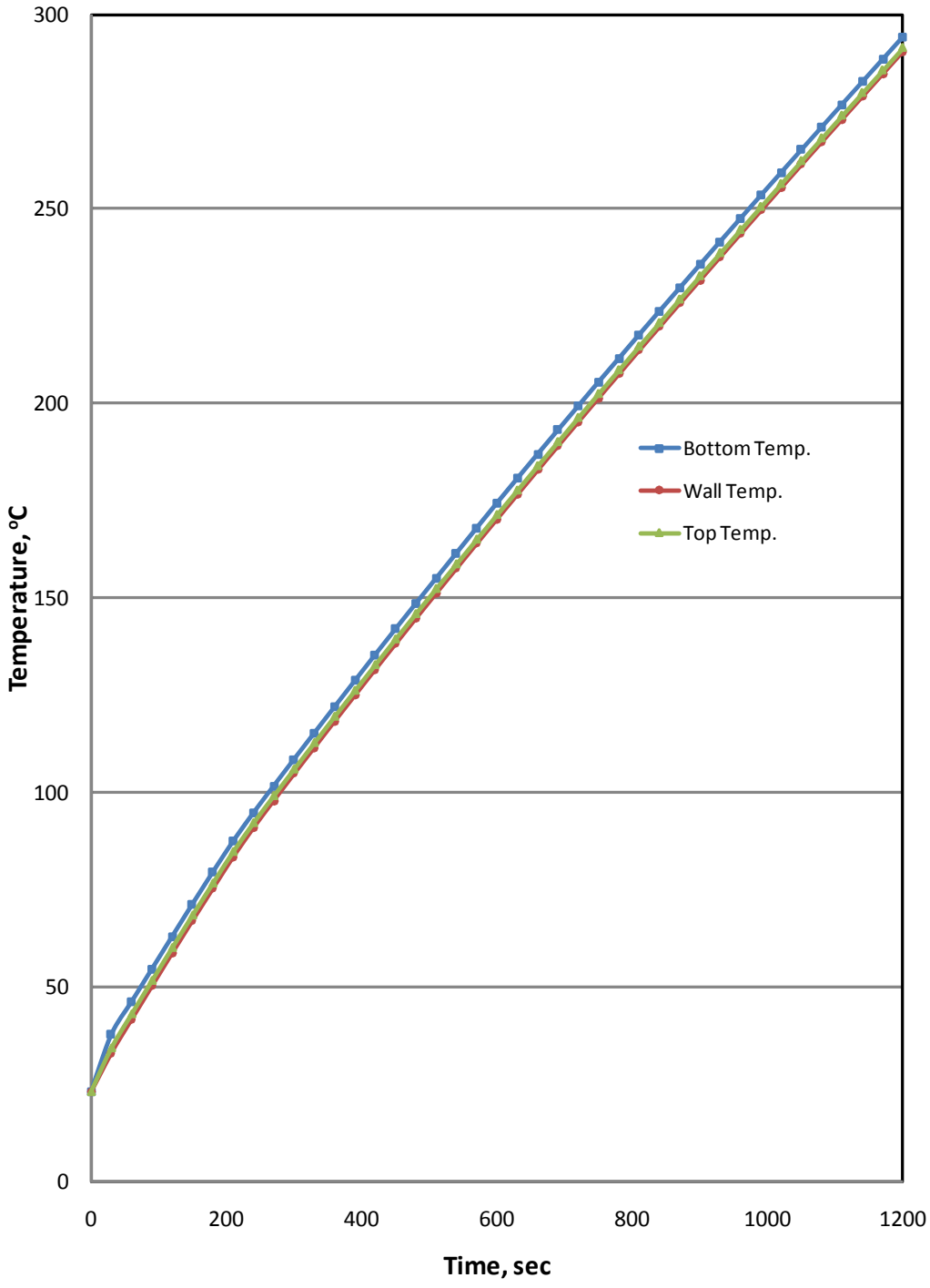

Fig. 3.4—Bottom temperature of n-C_{16} increases with time and reaches to the boiling point of n-C_{16}. Temperature profiles of wall and top also have same profiles as the bottom.

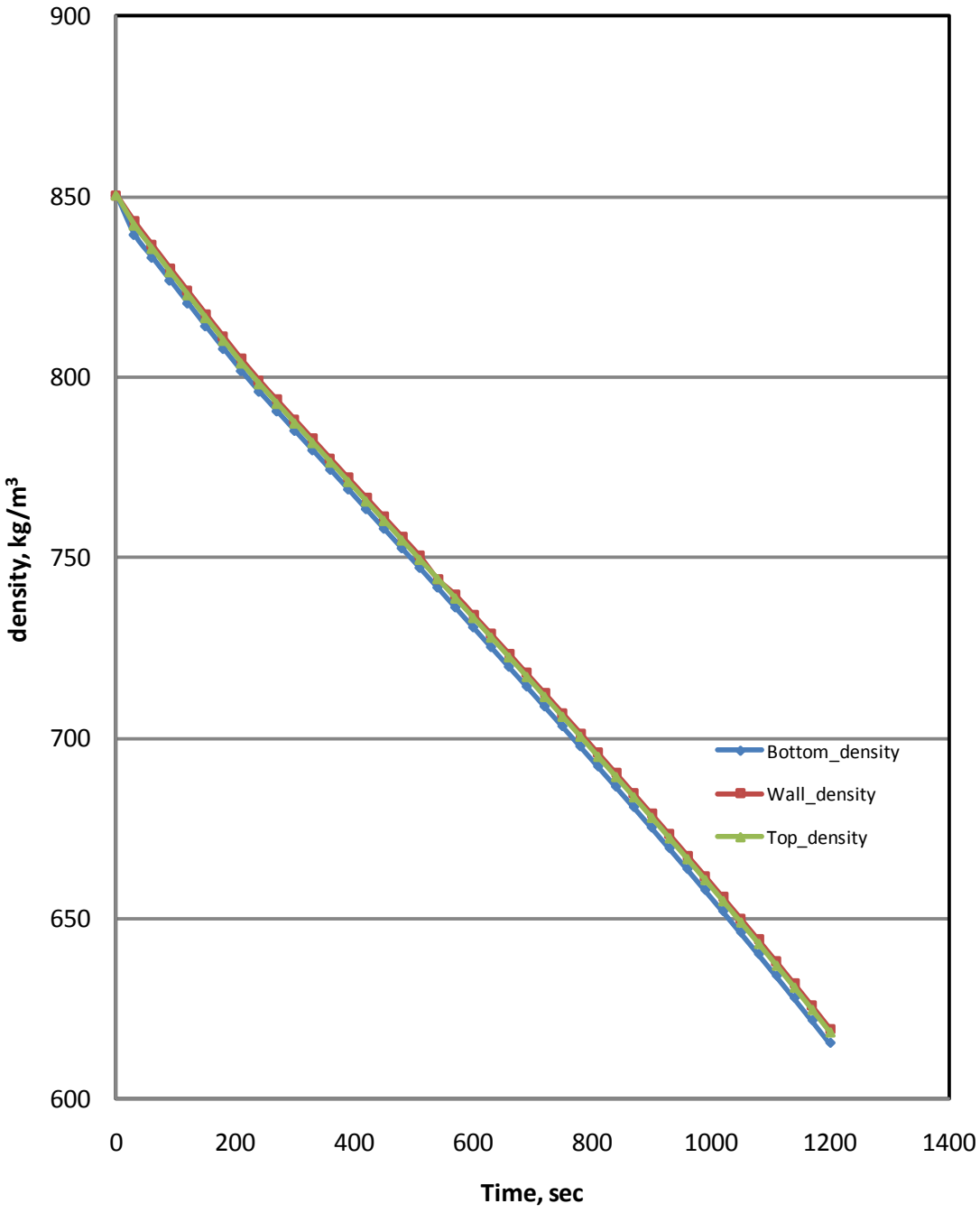

Fig. 3.5—Density profile of n-C_{16} at the bottom decreases with time. Density of wall and top are almost same as the bottom.

Fig. 3.6 shows the velocity vectors and streamlines of the liquid phase n-C_{16} caused by the buoyancy effect. **Fig. 3.6** indicates a case where fluid convection is driven by a pressure gradient and buoyancy forces (**ANSYS Manual**). The buoyancy is driven by variations of density which have a number of causes. In the case of single phase and single component heat transfer, the main cause is local temperature variations. For our simulation, the buoyancy force is

$$F_\alpha = (\rho_\alpha - \rho_{ref})g \,, \quad (3.14)$$

Since we added heat at the bottom, the resulting thermal expansion lowered the density of the n-C_{16}. The lighter n-C_{16} liquid then rose due to the enhanced buoyancy and mixed with other fluids of lower temperature. Therefore, **Fig. 3.6** illustrates the movement of the n-C_{16} liquid during the convection that occurred during our experiment.

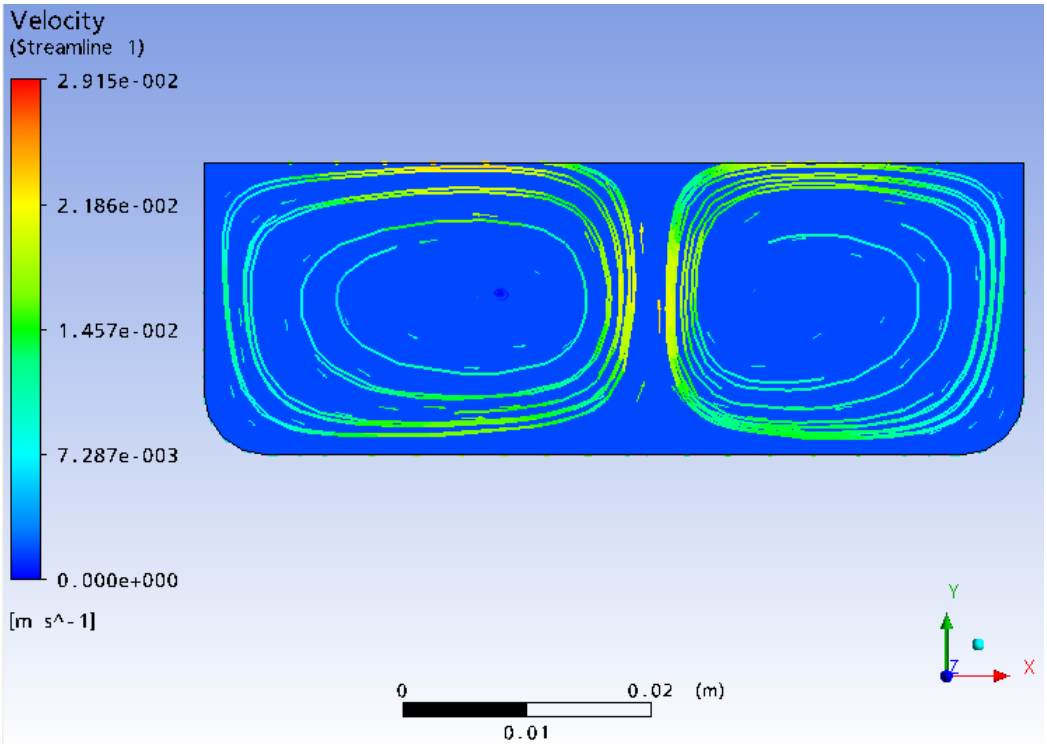

Fig. 3.6—velocity vectors and streamlines of liquid phase n-C_{16}.

Fig. 3.7 indicates the heat flux profiles of the wall and at the top of the n-C_{16} control volume. The heat flux of the bottom had already been determined from the previous calculation. For the bottom heat flux, we computed a constant heat flux of 14000 W/m^2. As for the mid-point heat flux, we took into account the several insulation materials and computed the overall heat transfer coefficient. Regarding the top area of the control volume, we considered the heat loss from the natural convection of the air. **Fig. 3.7** shows that the wall heat flux at mid point is higher than the heat flux at the top. This means we reduced heat loss at the wall using insulation.

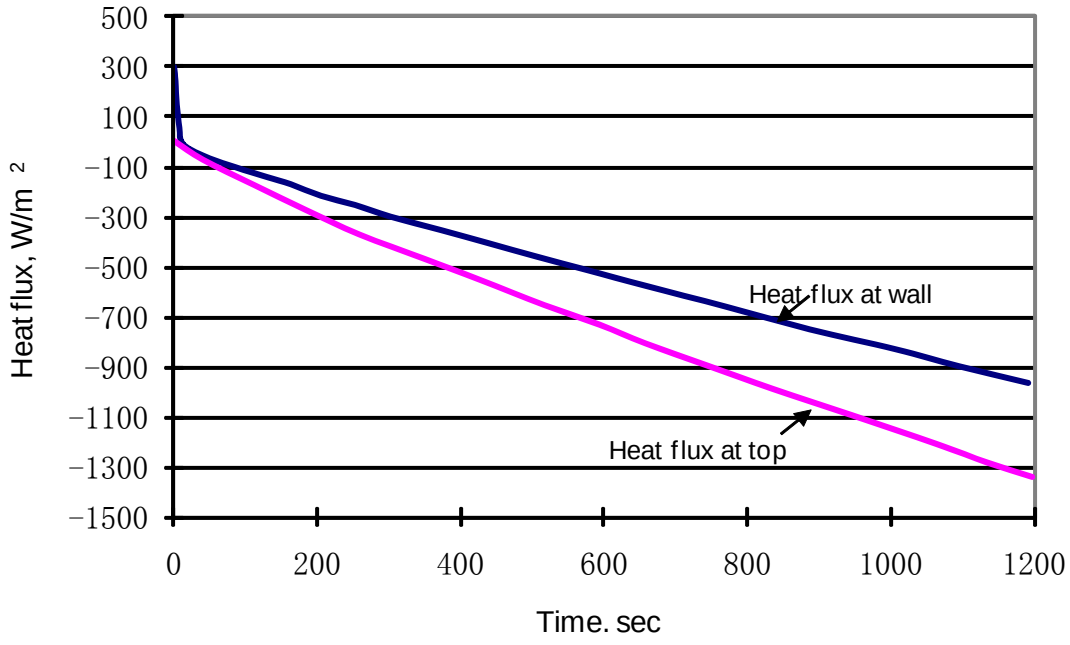

Fig. 3.7—Heat flux profile at the middle and the top of n-C_{16} decreases with time. By using the insulation, heat loss was reduced at the wall.

3.1.2 Multiphase Heat Transfer

Table 3.3 and **Fig. 3.8** show the simulation conditions and control volume of the multiphase heat transfer. Since the bottom temperature of this condition is constant (500^{o}C) we set this condition as steady state. Boundary condition of the wall is as same as the single phase heat transfer. In the case of the bottom boundary condition, we set a constant bottom temperature of 500^{o}C. Since the n-C_{16} liquid and vapor coexist, the initial condition for this simulation was n-C_{16} liquid and vapor at the boiling point of n-C_{16}.

Table 3.3—Simulation condition of multi-phase heat transfer.

Simulation Time	Steady State
B.C. of Wall	Insulated with fiber glass and pyrex glasss
B.C. of Bottom	Constant temperatuer, 500^{o}C
B.C. of Top	Heat loss from condenser, 23^{o}C
Initial Condition	287^{o}C of liquid and vapor phase n-C_{16}

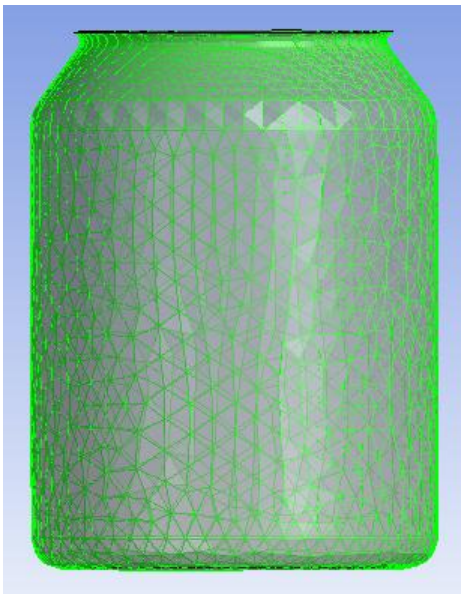

Fig. 3.8—Control volume of multi-phase heat transfer.

Boundary Condition at the Top

During the reflux experiment, vaporized n-C_{16} condenses after reaching the condenser. We added water of 23^{o}C to the condenser using a water pump. The condenser, thus maintains a constant temperature during the experiment. The condensed n-C_{16} vapor makes liquid drops. When the size of the droplets reaches a certain size, the droplets fall to the bottom of the reactor and vaporize again. Therefore, condensation and vaporization occur continuously during the experiment. For the simulation we set a fixed top temperature of 23^{o}C.

Initial Condition

The initial condition of the fluid was 287^{o}C with a mixture of liquid and vapor. The volume fraction of the liquid phase and vapor phase n-C_{16} is 35% and 65%, respectively. The volume of liquid n-C_{16} increased compared to the initial volume of the single phase heat transfer due to the thermal expansion of the liquid phase n-C_{16}.

Fluid Details and Models

Table 3.4 shows the fluid details of n-C_{16} vapor and liquid. Since we conducted a multiphase heat transfer simulation, we needed fluid information for both vapor and liquid. In addition, we used several parameters and models to simulate the transport phenomena of multiphase fluid (**Table 3.5**).

Table 3.4—Fluid details of n-C_{16} vapor and liquid. 0.1 mm of vapor particle diameter is a typical size for diesel fuel injection (Wai K. Cheng 2008). N-C_{16} (cetane) is the main component of diesel fuel.

n-C_{16} Vapor	**n-C_{16} Liquid**
Dispersed Fluid	Continuous Fluid
Mean Diamter: 0.1 mm	Fluid Buoyancy Model: density difference
Fluid Buoyancy Model: density difference	

Table 3.5—Necessary parameter and models for simulation. Surface tension coefficient of n-C_{16} was obtained from Enginnering Software Database Service.

Surface Tension Coeff.	0.0275 N/m
Interphase Transfer	Particle Model
Momentum Transfer	Drag Force: Grace
Heat Transfer	Two Resistance Fluid 1 heat transfer: Zero Resistance Fluid 2 heat transfer: Ranz Marshall Model
Mass Transfer	Thermal Phase Change Model

The following are discussions of four commonly-used models.

1) Interphase Transfer

Each fluid possesses its own flow field and the fluids interact via interphase transfer terms. In the heterogeneous multiphase model, there is one solution field for each separate phase. Transported quantities interact via interphase transfer terms. For example, two phases may have separate velocity and temperature fields, but there will be a tendency for these to come to equilibrium through interphase drag and heat transfer terms (**ANSYS Manual**). We used the particle model for interphase transfer because this model is available when one of the phases is continuous fluid (liquid) and the other is dispersed fluid (vapor).

2) Momentum Transfer

For momentum transfer, we needed to compute the drag force since this option applies to all morphology pair combinations. We tried several drag force models and found that the Grace model provided more realistic simulation results in terms of density distribution and fluid velocity vector profiles than the other drag force models. ANSYS CFX automatically takes into account spherical particle and spherical cap limits and dense fluid particle effects (**ANSYS Manual**).

3) Heat Transfer

We used a two-resistance model to calculate the fluid specific heat transfer coefficient since this model applies to both the particle and mixture models. Since it is possible on one side of the phase interface to specify a zero resistance condition which is equivalent to an infinite specific heat transfer coefficient, we set zero resistance for fluid1. For fluid2, we set Ranz-Marshall, which is the most well tested correlation. The Ranz-Marshall correlation (**ANSYS CFX Manual**) is

$$Nu = 2 + 0.6\,\mathrm{Re}^{0.5}\,\mathrm{Pr}^{0.3} \quad \text{..... (3.15)}$$

where the range of Reynolds number and Prandtl number are,

$$0 \le \mathrm{Re} < 200\,,\ 0 \le \mathrm{Pr} < 250 \quad \text{..... (3.16)}$$

Since our simulation is a multiphase simulation, the temperature of the liquid phase n-C_{16} stays at 287^{o}C with a corresponding Prandtl number of 72. We assumed that the Reynolds number of the fluid is less than 200 since the fluid velocity is very low. The only force acting on the fluid movement is buoyancy.

4) Mass Transfer

We used a thermal phase change model since it describes the change induced by interphase heat transfer. This can be used to simulate evaporation and condensation, or melting and solidification.

Simulation Results

N-C_{16} multiphase consists of both liquid phase and vapor phase n-C_{16}. Since this is a reflux simulation, the temperature of the n-C_{16} will not exceed its boiling point of 287^{o}C. This is because when the vaporized n-C_{16} reaches the condenser, the condenser removes heat from the vaporized n-C_{16}. Therefore, cracking of n-C_{16} is less likely take place during the n-C_{16} reflux. **Fig. 3.9** shows the temperature distribution of the n-C_{16} multiphase heat transfer simulation. Mostly, the temperature of the vapor and liquid stays at the boiling point of n-C_{16}. The top of the reactor has a low temperature distribution because of condensation. The bottom part has a high temperature profile

since we fixed it at 500°C. From the temperature profile of the bottom, we can estimate that a minor amount of n-C_{16} thermal cracking might be possible during the reflux mode. We found from our laboratory analysis of n-C_{16} reflux that a little thermal cracking took place during that experiment which resulted in the creation of some lighter components.

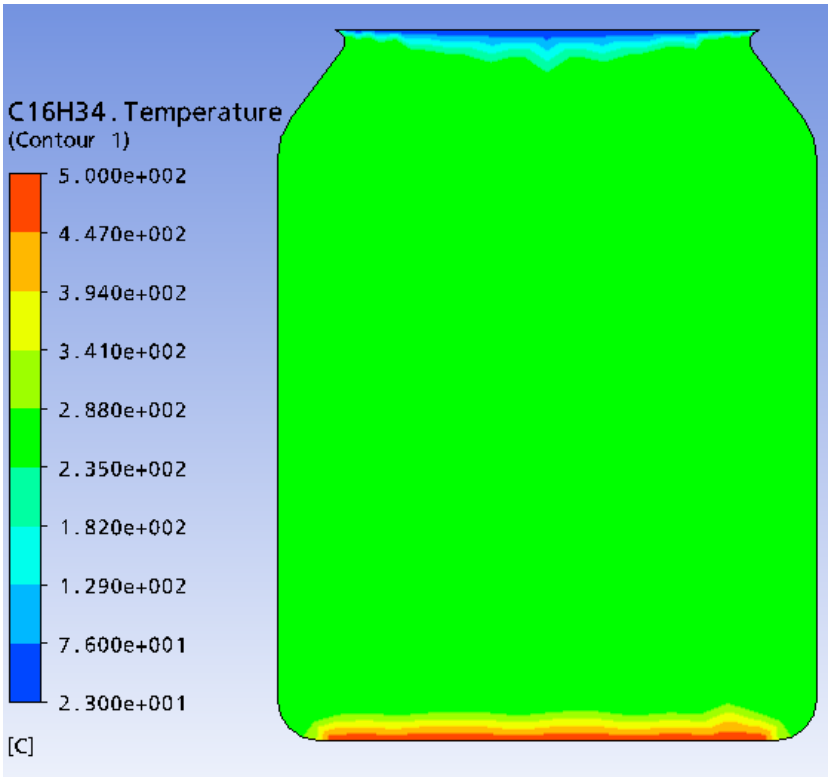

Fig. 3.9— Temperature distribution of n-C_{16} multiphase simulation indicates that vapor and liquid phase of n-C_{16} stay at almost same temperature (287 °C).

Fig. 3.10 indicates the density distribution of the n-C_{16} multiphase simulation. All the liquid and vapor n-C_{16} are stratified by their density. These results were fed to the Monte Carlo N-Particle (MCNP) code to simulate radiation entering an area the density of which is not uniform. Therefore, we were able to estimate a more realistic radiation dose in the fluid.

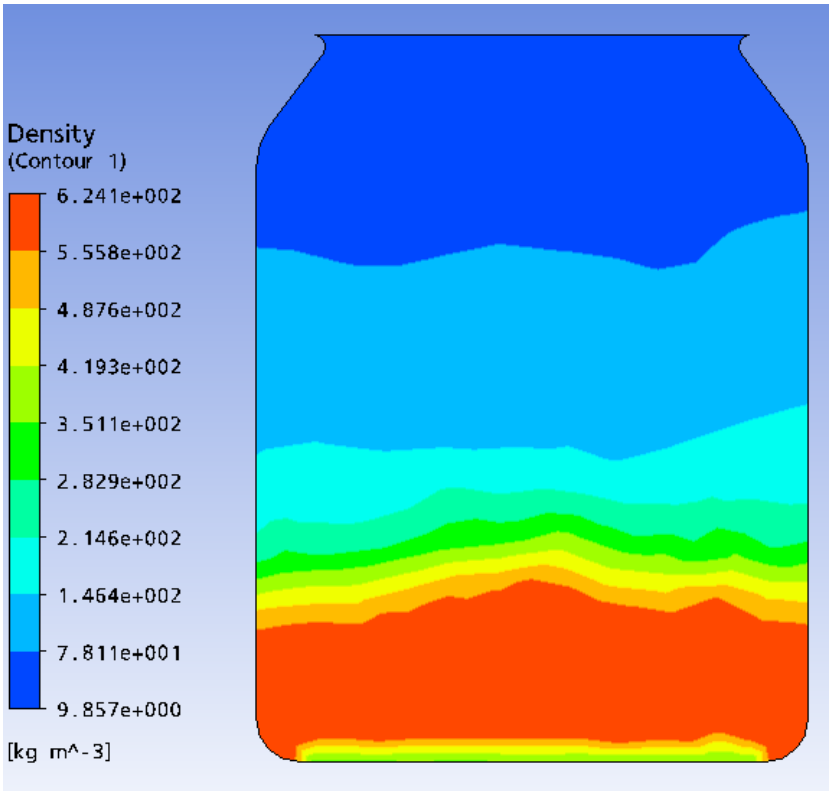

Fig. 3.10—Density distribution of liquid and vapor phase n-C_{16} shows that multiphase n-C_{16} is layered by its density. Upper part of n-C_{16} mostly consists of vapor phase n-C_{16} and bottom part is liquid phase n-C_{16}.

Fig. 3.11 and **Fig. 3.12** show the velocity vector of n-C_{16} vapor and liquid which describe the movement of the vapor and liquid phase n-C_{16}. From the result, we estimated how fast the vapor and liquid phases move during the experiment and the possible direction of the fluid when they move. We can then use this information to estimate the radiation dose more reliably. By comparing **Fig. 3.12** and **Fig. 3.13,** we found that the velocity of the vapor is about three times that of the liquid.

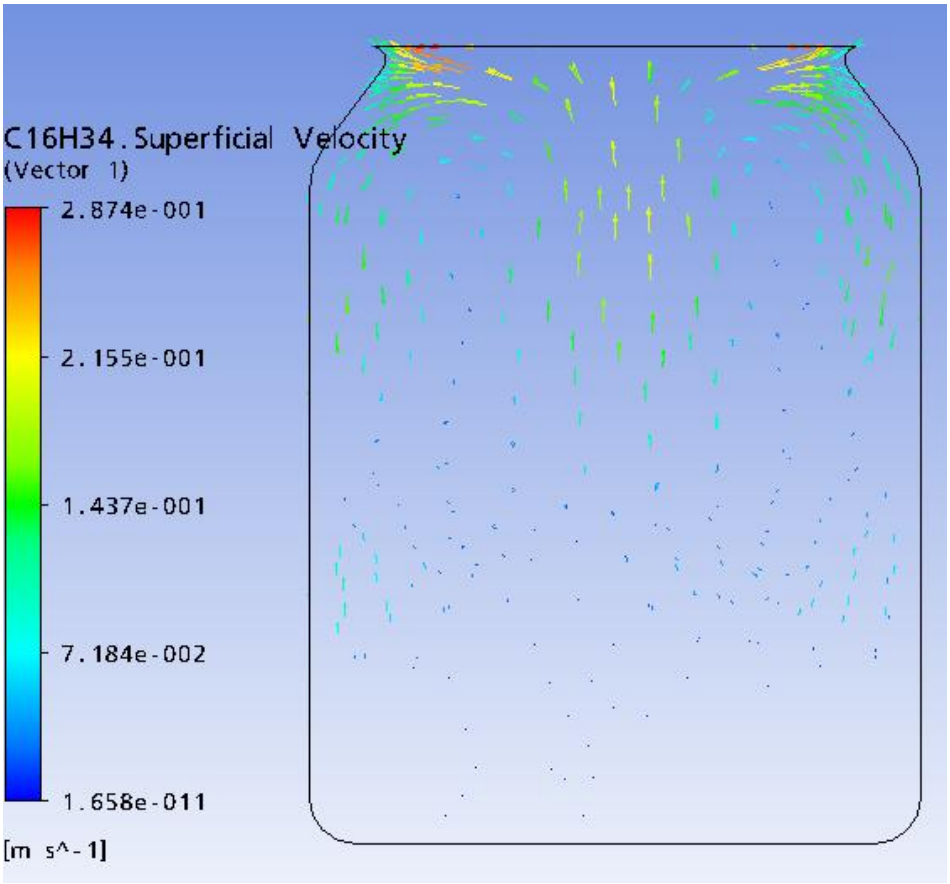

Fig. 3.11— Velocity vectors of n-C_{16} vapor. Compare to the velocity of n-C_{16}, velocity of vapor is approximately three times faster than liquid.

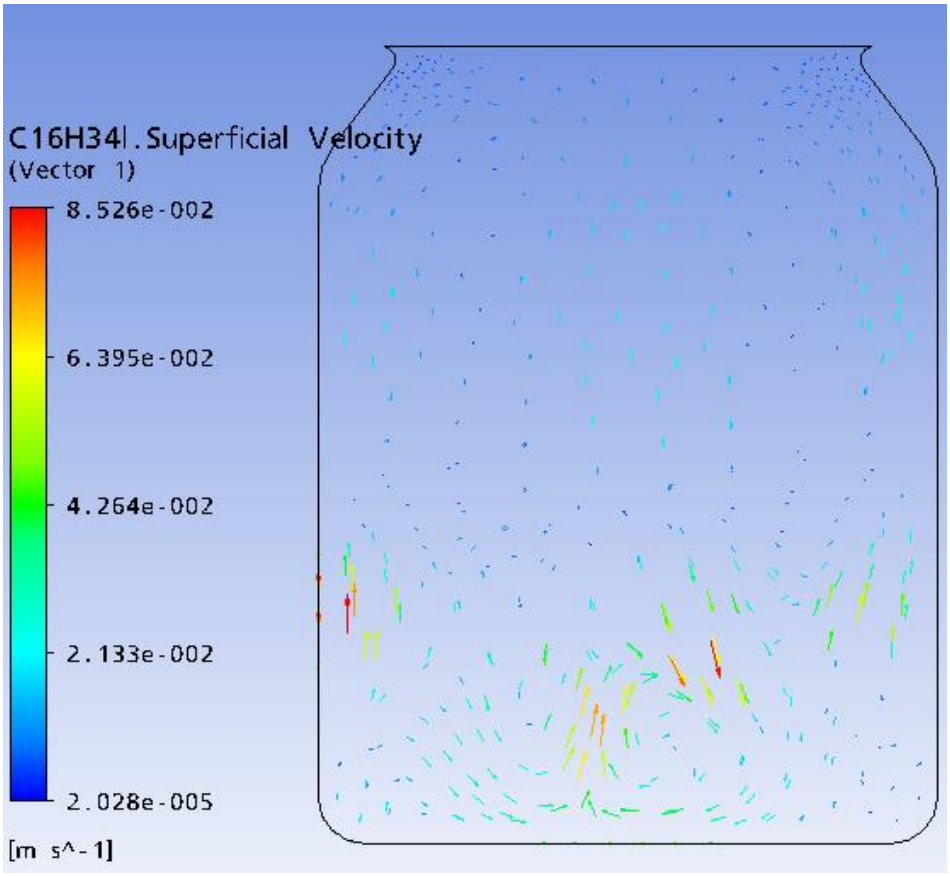

Fig. 3.12— Velocity vectors of n-C_{16} liquid.

Fig. 3.13 shows heat flux in the control volume of n-C_{16}. Even though the system receives thermal energy from the heater it also loses its energy through heat loss to the outside air.

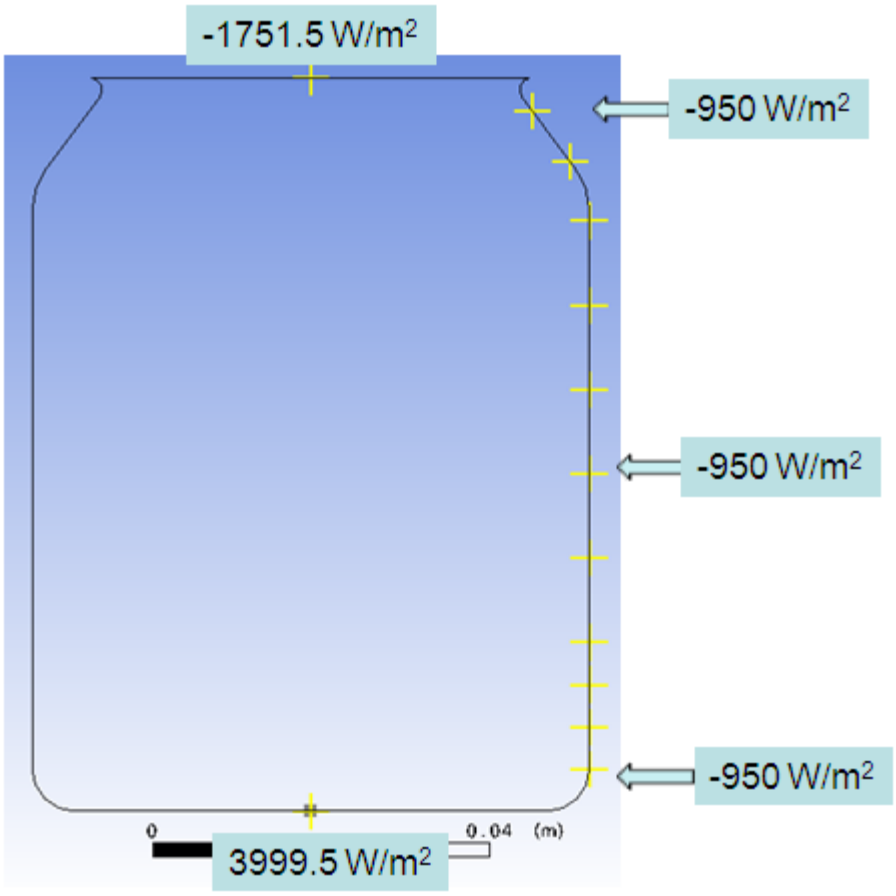

Fig. 3.13—Heat flux distribution in the control volume. Negative convention indicates heat loss. Positive convention means heat flux from the heater. Largest heat loss occurs on the top of the control volume.

3.1.3 Validation of Simulation

Validation examines if the conceptual models, computational models as implemented into the CFD code, and computational simulation agree with real world observations (NASA 2008). The strategy is to identify and quantify error and uncertainty through comparison of simulation results with experimental data.

Experimental data is the observation of the “real world” in some controlled manner. By comparing the CFD results to experimental data, one hopes that there is a good agreement, which increases confidence that the physical models and the code represent the "real world" for this class of simulations. However, the experimental data contains some level of error. This is usually related to the complexity of the experiment (NASA 2008).

In our n-C_{16} reflux simulation, we matched the time to reach the boiling point of n-C_{16} to the experiment. Also, we found from our multi-phase simulation that the temperature distribution of the control volume stays at almost same temperature (287^{o}C). During the n-C_{16} reflux, since vaporization and condensation taken place simultaneously it wouldn’t be happened that the temperature of the n-C_{16} increase beyond its boiling point (287^{o}C) without the increase in pressure.

Measuring the temperature outside of glass wall and the top of the reactor using thermocouples is a good way of comparing the experimental data to the simulation data. To locate several thermocouples in the reactor, it will require some modification of the reactor design.

For validating simulation of fluid with multi-components, we may need to measure the vapor temperature profile of the reflux experiment. However, vapor temperature measurement wouldn’t be unstable because of the turbulence occurred during the reflux phenomena.

3.2 Radiation Transport Monte-Carlo Simulation

In this study, Kim (2009) used the Monte Carlo N-Particle, Version 5 (MCNP-5) developed at the Los Alamos National Laboratory (Brown 2003). This code is capable of simulating coupled electron-photon problems using a three dimensional combinatory geometry system.

Using the code, Kim simulated irradiation of n-C_{16} in the aluminum can reactor with the Van de Graff E-Beam accelerator. The simulated E-Beam source is a parallel plane large enough to cover the target. The electrons were emitted in a plane and

distributed evenly within the scan angle. The target was positioned 30 cm in front of the exit beam window, and the density of n-C_{16} was taken from the heat transfer simulation (Yang 2009). **Fig. 3.14** shows the input geometry for the single phase simulation. According to the result of heat transfer simulation, the height of n-C_{16} is 2.35 cm at a volume of 80 ml. In the multiphase simulation, n-C_{16} is distributed throughout the entire aluminum can.

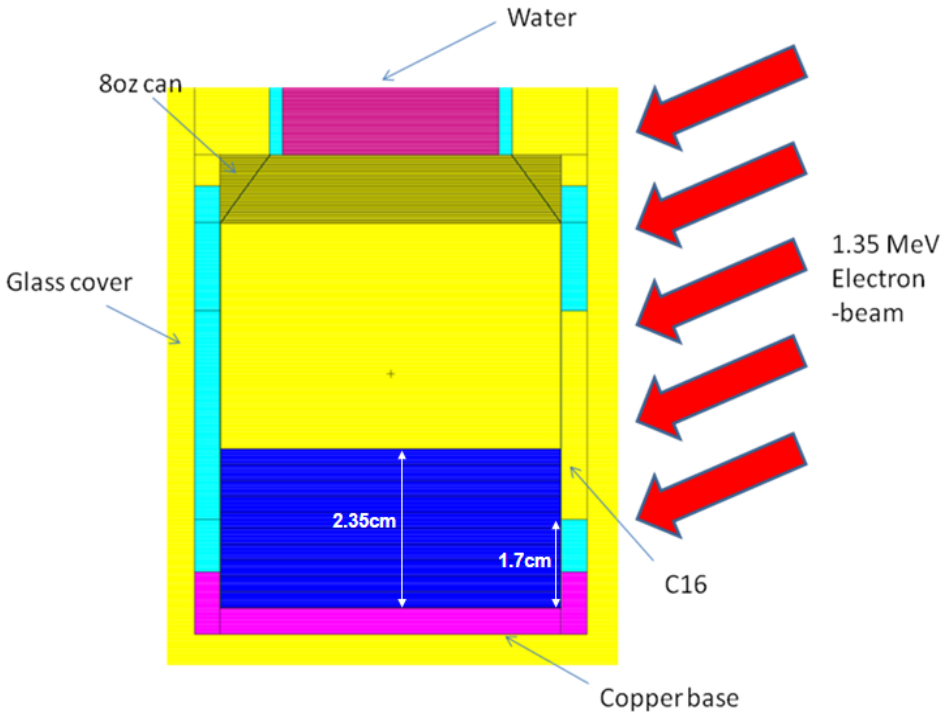

Fig. 3.14— Input geometry for n-C_{16} Monte Carlo simulation. Electron beam (1.35 MeV) was tilted 22.5 degree from the horizontal line. E-Beam entrance window starts from 1.7 cm above the bottom.

Generally, Monte Carlo simulation results represent an average of the contribution from many histories sampled during the course of the problem. Therefore, a total of 10^6-10^7 histories were used in our simulation to reduce the statistical uncertainty to about 5% or less. The total sampled histories were generated from the probability of electron path in the n-C_{16}. **Fig. 3.15** shows the paths of an electron in n-C_{16} as a probabilistic example. **Fig. 3.16** shows the real paths of electrons through irradiated solid media.

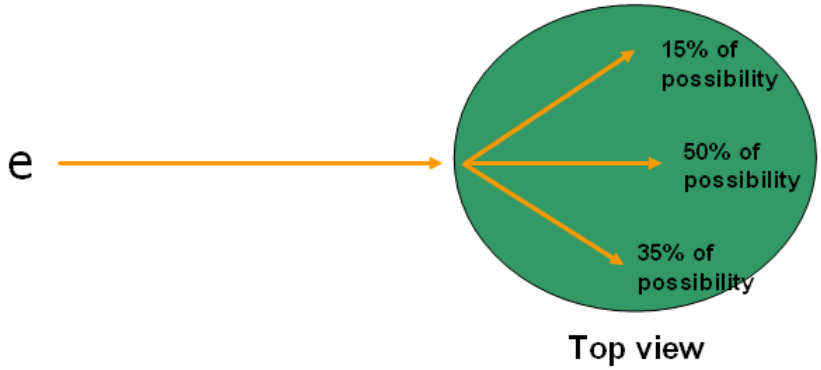

Fig. 3.15— Path of an electron in n-C_{16} sample (probabilistic example).

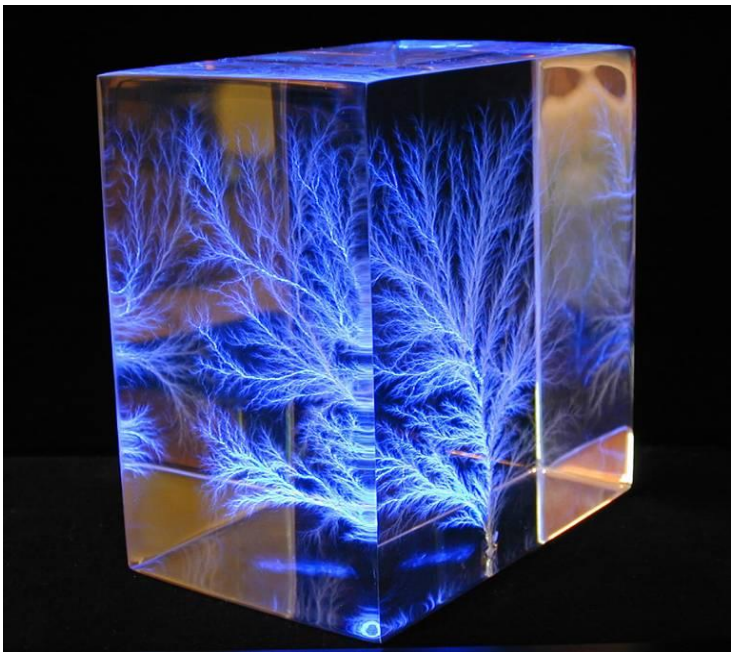

Fig. 3.16— Electron paths of irradiated sample (source: Stoneridge Engineering).

Single phase simulation result

As mentioned earlier, since the volume of n-C_{16} increased due to thermal expansion, the height of the n-C_{16} liquid in the reactor increased with the heating time (**Fig. 3.17**). All four curves show the same tendency; doses measured from the interface surface to 0.5 cm below the surface have the main portion of the absorbed dose, and then

they decrease significantly until they reach zero. This means the main radiation interaction occurs between the surface of the n-C_{16} and 0.5 cm below the surface.

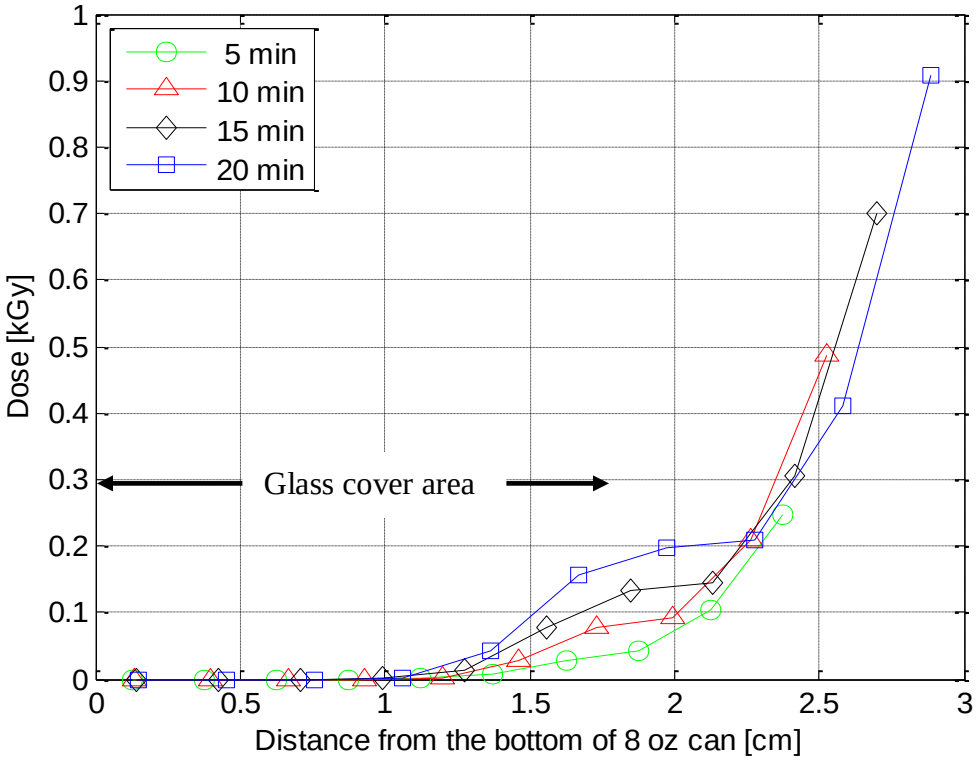

Fig. 3.17—Dose in n-C_{16} at single phase for 1.35 MeV electron beams of heating times.

Fig. 3.18 shows the dose distribution of the n-C_{16} at the surface after 10 minutes of heating and irradiation. Almost one fourth of the area has doses of more than 0.7 kGy, because that portion of the area is only directly exposed to the entering electrons. The remaining area receives some dose due to electron scattering, though the dose is quite low.

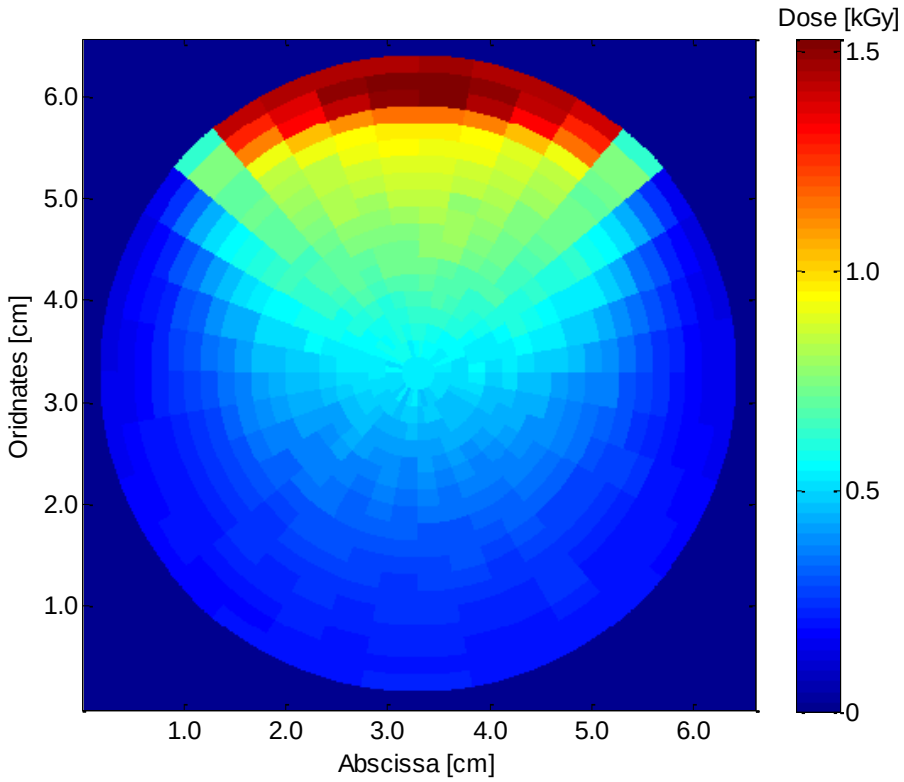

Fig. 3.18—Dose of n-C_{16} at 10 minutes of heating time (surface layer: 2.35 cm above the bottom). Highest radiation dose occurs at the electron shooting zone (red area).

Fig. 3.19 shows the radial doses (0^o, 90^o, 180^o, and 270^o) from the center of **Fig. 3.18**. At 90^o, Kim found regions of short build-up, fast-falling dose, and slow linear decreasing dose. Doses at 0^o and 180^o are almost the same as each other. However, the slope up to 1.56 cm is lower than the one between 1.56 cm and 3.12 cm because the former area is open to entering electrons and the latter one is the area covered by the glass cover. In addition, the doses at 0^o and 180^o are higher than the ones at 270^o, where electrons were partially blocked by the upper glass cover.

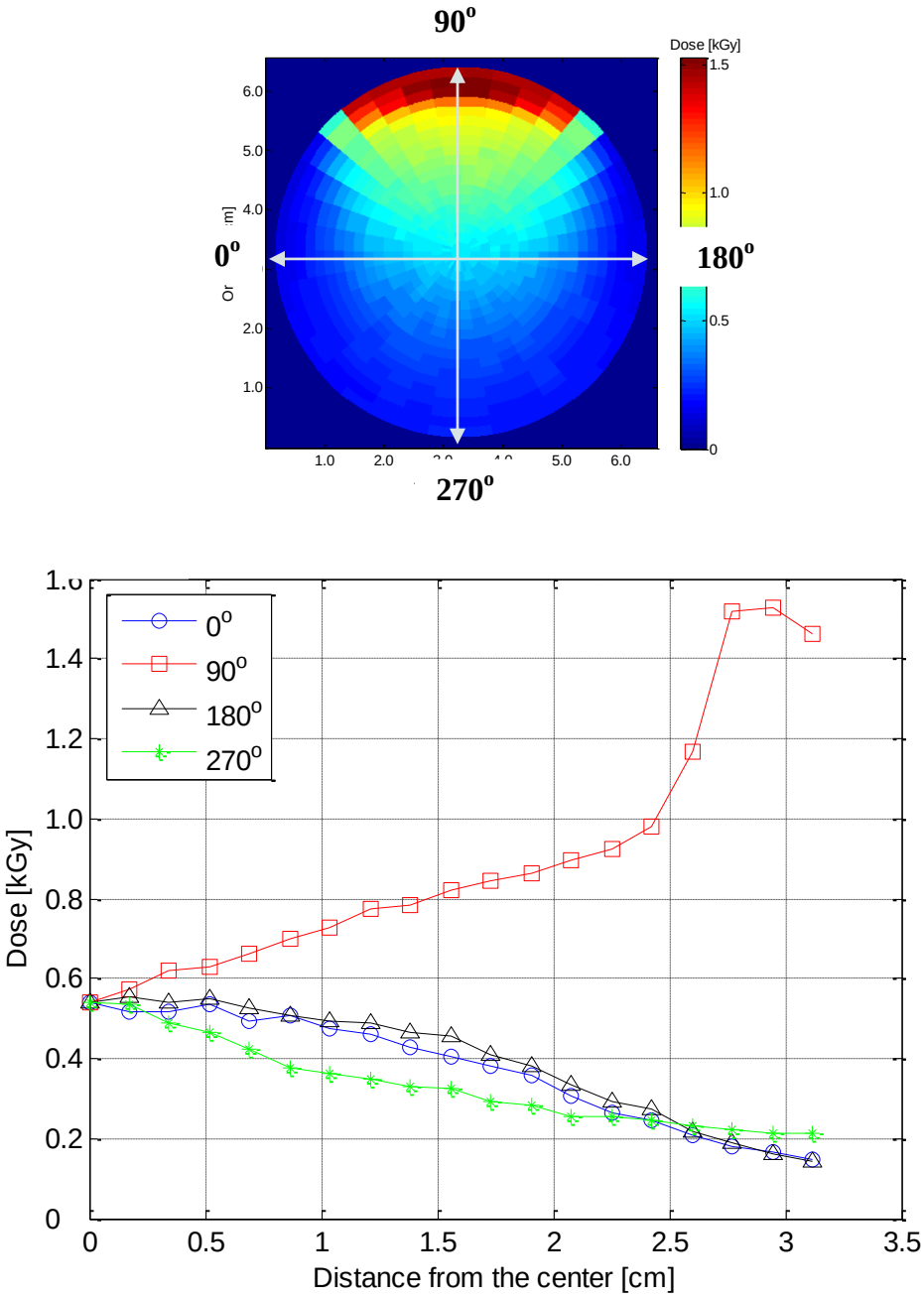

Fig. 3.19—Radial doses from the center at the surface.

In the middle layer, just under the lower glass cover window, the doses only exist within 0.69 cm from the outside of the circle (**Fig. 3.20**), which results mainly from the scattering of electrons. There is no dose in the rest of the area.

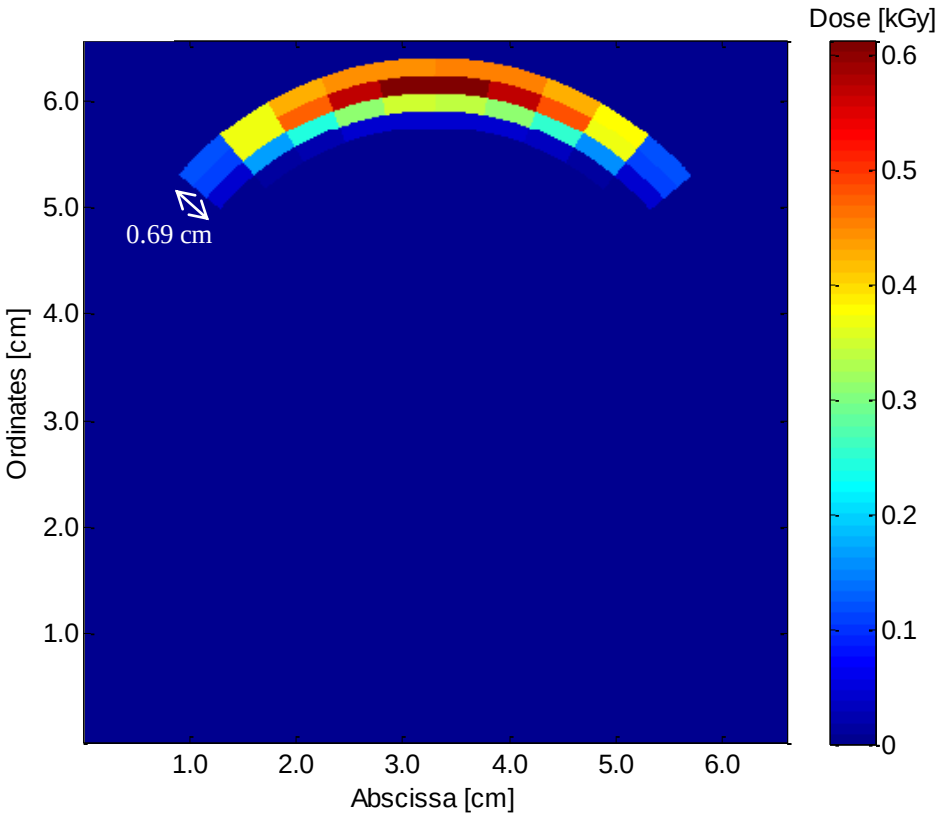

Fig. 3.20—Dose of n-C_{16} at 10 minutes of heating time (middle layer).

Multiphase simulation result

Fig. 3.21 shows the average densities from the heat transfer simulation and their corresponding doses from the Monte Carlo simulation at the same position. The maximum dose is 2.08 kGy at 3.95 cm from the bottom, where the fluid density is low (0.16 g/cm^3) and the region is fully exposed to the E-Beam. The glass cover decreased the kinetic energy of the electrons dramatically; slopes of the dose curve at 1.7 cm and 5.7 cm, the lower and upper limit of the glass cover window, are significantly large.

The dose below 1.7 cm gradually decreases to zero as it approaches to 0.7 cm. Even though the glass cover absorbed most of the electrons' kinetic energy, some electrons still reached 1.0 cm below the lower window. Below that, there is no radiation dose because the high-density copper base (8.94 g/cm^3) prevented electrons from reaching the n-C_{16} inside the aluminum can.

Between 5.7 cm and 7.0 cm, the dose also decreases gradually. Its slope, however, is not as steep as the one mentioned above because electrons more easily penetrate the low density region of the n-C_{16} and also scatter easily. Above 7.0 cm, the dose increases again with the help of electrons entering the shoulder region of the can, and continues to increase as it approaches the aluminum can's maximum height of 8.4 cm. The radiation in this setup has a greater effect on the low density region than the high density region.

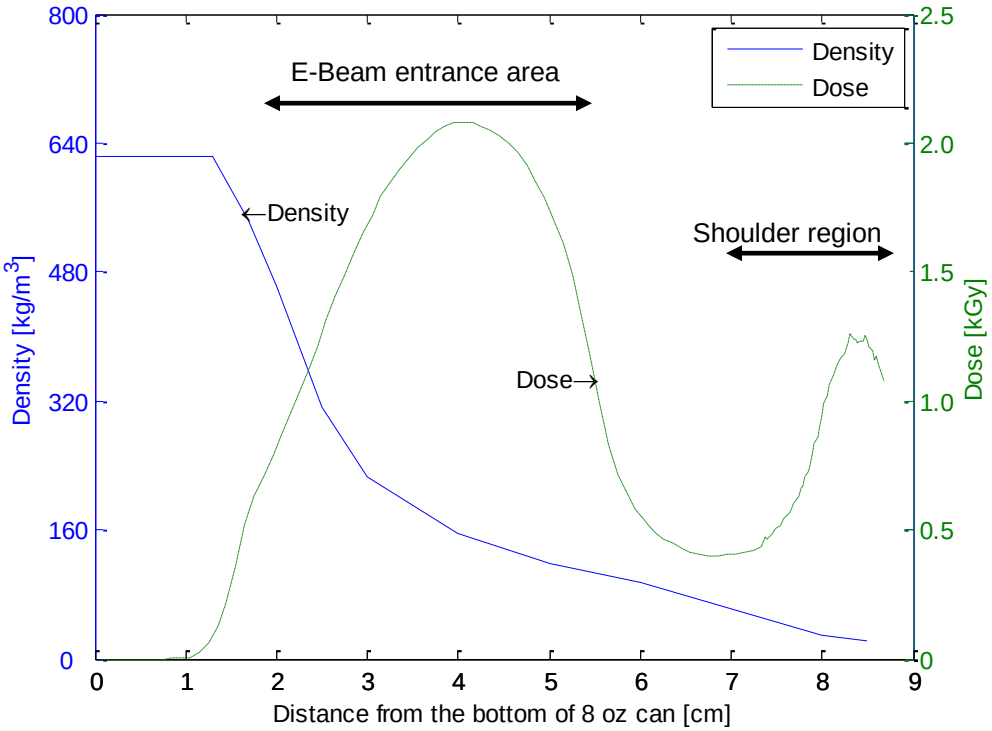

Fig. 3.21—Density and dose vs. vertical distance from the bottom of 8 oz aluminum can. This dose distribution is at 1 hr of irradiation time, when the total average dose is 0.67 kGy.

Fig. 3.22 shows the density distribution obtained from the heat transfer simulation and the corresponding dose distribution of the n-C_{16} at 2.0 cm (a), 4.0 cm (b), and 6.0 cm (c) from the bottom of the aluminum can. The highest dose occurred in the middle layer (4.0 cm from the bottom). More detailed discussion of dose distribution in the three layers is followed.

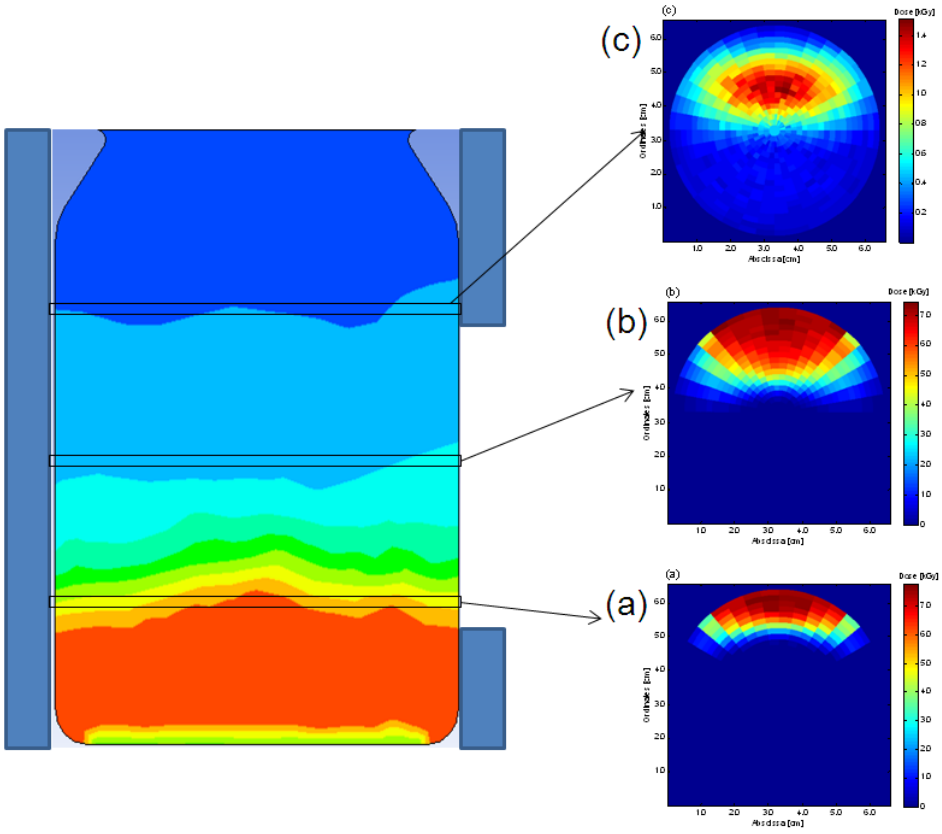

Fig. 3.22—Density distribution from heat transfer simulation and corresponding dose distribution of n-C_{16} at 2.0 cm (a), 4.0 cm (b), and 6.0 cm (c) from the bottom of the aluminum can.

Fig. 3.23 shows dose distribution at 2 cm, just above the lower glass window (1.7 cm). The penetration depth is 1.21 cm, which is quite larger than the penetration depth of electrons in water (0.3 cm), which was exposed to the same electron kinetic energy. This is due to the low density of the n-C_{16} (0.46 g/cm^3) at that region.

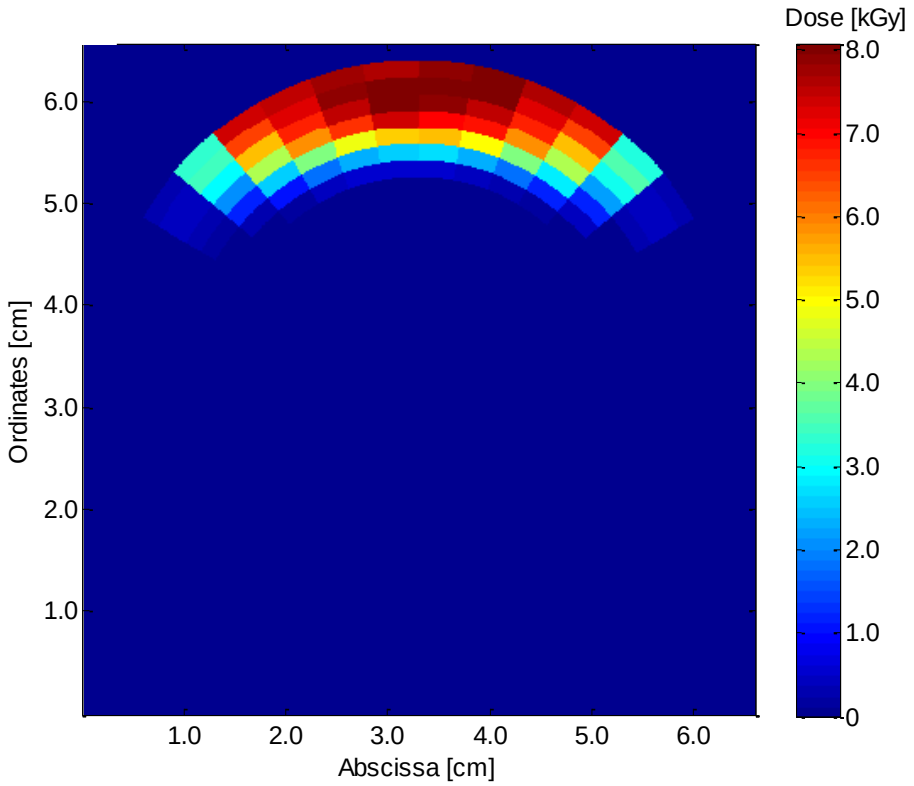

Fig. 3.23—Dose distribution of n-C_{16} at 2.0 cm from the bottom of the aluminum can.

Electrons entering regions of low density (0.16 g/cm^3) penetrate into the n-C_{16} slightly more than halfway (**Fig. 3.24**). However, the rest of the region does not receive any radiation because the upper glass cover blocks electrons which would otherwise reach the region. The area behind the window of the glass cover shows the highest dose.

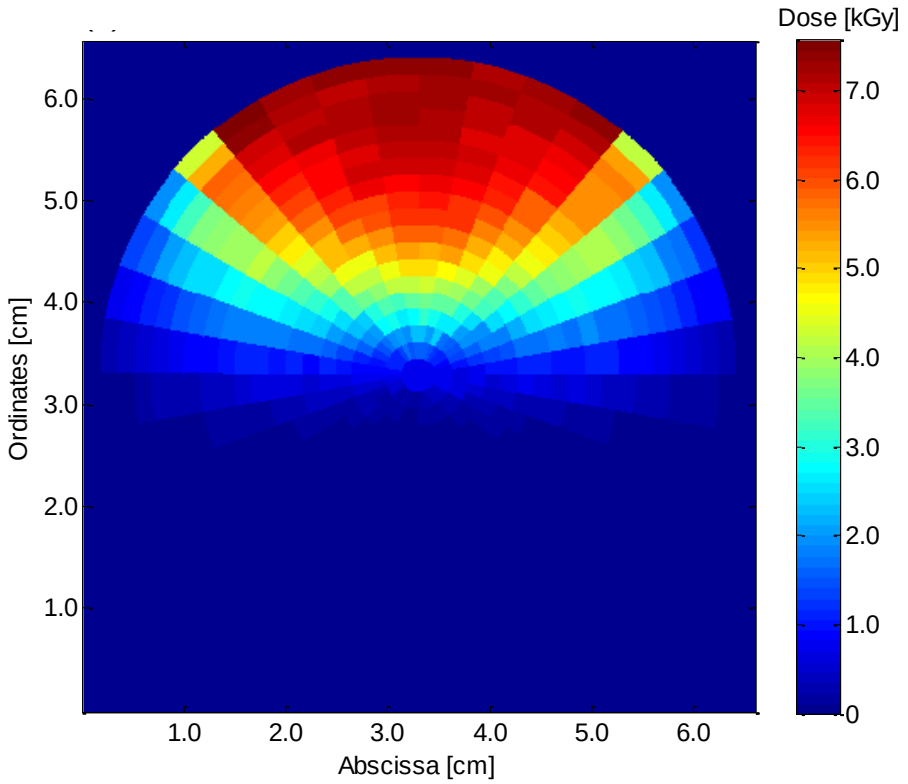

Fig. 3.24—Dose distribution of n-C_{16} at 4.0 cm from the bottom of the aluminum can.

Unlike the above cases, dose is distributed in the entire layer at the distance of 6.0 cm (**Fig. 3.25**). Electrons entering the shoulder region can reach the very back of the aluminum can due to the low density of the n-C_{16}. Using the glass cover resulted in the area with the highest dose shifting inward. This case (at 6 cm from the bottom) has an average dose that is lower than the average of the other two cases.

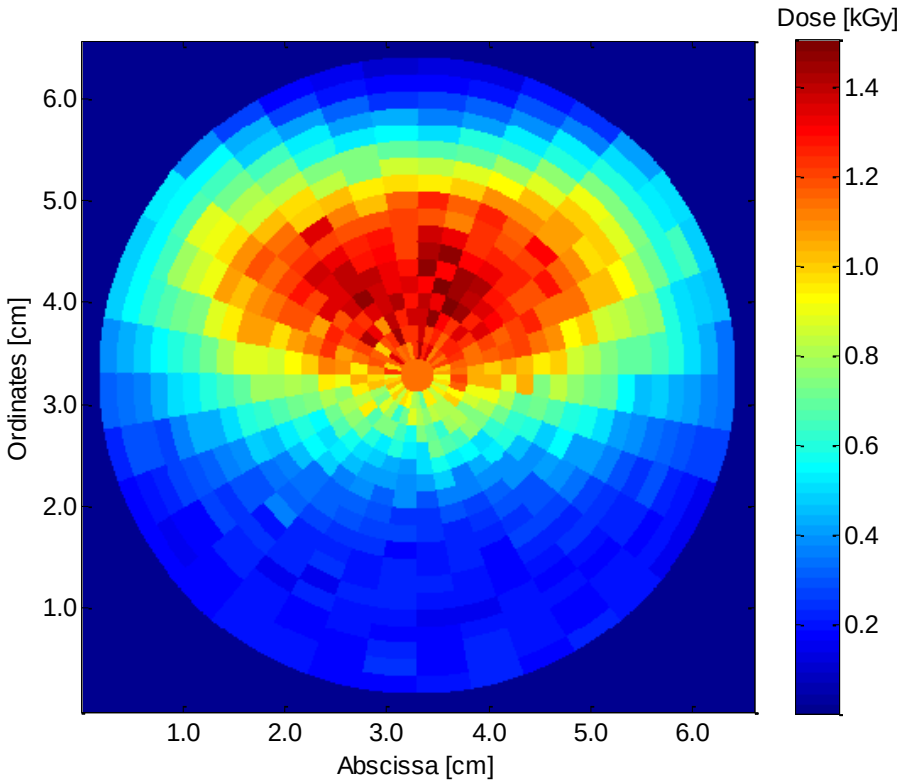

Fig. 3.25—Dose distribution of n-C_{16} at 6.0 cm from the bottom of the aluminum can.

These three dose distributions are good examples of whole dose distribution of n-C_{16}. However, n-C_{16} moving in a fluid state in a Monte Carlo simulation requires a huge amount of computing time to obtain a reliable result, and is almost impossible given currently available super computing power. This problem may be solved by post-processing of non-movement simulation results (e.g. random movement of n-C_{16} within the irradiation area). However, since we know the trend of fluid movement and velocity of fluid from the heat transfer simulation we can estimate the residence time of the fluid with limited penetration depth, which provides better ideas for estimating the average dose more accurately.

CHAPTER IV

POTENTIAL APPLICATION AND ECONOMIC FEASIBILITY

4.1 Potential Applications

4.1.1 E-Beam Partial Upgrading Facility

The high viscosity of heavy oil causes transportation problems. Today, partial upgrading technologies are used to make upgraded synthetic oil after heavy oil production. This is a highly energy-intensive process since it requires breaking large hydrocarbon molecules of heavy oil. The radiation effect on hydrocarbons from the use of E-Beam upgrading technology can minimize thermal energy consumption and the use of expensive catalysts. **Fig. 4.1** shows a conceptual design of an E-Beam field upgrading facility. After the production of heavy oil by a thermal recovery method, we send the heavy oil to the field upgrading facility and provide E-Beam radiation to the oil to break heavy molecules. During this time the heavy oil may have enough thermal energy to initiate free radical chain reactions since it is produced from a thermal recovery process. As a result, the heavy oil is able to initiate C-C bond decomposition with E-Beam. After upgrading the heavy oil, we send the upgraded oil to the distillation facility to obtain a certain range of distillation cut such as a naphtha, light gas oil, and vacuum gas oil. Then we can obtain synthetic crude oil which we can send to a refinery for further processing. This facility is able to promote higher profit from heavy oil production.

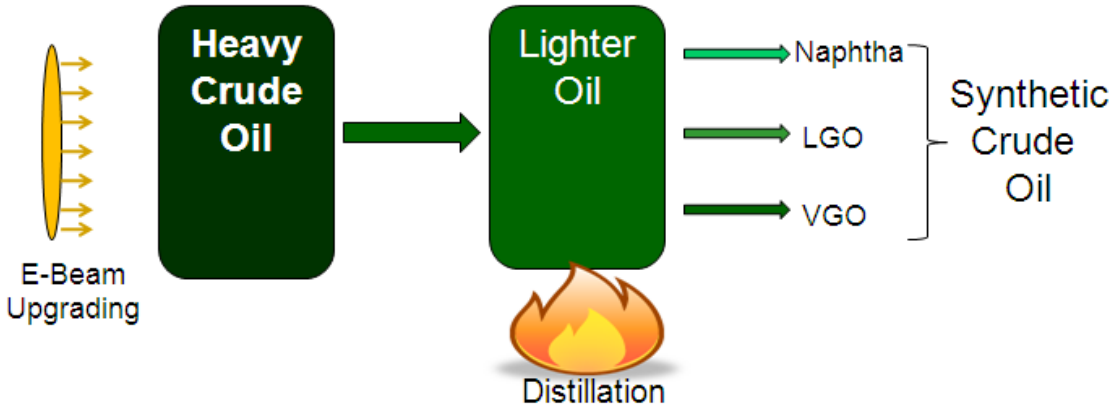

Fig. 4.1—Conceptual design of E-Beam field upgrading facility (batch system). Heavy crude oil is upgraded by E-Beam and upgraded oil sent to distillation facility to make synthetic crude oil. LGO stands for light gas oil and VGO stands for vacuum gas oil.

4.1.2 Pipeline Heavy Oil Upgrading

Fig. 4.2 shows a conceptual design of pipeline heavy oil upgrading (Yang et al. 2009). Two E-Beam machines are located near the heavy oil pipelines, and the machines generate electrons. These electrons enter the heavy oil inside of the pipeline and break hydrocarbon molecules which then generate lighter components. These lighter components make the heavy oil lighter for easy transportation. The number of machines to be used depends on the power of a machine and the kinetic energy of the electrons generated from the machine. To deliver electrons to the heavy oil effectively, we should design a special window for the E-Beam shooting area.

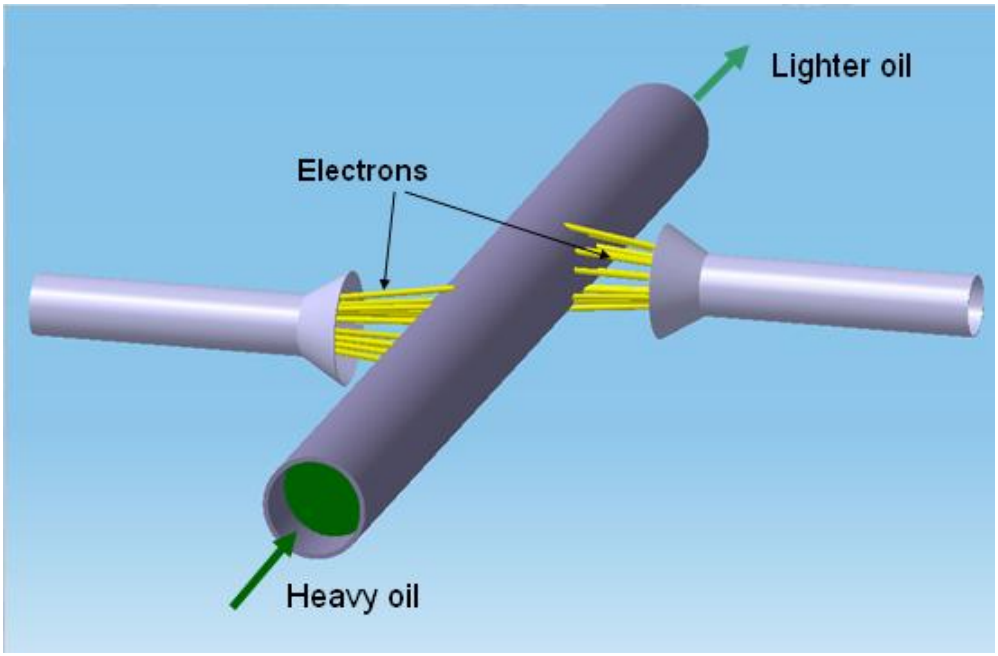

Fig. 4.2 — Electrons with high kinetic energy are generated by two E-Beam machines. These electrons enter heavy oil and break the heavy molecules of the heavy oil.

4.1.3 Refining Industry

In the refining industry, we can use this technology to lower the thermal energy consumption in the distillation column. From the naphtha experiments, we found that E-Beam increases the vapor temperature of naphtha.

In addition, we can reduce the amount of undesirable components and create the most demanded components. Our asphaltene experiment indicated that E-Beam significantly reduces aromatic content. From our experiments with naphtha and n-C_{16} we found that E-Beam creates more olefins when compared with conventional methods. Olefin is a very valuable chemical in the petroleum industry. Especially, ethylene, part of the olefin group, is very expensive, and the ethylene market is huge in petrochemical industry. The asphaltene experiment also indicated that E-Beam enhances isomerization of hydrocarbons. In the petrochemical industry, many isomerization techniques have

been developed because of the industrial importance of isomerization reactions. Therefore, we will be able to create new techniques to generate isomers at lower cost.

4.2 Machine and Operation Cost

Fig. 4.3 shows a currently used industrial-scale E-Beam machine for waste water treatment. This machine is able to process 10,000 bbl of waste water for 24 hours of operation with 3.1 kGy of absorbed dose. Since the machine is very durable, 24 hours of continuous operation is possible. Only 2 to 3 days of maintenance time is required for one year of continuous operation.

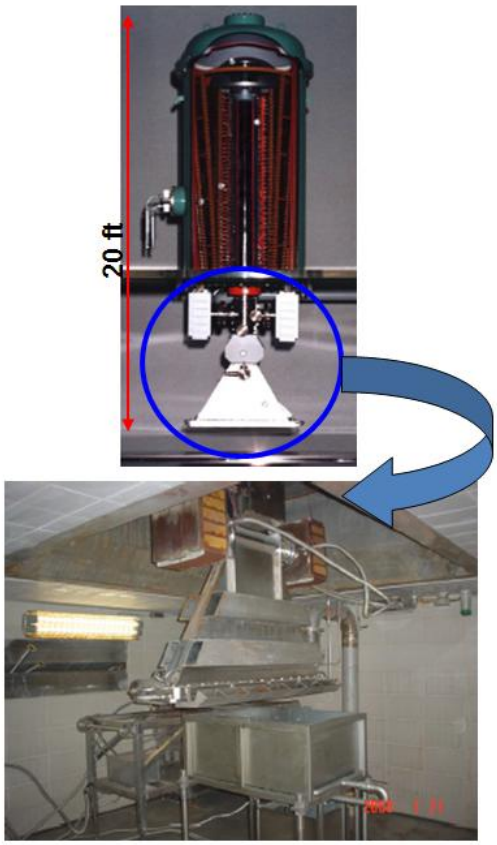

Fig. 4.3—Industrial scale E-Beam machine. It is able to process 10,000 bbl of oil per day with absorbed dose of 3.1 kGy.

.

In addition, the cost of the machine, including installation and shielding, is not very expensive (**Table 4.1**). Assume that we are upgrading heavy oil with the same absorbed dose (3.1 kGy) used for waste water treatment. Then, we can theoretically calculated radiation energy transferred to the fluid per day which can be calculated by

$$E_{tr} = P_{Beam} \times t \,, \quad \text{.....} \quad (4.1)$$

where E_{tr} is radiation energy transferred to the fluid, P_{Beam} is Beam power of the machine, and t is the process time in second. If we consider the efficiency of the process, we are able to obtain process volume to irradiate heavy oil with 3.1 kGy of radiation dose which is 10000 barrel per day. Using the specification of the machine and electricity cost in Texas, we estimated the process cost in cents per bbl. Here, we computed the average electricity cost in Texas to estimate the operation cost for one year of continuous operation. From the calculation, the E-Beam operation cost to upgrade 1 bbl of heavy oil is only 3 cents (**Table 4.2)**.

Table 4.1—Specification of an industrial scale E-Beam machine.

Electron Kinetic Energy, MeV	2.5
Beam Power, kW	100
Beam Current, mA	50
Total Power Consumption, kW	148
Power Efficiency, %	68
Process Volume, bbl/day[a]	10000
Total Cost, Million USD	1.35

a. Absorbed Dose: 3.1 kGy

Table 4.2—E-Beam operation cost to upgrade one barrel of heavy oil.

Operation Time, hr/day	24
Daily Electricity Consumption, kWh	3552
Elecricity Cost in TX[a], cents/kWh	8.08
Daily Electricity Cost, $	287
Yearly Electricity Cost, $	103321
Operation Cost, cents/bbl	3

a. Electricity price for industrial use

Fig. 4.4 shows the cost of using the E-Beam operation to process a barrel of heavy oil with different absorbed doses. We can find that the operation cost is proportional to the absorbed dose. Thus, we can increase the radiation energy to enhance the radiation effect, though this will increase the operation cost. We need to find the optimum doses for the numerous upgrading processes utilized within the petroleum industry.

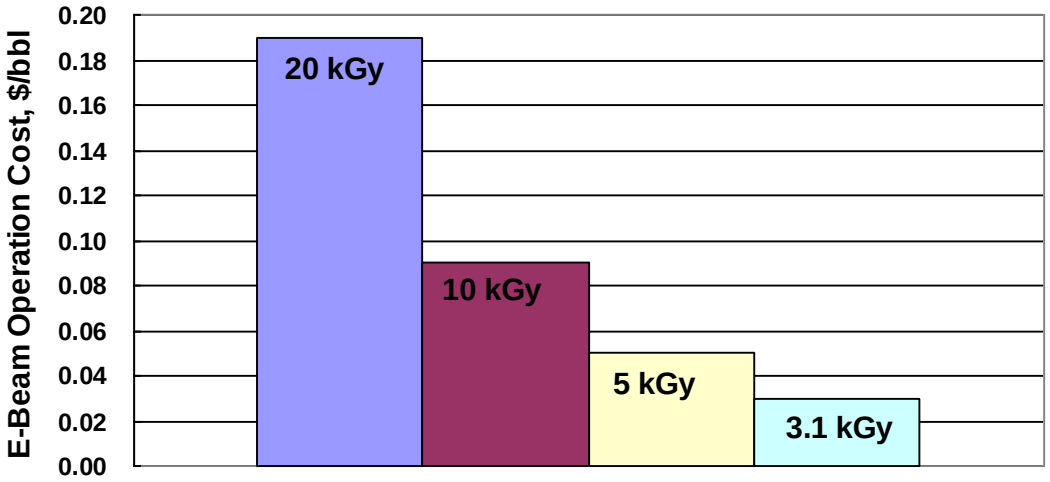

Fig. 4.4—Operation cost of E-Beam is proportional to dose.

4.3 Economic Comparison of E-Beam Upgrading and Conventional Upgrading

Visbreaking is a mild thermal cracking to reduce viscosity and sulfur content of heavy oil. The processing cost of this method is relatively lower than other upgrading methods. With our asphaltene experimental results, we compared the process cost of E-Beam upgrading with conventional visbreaking. **Table 4.3** shows average energy consumption for a coil type visbreaking. Using the natural gas price in Texas, we converted the amount of thermal required to upgrade 1 bbl of heavy oil to energy cost. The result is 73 cents per bbl.

Table 4.3—Average energy consumption for a conventional visbreaking and converted money value.

Avg. Energy Consumption[a], MMBtu/bbl	0.14
Natural Gas Price in TX[b], $/MMBtu	5.35
Thermal Energy Converted to Cost, cents/bbl	73

[a]Average energy consumption based on estimated utility
Source: DOE
[b]Gas price for industrial use
Source: EIA 2009

From the asphaltene experiments, we observed that RTC increased the amount of light oil by 39%. Since we had a lighter RTC sample compared to the TC sample, we estimated a 50% increase in volume with RTC. Therefore, with RTC we are able to get 50% more light oil compared to conventional visbreaking. **Fig. 4.5** and **Fig. 4.6** show the energy cost of a coil type visbreaking and E-Beam upgrading, respectively. The main assumption for this energy cost calculation is that each process used the same heat flux, so that the only difference between them is the E-Beam operation cost for the E-Beam upgrading. To generate the same amount of light oil created from RTC**,** the visbreaking (**Fig. 4.5**) needs to increase the volume of heavy oil by 50%. So, the energy cost for upgrading 1.5 bbl of heavy oil is 110 cents per unit light oil. **Fig. 4.6** shows the energy

cost of E-Beam upgrading. Since this process upgrades 1 bbl of heavy oil, the energy cost of this process is the sum of the thermal energy and E-Beam operation cost. Therefore, with E-Beam processing we can reduce the upgrading cost by 31%. In addition, we obtain better quality of light oil with E-Beam processing.

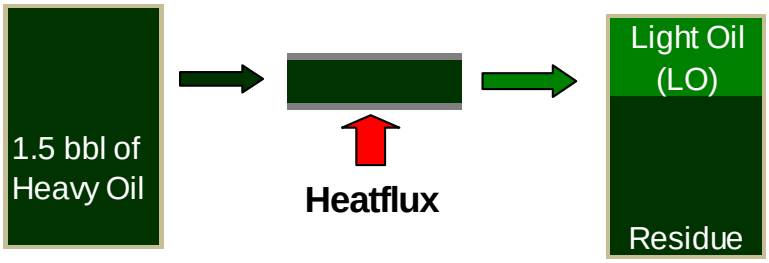

Energy Cost: 1.5 bbl x 73 cents/bbl=110 cents/Unit LO

Fig. 4.5—The energy cost to upgrade a certain amount of unit oil from conventional visbreaking can be calculated with the energy consumption data of visbreaking (Table 4.3).

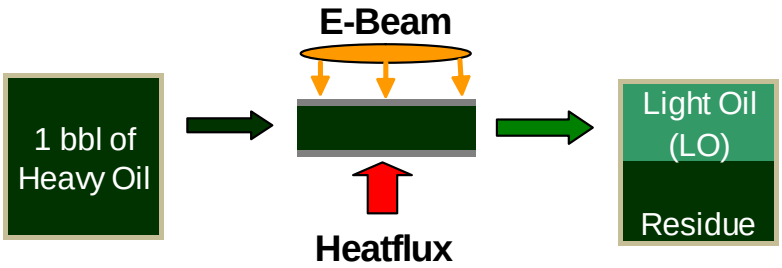

Energy Cost: 1bbl x (73 cents/bbl + 3 cents/bbl)=76 cents/Unit LO

Fig. 4.6—The energy cost to upgrade a certain amount of unit oil from E-Beam upgrading can be calculated with the energy consumption data of visbreaking (Table 4.3) and E-Beam operation cost (Table 4.2).

CHAPTER V

CONCLUSIONS

5.1 Conclusions

The parallel experiments conducted with n-C_{16}, naphtha, and asphaltene indicate that radiation effects on hydrocarbons are significant.

In the naphtha distillation, we found that E-Beam irradiation may have caused exothermic reactions and these reactions increased the heat of vaporization, resulting in a higher vapor temperature profile and distilled yield**.** In addition, we observed that radiation effect on naphtha distillation is proportional to the amounts of electrons absorbed in the fluid.

The results of the asphaltene experiment (the lighter RTC sample and higher isoparaffin formation) show that C-C bond decomposition and isomerization are enhanced with E-Beam irradiation. In addition, the lower aromatics content in the RTC sample indicates a significant reduction of aromatic components during E-Beam irradiation.

From the result of the reflux experiment conducted with n-C_{16}, we found that C-C bond cleavage and polymerization take place simultaneously during the chain reactions. The polymerization reaction can be reduced using a special procedure such as radical trapping using Tempo, and it will require modification of the experimental set up. Another reflux experiment with naphtha indicated that E-Beam broke hydrocarbon molecules in the naphtha and generated lighter components. In addition, this reaction generated more olefins from C-H dissociation.

The energy transfer simulation of E-Beam upgrading of the multiphase and single phase n-C_{16} is a valuable initiative which researchers have never tried before. With the heat transfer simulation, we estimated heat loss, fluid movement, and density distribution during the reaction.

Using the density distribution data from the heat transfer simulation, we conducted a radiation simulation to estimate accurately the radiation dose in the fluid. From the simulation, we found that insulating an aluminum can using glass fiber and a pyrex glass cover minimizes heat loss, though it prevents many electrons from entering the fluid.

Under multiphase conditions, we found that the system has much heat loss because of the condenser (cooling load) so it is unlikely that cracking of fluid occurs during the reflux.

From the Monte-Carlo simulation, we found that the penetration depth of E-Beam is limited. However, even though the penetration of electrons in the fluid is very low, we are able to distribute the radiation dose evenly through convection of the fluid.

The simulation study makes possible the optimization of conditions for laboratory experiments and industrial-scale design of the process.

The inexpensive operating cost of the E-Beam machine (3 cents per barrel) indicates that the application of E-beam technology is economically feasible. This new technology will enable upgrading of heavy oil without excessive thermal energy consumption or use of catalysts, resulting in higher profits from heavy oil production.

5.2 Challenges and Recommendations

In E-Beam upgrading, since the main source for the process is the high kinetic energy of E-Beam, it is important to deliver effectively many electrons to the hydrocarbons. However the main challenge for the delivery of electrons is the penetration depth. The penetration of E-Beam is disproportional to the density of the media. Therefore, if we shoot electrons through a highly dense media, such as a steel pipe, the penetration depth of electrons will be very low. Because electrons are charged particles, they interact with, and transfer their energy to, all the atoms in the media, and stop moving once they lose their energy. A possible solution in pipeline heavy oil upgrading is to make a special thin window in the E-Beam shooting area.

In order to improve the penetration of E-Beam, we can increase the kinetic energy of electrons so these electrons can travel longer distances. However, in accordance with IAEA guidelines for avoiding radioactivity we have a limited range of kinetic energy of E-Beam to 10 MeV. If we use the very high kinetic energy of electrons, the reaction may possibly generate neutrons.

Even though we use a machine that can generate 10 MeV of electrons, the efficiency is not good. This is because the efficiency of E-Beam machines decreases as the kinetic energy of the electrons generated by the machine increases. Using machines that generate electrons that have high kinetic energy therefore, would not be economical since it consumes so much energy.

Estimating accurately the dose distribution in the fluid with convection is very difficult. A possible solution we proposed and conducted is a coupled heat transfer and radiation transport simulation. To develop this approach, we need to find a way to compute fluid movement in the MCNP code without huge amounts of computation time.

Finding major process mechanisms are very important since we have to quantify certain energy ranges with this new process, such as the amount of radiation energy required for a certain type of upgrading. This work will help us compute chemical reactions in our simulation.

All our experimental setups are based on batch systems. However, we need to conduct experiments under continuous flowing systems for more practical industrial applications. To do so we need to conduct simulation studies to pre-design the process before building up experimental apparatus. These simulations can provide the best residence times, desirable geometry, and operating temperature constrained to fluid characteristics.

NOMENCLATURE

Gy = Gray (J/kg)

ε = Energy imparted by ionizing radiation (kJ)

R_{in} = The radiant energy incident on the volume (J)

R_{out} = The radiant energy emerging from the volume (J)

ΣQ = The sum of all changes of the rest mass energy of nuclei and elementary particles in any nuclear transformations which occur in the volume (J).

D = Absorbed dose (kJ/kg)

$\dot{D}$ = Absorbed dose rate (Gy/sec)

K = Kerma (J/kg)

K_c = Collision kerma (J/kg)

ψ = Energy fluence (J/m^2)

$\frac{\mu_{en}}{\rho}$ = Energy absorption coefficient

X = Exposure (C/kg)

$\overline{W}_{air}$ = Energy required to generate a pair of positron and electron (33.97 eV/i.p)

K_{H_2} = Hydrogen formation rate constant (lbmol/hr/lbmol)

$\dot{n}_{H_2}$ = Moles of hydrogen produced per hour

$n_{C_{16}}$ = Moles of n-C_{16}

$M_{C_{16}}$ = Molecular weight of n-C_{16}

n_{gas} = Moles of gas produced

V_{gas} = Volume of gas produced (m^3)

Vm_{gas} = Molar volume of gas produced (m^3/mol)

ΔQ = Heat energy (kJ)

m = Mass of sample (g)

c_p = Specific heat capacity under constant pressure (J g^{-1} K^{-1})

GC = Gas chromatography

RTD = Radiation thermal distillation

TD = Thermal distillation

RTC = Radiation thermal cracking

TC = Thermal cracking

MeV = Mega electron volt

Avg. MW = Average molecular weight

Avg. API = Average API gravity

Wt% = %WGT= Weight percent

$\Delta H_{(vap)}$ = Enthalpy of vaporization

Q_i = Heat used for a vaporization of each component

Q_{total} = Total heat of vaporization

U = Overall coefficient of heat transfer (W/mm^2K)

A = Area (m^2)

H = Heat transfer coefficient (W/mm^2K)

K = Thermal conductivity (W/mmK)

q = Heat flow rate (W)

q / A = Heat flux (W/m^2)

R = Gas constant (8.314472 $JK^{-1}mol^{-1}$)

T = Temperature (Kelvin)

ω = Acentric factor

T_C = Critical temperature (Kelvin)

P_C = Critical pressure (Pa)

v_c = Critical molar volume (m^3/mol)

F_α = Buoyancy force

g = Gravity

Nu = Nusselt number

Re = Reynolds number

Pr = Prandtl number

REFERENCES

Agrell, J. and Faucher, M. 2007. Heavy Oil Bitumen Dehydration: A Comparison Between Disc-Stack Centrifuges and Conventional Separation Technology, *SPE Production & Operation* **22** (2) : 156-160.

Alboudwarej, H., Felix, J., Taylor, S., Badry, R., Bremner, C., Brough, B., Skeates, C., Baker, A., Palmer, D., Pattison, K., Beshry, M., Brown, G., Calvo, R., Triana, J.A.C., Hathcock, R., Koerner, K., Houghes, T., Kundu, D., Cardenas, J.L., West, C. 2006. *Highlighting Heavy Oil*, Oil Field Review Report, Schlumberger.

ANSYS CFX Manual, ANSYS CFX, Release 11.0 2009 Texas A&M University, College Station.

Argillier, J.F and Henaut, I. 2005 Heavy Oil Dilution, Paper SPE 97763 presented at the International Thermal Operations and Heavy Oil Symposium, 1-3 November 2005, Calgary, Alberta, Canada.

Attix, F.H. 1986. Introduction to Radiological Physics and Radiation Dosimetry. New York: John Wiley & Sons.

Average Retail Price of Electricity to Ultimate Customers by End-Use Sector, by State, Year-to-Date through December 2008 and 2007, Energy Information Administration. http://www.eia.doe.gov/

Bennett, C.O. and Myers, J.E, Momentum, Heat, and Mass Transfer. New York: McGraw-Hill.

Berger, M.J., Coursey, J.S., Zucker, M.A., Chang, J. 2008 ESTAR Stopping-Power Range Tables for Electrons, Protons, and Helium Ions. Gaithersburg, MD: National Institute of Standard and Technology. Physics Laboratory, Ionizing Radiation Division.

Berger, M.J. and Seltzer, S.M. 1983. Stopping Powers and Ranges of Electrons and Positrons. NBSIR 82-2550-A, National Bureau of Standards, Washington, DC, 20234.

Bird, R.B., Stewart, W.E., and Lightfoot, E.N. 2006 *Transport Phenomena* 2nd edition, New York: John Wiley and Sons INC.

Braby, L. 2008 NUEN 613, Principles of Radiological Safety, class notes, Fall 2008, Texas A&M University, College Station.

Brown, F. B. 2003. MCNP-A General Monte Carlo N-Particle Transport Code, Version 5., Los Alamos, NM: Los Alamos National Laboratory

CATIA V5R18, DASSAULT SYSTEMS, Texas A&M University, College Station, TX.

Chang, W.K. 2008. Internal Combustion Engines. MIT Open Course (2.6.1) http://ocw.mit.edu/OcwWeb/web/home/home/index.htm

Chao, A., and Tigner, M. 1999. *Handbook of Accelerator Physics and Engineering*. River Edge, NJ.: World Scientific Publishing Co.

Dickenson, R.L. and Biasca, F.E. 1997. Refiner Options for Converting and Utilizing Heavy Fuel Oil. *Hydrocarbon Processing* **76** (2): 57-61.

Direct Scientific. 2009 Ionization chambers. http://www.drct.com/.

Elliot, K. 2008. Examination of Oil Sands Projects: Gasification, CO2 Emissions and Supply Costs. Paper SPE 117824 presented at the 2008 SPE/PS/CHOA International Thermal Operations and Heavy Oil Symposium, Calgary, Alberta, Canada, 20-23 October. SPE 117824-MS. DOI: 10.2118/117524-MS.

Energy and Environmental Profile of the U.S. Petroleum Refining Industry. U.S. DOE/OIT, December 1998. Natural Gas Industrial Price 2009, Energy Information Administration. http://www.eia.doe.gov/

Enthapy of hydrocarbons, NIST Chemistry webbook. http://webbook.nist.gov/chemistry/, (March 2009)

Foldiak, G. 1981. *Radiation Chemistry of Hydrocarbons.* Amsterdam: Elsevier.

Fortes Da Silva, P, 2008 Phd candidate at the Department of Biological and Agricultural Engineering, Texas A&M University College Station: New reactor design: Personal communication.

Humphries, S. 1986. *Principles of Charged Particle Acceleration*. New York: John Wiley.

Khan, M.R. 2007 Crude Value Enhancement: An Emerging Opportunity for Innovation in E&P. Paper SPE 112809. SPE Distinguished lecture during 2006-2007.

Kim, J. Post doctoral research associate at Department of Biological and Agricultural Engineering, Texas A&M University, College Station: Monte Carlo simulation of three different oils; Personal communication, (April 2009).

Kim, J. 2009. Post doctoral research associate, Radiation Transport Monte Carlo Simulation at n-C_{16}. Research report prepared for the 2009 E-Beam Workshop, College Station, TX. 25 June.

Kim, J. and Silva, P. Post doctoral research associate and PhD candidate at Department of Biological and Agricultural Engineering, Texas A&M University, College Station: Van De Graff Tune Up; Personal communication (December 2008).

Koppel, P.E, Mazurek, W.L, and Harji, A. 2002. Projects Scenarios for Bitumen Upgrading. Paper SPE 78983 presented at the 2002 SPE International Thermal Operations and Heavy Oil Symposium and International Horizontal Well Technology Conference, Calgary, Alberta, Canada, 4-7 November 2002.

Lee, K.B., *Heat Transfer Analysis*, Taesung S&A 2006, Seoul, South Korea.

Lott, R.K. and Lee, T.L.K, (HC)3 Hydrocracking Technology, Paper SPE 98058 presented at the 2005 SPE International Thermal Operations and Heavy Oil Symposium, Calgary, Alberta, Canada, 1-3 November 2005.

Luo, Peng and Gu, Yonggan 2007. Effects of Asphaltene on the Heavy Oil Viscosity at Different Temperatures. *Fuel* **86** (2007):1069-1078.

Miao, P., Zhao, C., Xu, G., Tang, W., Zeng, K., Wang, Y., Zhou, H., and Yang, G. 2009. Degradation of Poly (D,L-lactic acid)—poly (ethyleneglycol)-b-poly (D,L-lactic acid) copolymer by Electron Beam Radiation. *Journal of Applied Polymer Science* **12** (2009):2981-2987.

Michaelides, E.E. 2006. Particles, Bubbles and Drops. city, NJ: World Scientific.

NASA 2008. CFD Validation Assessment, Houston, TX: National Aeronautics and Space Administration.

Nelson , W.L. 1958, *Petroleum Refinery Engineering*. New York: McGraw-Hill.

Properties of fluid, Engineering Software and Database Service. 2008. http: www.engsolcom.com

PVTsim, Vers. 11.0, Calsep Inc. (2008), Texas A&M University, College Station.

Raseev, S. 2003. *Thermal and Catalytic Processes in Petroleum Refining*, 50. New York: Marcel Dekker, Inc.

Redlich, O. and Kwong, J.N.S. 1949 On the Thermodynamics of Solutions. V. An Equation of State. Fugacities of Gaseous Solutions, *Chemical Reviews.* (1949) **44**, 233.

Saniere, A. and Lantz, F. 2007. A World-Wide Economic Analysis of the Non Conventional Supply Based on a Modeling Approach. Paper SPE 107672 presented at the 2007 SPE Hydrocarbon Economics and Evaluation Symposium, Dallas, Texas, 1-3 April 2007.

Salovey, R. and Falconer, W.E. 1965. Radiation-Induced Reactions in n-Hexadecane. *Journal of Physics and Chemistry* **69**: 2345-2350.

Simanzhenkov, V. and Idem, R. 2003 *Crude Oil Chemistry*. New York: Marcel Dekker, Inc.

Taube, C. and Schmidt-Naake, G. 2001 TEMPO-Controlled Radical Suspension Polymerization in an Oil/Water System in an Autoclave. *Chemical Engineering & Technology* **25**(10): 1013-1017.

Turner, J.E. 1986. *Atoms, Radiation, and Radiation Protection.* New York: Pergamon Press.

Veith, E.J. 2007 Performance of a Heavy to Light Crude Oil Upgrading Process, Paper SPE 108678 presented at the 2007 International Oil Conference and Exhibition in Mexico, Veracruz, Mexico, 27-30 June 2007.

Wangen, E.S., McCaffrey, W.C., Kuznicki, S., Hoff, A.M and Blekkan, E.A. 2007. Cracking of Vacuum Residue from Athabasca Bitumen in a Thin Film. *Topics in Catalysis* **45**: 1-4

Wilson, E. J. 2001. *An Introduction to Particle Accelerators*. New York: Oxford University Press.

Woods, R.J and Pikaev, A.K. 1994, *Applied Radiation Chemistry: Radiation Processing. New York*: A Wiley-Interscience.

Wu, G., Katsumura, Y.Z., Matsuura, C., Ishigure, K., and Kubo, J. 1997. Radiation Effect on the Thermal Cracking of n-hexadecane. 1. Products from Radiation-Thermal Cracking. *Industrial & Engineering Chemistry Research* **36** (6):1973-1978.

Wu, G., Katsumura, Y.Z., Matsuura, C., Ishigure, K., and Kubo, J. 1997. Radiation Effect on the Thermal Cracking of n-hexadecane. 2. A Kinetic Approach to Chain Reaction. *Industrial & Engineering Chemistry Research* **36** (9):3498-3504.

Yan, T.Y. 2002. Upgrading of Heavy Oils: - An Overview. *Journal of Petroleum Technology* **38** (4): 39-50.

Yang, D. 2009. Electron Beam Irradiation Improve Conventional Heavy Oil Upgrading, presented at the 2009 SPE Gulf Coast Student Paper Contest, Houston, Texas, 18 April 2009.

Yang, D and Kim, J. MS candidate and post doctoral research associate at Department of Petroleum engineering and Biological and Agricultural Engineering: Dose Measurement and Calibration (2009) presented at the 2009 E-Beam Workshop, Texas A&M University College Station, 25 June.

Yang, D. 2009. Heat Transfer Simulation with CFD. Presented at the 2009 E-Beam Workshop, Texas A&M University, College Station, TX. 25 June.

Yang, D., Kim J., Silva, P., Barrufet, M., Moreira, R., and Sosa, J. Laboratory Investigation of E-Beam Heavy Oil Upgrading. Paper SPE 121911, presented at the 2009 SPE Latin American and Caribbean Petroleum Engineering Conference, Cartagena, Columbia, 31 May-3 June.

Yasar, M., Trauth, D.M., and Klein, M.T. 2001 Ashphaltene and Resid Pyrolysis. 2. The Effect of Reaction Environment on Pathways and Selectivities, *Energy and Fuels* **15**: 504-509.

Zaykin, Y.A., Zaykina, R.F., and Silverman, J. 2004. Radiation-Thermal Conversion of Paraffinic Oil. *Radiation Physics and Chemistry* **69** (3):229-238.

Zaykin, Y.A., and Zaykina, R.F. 2004. Bitumen Radiation Processing. *Radiation Physics and Chemistry* **71** (1-2):471-474.

Zaykin, Y.A., Zaykina, R.F., and Mirkin, G. 2003. On Energetics of Hydrocarbon Chemical Reactions by Ionizing Irradiation. *Radiation Physics and Chemistry* **67** (3-4):305-309.

Zaykin, Y.A. 2008. Low-Temperature Radiation-Induced Cracking of Liquid Hydrocarbons. *Radiation Physics and Chemistry* **77** (2008):1069-1073.

Zaykina, R.F., Zaykin, Y.A., Mamonova, T.B., and Nadirov, N.K. 2001. Radiation-Thermal Processing of High-Viscous Oil from Karazhanbas Field. *Radiation Physics and Chemistry* **60** (3):211-221.

Zaykina, R.F., Zaykin, Y.A., Mirkin, G., and Nadirov, N.K. 2002. Prospects for Irradiation Processing in the Petroleum Industry. *Radiation Physics and Chemistry* **63** (3-6):617-620.

Zaykina, R.F., Zaykin, Y.A., Yagudin, S.G., and Fahruddinov, I.M. 2004. Specific Approaches to Radiation Processing of High-Sulfuric Oil. *Radiation Physics and Chemistry* **71** (1-2):467-470.

Zhussupov, D. 2006. Assessing the Potential and Limitations of Heavy Oil Upgrading by Electron Beam Irradiation. MS Thesis, Texas A&M University, College Station, TX.

VITA

Name:	Daegil Yang
Permanent Address:	Harold Vance Dept. of Petroleum Engineering c/o Dr. Maria Barrufet Texas A&M University College Station, TX 77843-3116, USA.
Email:	daegil.yang@gmail.com

Education:	B.S., Automotive Engineering Kookmin University (Seoul), February 2005
	M.S., Petroleum Engineering Texas A&M University, December 2009